Università
degli Studi
della Campania
Luigi Vanvitelli

UNIVERSITÀ DEGLI STUDI DI SALERNO

Dipartimento di Fisica “E. R. Caianiello” e Dipartimento di Matematica

in convenzione con

UNIVERSITÀ DEGLI STUDI DELLA CAMPANIA "LUIGI VANVITELLI"

Dipartimento di Matematica e Fisica

Dottorato di Ricerca “Matematica, Fisica e Applicazioni” Curriculum Fisica
XXX Ciclo

Tesi Di Dottorato

Electrical and thermal transport properties of superconducting materials relevant for applications

Candidato
Francesco Avitabile

Tutor
Prof. Angela Nigro

Co-tutors
Dr. Gaia Grimaldi
Dr. Antonio Leo

Coordinator
Prof. Roberto Scarpa

A. A. 2017/2018

SUMMARY

Introduction

After a century from its discovery, superconductivity has promised to provide solutions to many challenges. Although their operation is limited only at cryogenic temperatures, superconducting materials are competitive in the development of large scale applications which need high power density and low losses [1-2]. For example, superconducting materials are used in the manufacture of high performing cables for the new generation power grids or high-field magnets [3]. In addition, Magnetic Resonance Imaging (MRI) needs a so stable magnetic field that it would not be technically possible without the use of superconducting magnets [4]. As well as particle accelerators that, except for 5% of their use dedicated to scientific research, have their main applications in industrial activity (implanting, sterilization, etc.) and nuclear medicine [5]. Moreover, highly stable superconducting magnets are used in magnetic levitation trains that can reach speeds of about 600 km/h and superconducting motors are being studied for use in aircrafts and ships [6]. Continuing this list, ongoing projects as Superconducting Magnetic Energy Storages (SMES) as well as protection systems for electrical networks like Superconducting Fault Current Limiters (SFCL) can be quoted [7]. Nowadays, if the confinement of nuclear fusion has become possible, it is only thanks to the use of superconducting magnets. Superconducting magnets-based reactors, as Tokamaks and Stellarators, are currently in use in the world for research purposes, and the most powerful nuclear fusion reactor in the world (ITER) is under construction in Cadarache, in the south of France [8]. Finally, a considerable scientific interest is also directed to the application of superconducting devices in the design of quantum computers [9] and in the sensor production, as single-photon detectors [10].

Fundamental properties and fabrication processes of a superconducting material have to fulfil some requirements in order to consider the material suitable for applications. In particular, the temperature below which the material is superconducting has to be as high as possible, the material has to remain in the superconducting state in magnetic field as intense as possible and it should show no-dissipation under as high as possible electrical biasing. Moreover, the material fabrication processes should be similar to already employed processes for conventional electrical conductors fabrication, or, at least, scalable and easy to implement.

Another important feature to consider is the voltage stability under current biasing in the dissipative regime which can be present in some superconducting materials for some applied magnetic field and bias current values. Indeed, once the biasing current density increases, the transition of the material to the normal state, referred also as a quench event, can be observed and often this transition is not gradual. In particular, if the Flux-Flow Instability (FFI) phenomenon is triggered, the transition in the current-voltage

(I-V) curve has the form of a sudden voltage jump [11-13]. Nevertheless, in some cases a more gradual transition is the most advisable one for a better control of quench.

In a superconducting device, thermal stability is another requirement to fulfil in order to avoid quench phenomena. Indeed, if the superconductor temperature rises locally above its critical value and the self-heating effects become significant, the normal zone will expand and eventually the whole magnet will revert to the normal state. In order to avoid such a quench, the dimension of the over-heated volume has to be smaller than the so called minimum propagation zone (*MPZ*). The length of the *MPZ* in a superconducting wire can be estimated by the thermal conductivity κ of the wire and its electrical resistivity ρ [14]. Superconductors have very small *MPZs* because they have very high ρ (in the normal state) and at the same time a very low κ. Moreover, the *MPZ* is not the only parameter that has to be kept under control. In a quench phenomenon, once a normal zone has started to grow, it will continue to expand, under the combined actions of heat conduction and ohmic heating, at a constant velocity referred as normal zone propagation velocity (*NZPV*). The *NZPV* describes how fast the overheated zone propagates during a quench, it plays a key role in the protection strategies against quench-induced damages, and it depends mainly on superconducting material heat capacity in the normal state.

Practical superconducting wires are made in composite form, containing both superconductor and a normal conductor. Indeed, heat transfer through the conductor is the main channel for removing heat and, consequently, preventing a quench. In particular, technical superconductors for large-scale applications are round or tape-shaped wires in which one or more superconducting filaments are embedded in a matrix consisting at least partially of a normal metal, such as Cu or Ag. They must carry operating currents, DC or AC, of hundreds of amperes. Among several superconducting elements and compounds, only a few of them are technologically suitable from the point of view of manufacturing wires for the current transport applications [3]. The currently commercial superconducting materials are NbTi, Nb_3Sn, $Bi_2Sr_2CaCu_2O_7$ (Bi-2212), $Bi_2Sr_2Ca_2Cu_3O_{10}$ (Bi-2223), MgB_2, and $YBa_2Cu_3O_7$.

Nowadays, the improvement in the fabrication techniques of iron-based superconductors have made them real competitors of HTS and MgB_2 in the perspective of high power wires and/or tapes production. Among the families of iron-based superconductors, the 11-family is one of the most attractive for high field applications at low temperatures. It has been recently demonstrated that it is possible to realize coated conductors able to carry very high current densities (up to 10^5 A cm^{-2} at 4.2 K and 30 T) [15] and it is possible to improve further the critical current density value with the proper choice of the substrate [16-18].

What we have done

We have carried out electrical and thermal transport characterization on superconducting materials relevant for applications and technical superconductors, as well. Measurements of this work were performed at MaSTeR-Lab of CNR-SPIN Salerno and Physics Department of Salerno University.

The electrical transport characterization of 11-compound Fe(Se,Te) thin films uses cryogen-free measurement systems. The Fe(Se,Te) thin films studied belong to the second generation of high-quality and purity thin films grown on CaF_2 substrates. All samples are provided by CNR-SPIN Genova. The obtained results have been compared with the first-generation one [18].

The analysis of the Fe(Se,Te) thin films $R(T)$ curves, carried out at fixed values of magnetic field, has allowed to estimate the pinning activation energy U. The pinning force as a function of the magnetic field has been also evaluated by J_c measurements, that is evaluating the maximum current value above which dissipation sets in. Then, by using the Dew-Hughes approach we have analyzed the pinning centers landscape.

However, the use on a large scale of iron-based cannot be achieved without the understanding of the current stability mechanisms in these compounds. For this reason, we have studied the I-V curves in a regime well above the critical current J_c and quench features similar to those related to FFI have been recognized.

A preliminary study has been done to determine how the instability parameters are influenced by the cooling environment. Indeed, cooling efficiency and thermal stability are strictly demanding for practical applications of superconductors operating at current values close to the critical current I_c, because a thermally unstable device can show premature quench. To obtain thermal stability, a balance between heat removal from the material and Joule heating must be reached. To this aim, we have studied heat exchanges of superconducting samples with the surrounding environmental setup by current driven stability measurements. In particular, we analyse I-V characteristics up to current values triggering the instability of the flux flow regime on NbN and NbTiN ultra-thin films realized in collaboration with CNR-SPIN Salerno and CEA Grenoble (J. C. Villégier Group).

The ultra-thin films have been cooled in different environments, namely liquid Helium bath and cryogen-free system with both dynamic He-gas and static He-gas. The effects of the cooling method on the electric current carrying stability of NbN and NbTiN ultra-thin films are reported.

It has been also investigated the relation between the critical current and the instability current in Fe(Se,Te) microbridges, with the analysis focus on the difference $I^{*}-I_c$, which can be seen as a safe range before the full quench of the superconductor. Indeed, in the range between I_c and the instability current I^{*}, the material is still in the superconducting phase, but dissipation due to moving vortices is present. The relation between these two critical current values is a high relevant topic to the potential high field applications of superconducting materials, but less well studied in the community, with few works on HTSs to our knowledge [19-20].

Experimental studies involving technical superconductors $Bi_2Sr_2CaCu_2O_{8+x}$ (Bi-2212) round wires are performed in collaboration with the Group of Applied Superconductivity (C. Senatore Group) at "Département de Physique de la Matière Quantique" of Geneva University (Switzerland). The thesis work is focused on electrical and thermal characterization of superconducting wires manufactured by Oxford Superconducting Technology (OST).

We have studied the thermal stability of technical superconductors by means of thermal and electric transport measurements. An increase of mass density, electrical connectivity and critical current density has been obtained in the samples by overpressure process under different total pressures reached adding Ar at a fixed O_2 partial pressure of 1 bar, with a maximum T of 890° C [21-25]. In particular, the thermal conductivity κ of samples reacted at different pressures, namely 1, 10 and 100 bar, in magnetic fields up to 19 T, have been examined.

An open issue about Bi-2212 conductors is understanding to what extent the Ag matrix is contaminated during the heat treatment due to Bi-2212 element diffusion. Among the elements composing Bi-2212, Cu has the highest solubility in Ag [26]. This contamination could have a negative effect on the *RRR* value and, consequently, on the thermal conductivity of the whole wire. Contrary to the case of LTS, the *RRR* of the matrix in HTS technical conductors cannot be evaluated from a resistivity measurement performed on the whole conductor. Indeed, due to the superconducting transition at high T, it is not possible to measure the residual ρ of the matrix. Previously, the residual resistance ratio (*RRR)* of the matrix had been evaluated in Bi-2212 wires processed with a non-standard partial-melt-processing in order to depress the critical current of the samples with very little superconducting phase [26]. In this work, an alternative method is presented which overcomes previous critical results [26]. Here the *RRR* of the metal matrix has been estimated by measuring the electrical resistance of short pieces of conductor in which the superconducting filaments have been removed by chemical etching. In this way, the samples are not exposed to heat treatments that could change the degree of contamination of the matrix. This has allowed us to quantify the effects of the overpressure heat treatment on the low-temperature electrical and thermal conductivity properties.

Moreover, a preliminary study on *NZPV* is presented. Among the various models known to estimate the *NZPV* the approximated expression used for the REBCO CC was taken into consideration. We have evaluated the error committed in this procedure for the *NZPV* estimate, measuring the heat capacity *C(T)* of the Bi-2212 round wires, and we have been able to determine how the error is reduced as the magnetic field increases.

Structure of this PhD Thesis work

The present work is constituted by four Chapters.

In the first part of Chapter 1, we present an overview on general aspects of superconductivity and the fundamentals on type II superconductors, pinning mechanisms and vortex dynamics in superconducting materials also introducing the parameters relevant for thermal stability of superconducting devices. Then, we present the superconducting materials that are relevant from the point of view of the applications. Finally, technical superconductors and their thermal transport properties are discussed.

In Chapter 2, the reader can find an overview on cooling methods as well as information about the measurements setups and the samples preparation.

In Chapter 3, the results of the electrical transport properties on Iron-based thin films are shown. Moreover, a study on the efficiency of cooling methods by FFI measurements on Nb-based thin films is also shown.

In Chapter 4, the determination of the thermal conductivity κ, heat capacity *C(T)* and of *RRR* by means of thermal and electrical transport measurements is reported.

1 SUPERCONDUCTIVITY AND APPLICATIONS

1.1 General Aspects

Superconductivity is a state of matter characterized by perfect conductivity and perfect diamagnetism [27]. It was discovered by H. Kamerlingh Onnes in 1911 when, while he was investigating the low temperature electrical resistance of a mercury sample, he found that below 4.15 K the DC resistance of that element decreased suddenly to zero [28]. In the following years, superconductivity was found in many metals, metallic compounds and alloys each of one showed superconductivity below different temperature values. The temperature below which their resistance drops to zero is called critical temperature and usually denoted as T_c. In 1933, Meissner and Ochsenfeld discovered the second effect, perfect diamagnetism, when they found that superconductors completely expelled internal magnetic fields below a certain critical field value, H_c [29].

Two years later, the London brothers developed a model based on two phenomenological equations explaining the Meissner effect and providing the penetration depth of the external magnetic field into the superconductors [30]. Subsequently, in 1950, Ginzburg and Landau formulated the so called macroscopic theory of superconductivity describing the superconducting state through an order parameter and providing a derivation for the London equation. In 1957, thanks to Ginzburg-Landau (GL) theory, A. Abrikosov explained some experimental observations concluding that for some superconductors there are two critical fields, H_{c1} and H_{c2}, among which there exists a mixed state where magnetic field penetrates the superconductor in quantized flux lines [31]. Superconductors showing only the Meissner state are referred as Type-I, while those also showing the mixed state are of Type-II. In the same year, Bardeen, Cooper and Schrieffer (BCS) introduced a microscopic theory of superconductivity [32]. BCS theory shows that superconductivity is due to the condensation induced by phonon interactions of electrons pairs (Cooper pairs) into a coherent ground state and that superconducting and normal state are divided by an energy gap. Both Ginzburg-Landau and London equations well fit into BCS formalism and many of its predictions were confirmed by experiments.

Following a BCS Theory interpretation, it has been argued that lattice instabilities would have destroyed Cooper pairing preventing any material to show a critical temperature higher than 30-40 K [33]. In spite of this prediction, in 1986 Alex Müller and Georg Bednorz discovered superconductivity in a sample of LaBaCuO with a critical temperature about 30 K [34]. This discovery was surprising because this material is a ceramic oxide that is typically an insulator. Due to that discovery the research on superconducting materials was mainly focused on copper oxide (cuprate) compounds bringing in a few years to a T_c of about 90 K (above the boiling point of liquid N_2 at 77 K) found in the cuprate $YBa_2Cu_3O_{7-\delta}$. [35-36]. In the following years, many different cuprate systems showed such high transition temperature reaching the critical temperature of 138 K at atmospheric pressure and 164 K under 30 GPa in the $HgBa_2Ca_2Cu_3O_8$ compound [37]. Many properties of these high-temperature superconductors (HTSC) are highly unusual. More than 25 years after their discovery, it is still unclear how the Cooper pairing is accomplished in these materials and it seems likely that magnetic interactions play an important role. The BCS theory is unsuitable to describe superconductivity in these complicated materials and the mechanism of high-temperature superconductivity is still an open question.

In 2001, the superconductivity was discovered in the compound MgB_2, synthesized for the first time in 1953 [38]. For years it has been considered a conventional superconductor, with the highest critical temperature (T_c = 39 K) found until then, but the presence of a gap multiband structure makes it not completely explained by the BCS theory [39-40].

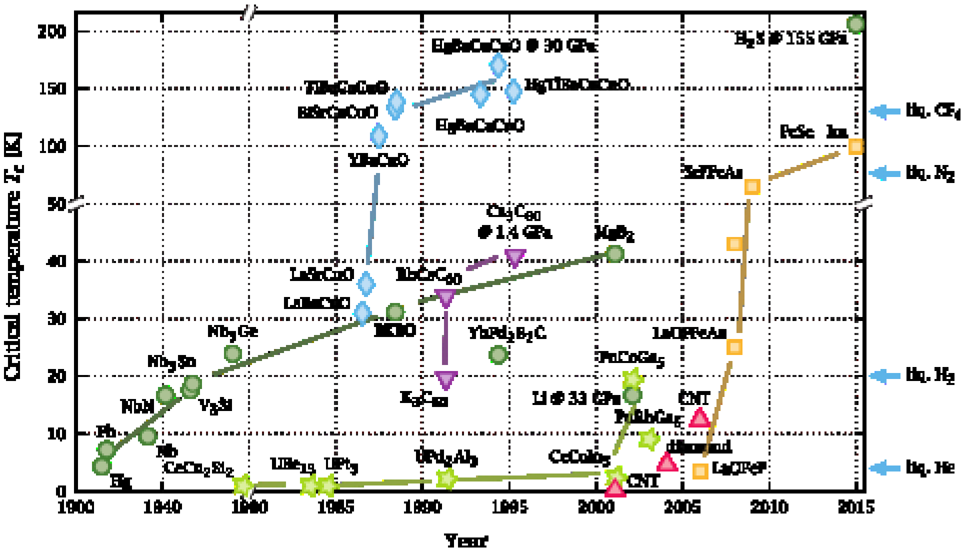

Fig. 1.1 : Superconducting timeline, BCS superconductors are displayed as green circles, cuprates as blue diamonds, and iron-based superconductors as yellow squares [48].

In 2008, H. Hosono et al. discovered another superconducting family, the iron based. They first found that the $LaO_{1-x}F_xFeAs$ compound was superconductor at 26 K [41]. Moreover, its critical temperature can reach higher T_c replacing Lanthanum atoms with other rare earth elements such as cerium, neodymium and praseodymium and up to 56 K with samarium doping [42-44]. In the iron base family are included iron-chalcogenides with the best critical temperature around 50 K [45]. Recently it was found that in particular conditions of growth on suitable substrates it was possible to obtain a T_c up to 100 K for FeSe-based ultra-thin films [46-47].

Several guidelines for achieving high T_c with no upper limit have been theorized in the past years (see also Fig. 1.1, [48]). For example, referring to the BCS Theory, Ashcroft argued that conditions as high-frequency phonons, strong electron–phonon coupling, and a high density of states, which can be in principle satisfied by metallic hydrogen and hydrogen dominant metallic alloys, can lead to T_c up to 300 K [49-51]. Indeed, in 2015, Drozdov et al. found that sulphur hydride transforms to a metal at a pressure of approximately 90 GPa and shows superconductivity transition at a T_c of 203 K at a pressure of 150 GPa just by following these guidelines [52]. Through this discovery, this material class is thought to be the best candidate to achieve room-temperature superconductivity.

1.1.1 Fundamentals

The phenomenological Ginzburg-Landau theory focuses its predictions entirely on the superconducting electrons providing that the local density of superconducting electrons n_{sc} is represented by the introduction of a complex pseudo-wavefunction, referred as the order parameter $\psi(\mathbf{r})$, for which holds the relation $|\psi(\vec{r})|^2 = n_s$ [27, 53].

The order parameter $\psi(\mathbf{r})$ is the solution of the differential equation obtained using a variational principle starting from a series expansion of the free energy in power of ψ and $\nabla\psi$ with expansion coefficients α and β which takes the form:

$$\frac{1}{2m^*}\left(-i\hbar\vec{\nabla} - \frac{e^*}{c}\vec{A}\right)^2 \psi + \frac{\beta}{2}|\psi|^2\psi = -\alpha\psi \tag{1.1}$$

where m^* and e^* are the Cooper pair mass and electric charge respectively, β must be positive for validity of theory, while α can be positive or negative. If $\alpha > 0$, the minimum free energy corresponds to:

$$|\,\psi|^2 = 0$$

If $\alpha < 0$, the minimum free energy corresponds to:

$$|\,\psi|^2 = |\,\psi_\infty|^2 = -\frac{\alpha}{\beta} \tag{1.2}$$

here ψ_∞ is the maximum concentration of Cooper pairs that can exist infinitely deep in the interior of the superconductor completely shielded from any field or current [27]. The characteristic distance over which $\psi(\mathbf{r})$ can vary without relevant energy increase is the so-called coherence length

$$\xi(T) = \frac{\hbar}{[2m^*\alpha(T)]^{1/2}} \propto \frac{1}{\sqrt{1 - T/T_c}} \tag{1.3}$$

Another characteristic length is the magnetic penetration depth $\lambda(T)$, which characterizes the distance over which the magnetic field is screened by the superconducting currents. It is found by II London equation [27]:

$$\vec{h} = -c\vec{\nabla} \times \Lambda\vec{J}_s \tag{1.4}$$

where h denotes the value of magnetic field density on a microscopic scale and $\Lambda = 4\pi\lambda^2/c^2 = m/n_s e^2$. If the eq. (1.4) is combined with Maxwell equation $\vec{\nabla} \times \vec{h} = 4\pi\vec{J}/c$ we obtain:

$$\nabla^2 \vec{h} = \frac{\vec{h}}{\lambda^2} \quad (1.5)$$

$$\nabla^2 \vec{J}_s = \frac{\vec{J}_s}{\lambda^2} \quad (1.6)$$

Where

$$\lambda = \sqrt{\Lambda/\mu_0} = \sqrt{\frac{mc^2}{4\pi n_s e^2}} \quad (1.7)$$

is called the London penetration depth. The solutions of these differential equations, in turn, yield magnetic fields and currents that, from their value on the superconductor surface, exponentially decrease with the London penetration depth λ inside the material. The penetration depth λ is temperature dependent due to the n_{sc} temperature dependence. The temperature dependant λ(T) was found to be approximately [27]:

$$\lambda(T) \approx \frac{\lambda(0)}{[1-(T/T_c)^4]^{\frac{1}{2}}} \quad (1.8)$$

It is useful to introduce the dimensionless Ginzburg–Landau parameter κ, which is defined as the ratio of the two characteristic lengths

$$\kappa \equiv \frac{\lambda(T)}{\xi(T)} \quad (1.9)$$

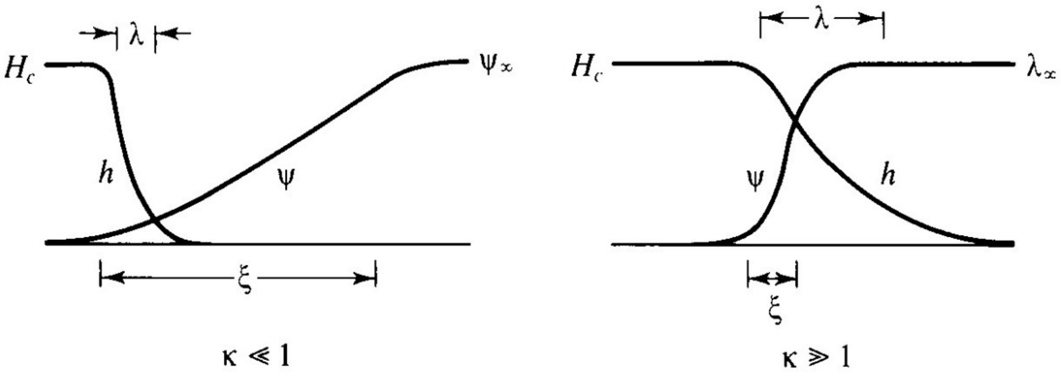

Fig. 1.2: Schematic diagram of variation of h and ψ in a domain wall. The case κ«1 refers to a type I superconductor; the case κ»1 refers to a type-II superconductor [27].

In pure superconductors, $\kappa \ll 1$, but in dirty superconductors or in HTS, $\kappa \gg 1$.

Superconductors can be classified on the basis of their Ginzburg-Landau parameter value. Type I superconductors are those with $\kappa < 1/\sqrt{2}$ with a positive sign of the surface energy of a boundary between normal and superconducting regions, while type II superconductors have $\kappa > 1/\sqrt{2}$ and a negative surface energy, which favours the formation of superconducting-normal boundaries and magnetic flux penetration [31].

The $H - T$ phase diagram for a bulk type I and type II superconductor is represented in panels (a) and (b) in Fig. 1.3, respectively. Type I superconductors ($\kappa < 1/\sqrt{2}$) are in the Meissner state for applied fields up to H_c, given by

$$H_c(T) = \frac{\Phi_0}{2\sqrt{2}\pi\mu_0\lambda(T)\xi(T)} \tag{1.10}$$

where Φ_0 is the superconducting flux quantum (see below). In the Meissner state, all magnetic flux is expelled from the interior of the sample ($B = 0$). At $H_c(T)$ a first-order transition occurs leading to a discontinuous breakdown of superconductivity, and the sample turns to the normal state [Fig. 1.3(a)]. Type II superconductors ($\kappa > 1/\sqrt{2}$) are in the Meissner state for fields smaller than the first (or lower) critical field

$$H_{c1}(T) = \frac{\Phi_0}{4\pi\mu_0\lambda^2(T)} ln(\kappa) \tag{1.11}$$

For fields $H > H_{c1}(T)$, there is a penetration of magnetic flux until, at the so-called second (or upper) critical field, the system becomes normal [Fig. 1.3 (b)]. This second critical field can be expressed as

$$H_{c2}(T) = \frac{\Phi_0}{2\pi\mu_0\xi^2(T)} \tag{1.12}$$

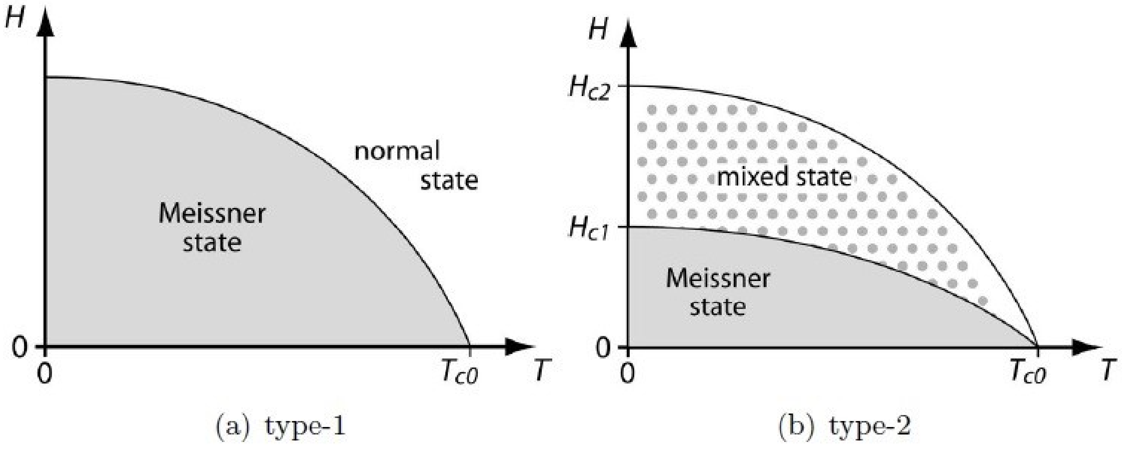

(a) type-1 (b) type-2

Fig. 1.3: The H-T phase diagram of a (a) type I and (b) type II superconductor [54]

The phase between H_{c1} and H_{c2} is referred as mixed state or Abrikosov vortex state, where the flux penetrates in a regular array of flux tubes or *vortices*, each bearing a superconducting flux quantum $\Phi_0 = h/2e = 2.07 \times 10^{-15}$ T m^2 [31]. Thanks to the partial flux penetration, the diamagnetic energy for maintaining the field out is less, so H_{c2} can be much greater than H_c.

1.1.2 Vortex lattice

The magnetic field penetrates in a type II superconductor as an array of vortices distributed through the material. If the separation between the vortex is large compared to λ, the vortex-vortex interactions can be neglected, then they can be considered as isolated. The vortex structure consists of a normal core of radius ξ, around which shielding currents circulate. The local magnetic field h and the superconducting electron density n_{sc} are functions of the distance r from the vortex center as schematically represented in Fig. 1.4 [54].

The local magnetic field and current distribution in the mixed state ($H_{c1} < H < H_{c2}$) of a type II superconductor can be calculated from the London model [30], with the requires of $\kappa \gg 1$ and the order parameter is nearly constant in space. In this limit, we can obtain from London equation (1.4) the local field distribution around a vortex as [27]

$$\mu_0 h(r) = \frac{\Phi_0}{2\pi\lambda^2} K_0\left(\frac{r}{\lambda}\right) \tag{1.13}$$

where K_0 is the zero-order Bessel function which, at short distances ($\xi < r \ll \lambda$), tends to:

$$K_0 = ln\left(\frac{\lambda}{r}\right) \tag{1.14}$$

and, at large distances ($r \gg \lambda$), tends to:

$$K_0 = \sqrt{\frac{\pi\lambda}{2r}} exp\left(-\frac{r}{\lambda}\right). \tag{1.15}$$

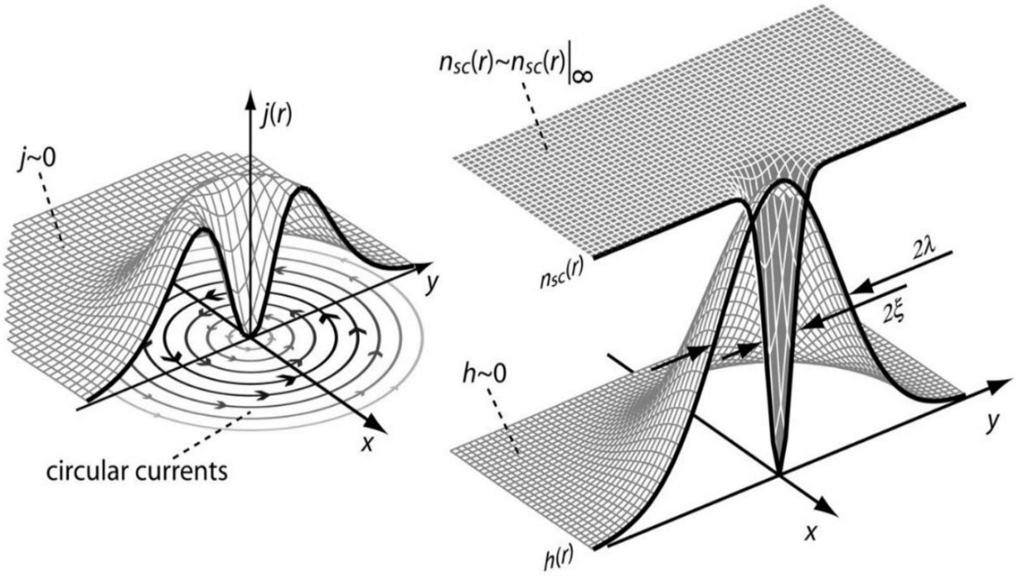

Fig. 1.4: Structure of a single vortex, showing the radial distribution of the local field h(r), the circulating supercurrents j(r) and the density of superconducting electron $n_{sc}(r)$ [54]

It can be observed that the local field h is highest in the center of the vortex core where superconducting order parameter (ψ *or* n_{sc}) is zero and his value is given by the limiting form:

$$\mu_0 h(r) \approx \frac{\Phi_0}{2\pi\lambda^2}\left[ln\frac{\lambda}{r} + 0.12\right], \qquad \xi \ll r \ll \lambda \tag{1.16}$$

and decays over a distance given by the penetration depth λ:

$$h(r) \rightarrow \frac{\Phi_0}{2\pi\lambda^2}\left(\frac{\pi}{2}\frac{\lambda}{r}\right)^{1/2} e^{-r/\lambda}, \qquad r \rightarrow \infty \tag{1.17}$$

due to the screening currents. Then, the current distribution of a single vortex can be calculated by performing the derivative of the local field with respect to the radial distance dependence, [55]:

$$J(r) = \frac{\Phi_0}{2\pi\mu_0\lambda^2} K_1\left(\frac{r}{\lambda}\right) \tag{1.18}$$

Here, K_1 is the first order Bessel function which decreases as $1/r$ for $\xi < r \ll \lambda$, and diverges as K_0 at large distances $r \gg \lambda$. Finally, the energy of a flux line is the sum of the field and the kinetic energy of the currents and a small core contribution [56]:

$$E_l = \frac{1}{4\pi\mu_0}\left(\frac{\Phi_0}{\lambda}\right)^2 \left[ln\left(\frac{\lambda}{\xi}\right) + 0.12\right] \tag{1.19}$$

where the constant 0.12 describes the contribution of the normal core. Since E_l is a quadratic function of the magnetic flux, it is energetically unfavourable in a homogenous superconductor to form multiquanta vortices, carrying more than one flux quantum.

The interaction energy between more parallel vortices is easy to treat under the approximation $\kappa \gg 1$. Due to the repulsive electromagnetic interaction, they tend to be positioned as far away from each other as possible, resulting in the well-known Abrikosov vortex lattice [31]. The repulsive force between two vortices f_{ij} is [56]:

$$f_{ij}(r_{ij}) = \frac{\Phi_0^2}{2\pi\mu_0\lambda^3} K_1\left(\frac{r_{ij}}{\lambda}\right) \tag{1.20}$$

If two vortices are generated in a type I superconductor, the value of ξ is larger than λ, so the normal cores overlap first, leading to a gain in the condensation energy and thus to vortex-vortex attraction [57] [58] [Fig. 1.5(a)]. Instead in a superconductor of the type II, the magnitude of the λ value would cause the currents to overlap first, leading to vortex-vortex repulsion [Fig. 1.5(b)]. For a given vortex density, the most favourable configuration in which the vortices are arranged is triangular lattice [Fig. 1.6], with the density of vortices n_v increases with increasing field. The distance a_v between nearest neighbour vortices in the triangular lattice is related to the induction B through the relation

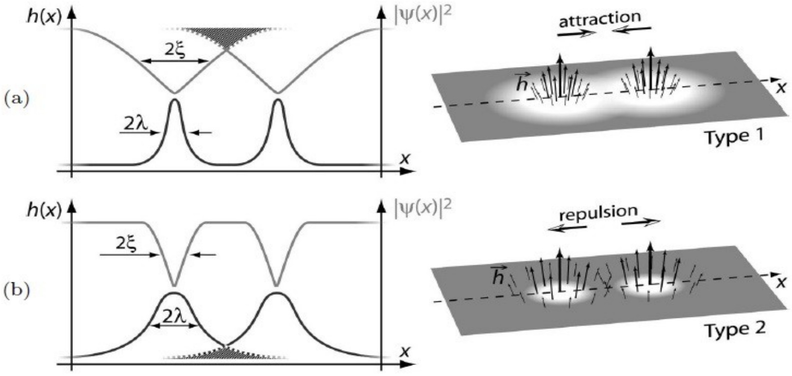

Fig. 1.6: Schematics of the vortex-vortex interactions: (a) in type I superconductors, vortex core are overlapping first, thus causing an attraction between vortices; (b) in type II materials, the first to overlap are the local fields h(x), which leads to a vortex-vortex repulsion [54].

$$B = \Phi_0 n_v = \frac{2}{\sqrt{3}} \frac{\Phi_0}{a_v^2} \tag{1.21}$$

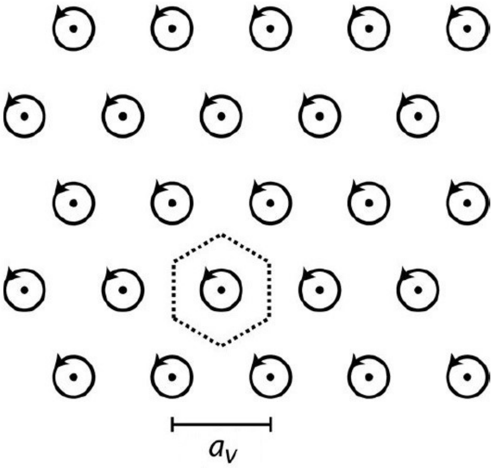

Fig. 1.5:Schematic diagram of a triangular vortex lattice with period a_v, The dashed lines indicate the unit cells [54].

1.1.3 Vortex Pinning

In the case that a Type II superconductor immersed in a magnetic field above H_{c1} is crossed by an electric current, the flux lines start moving due to the Lorentz force that results from the action of the current density $\vec{J}$ on the flux lines. Such a Lorentz force per unit length and per one vortex is given by:

$$\vec{f}_L = \vec{J} \times \vec{\Phi}_0 \tag{1.22}$$

and tends to move the vortices transversely to the current. Such motion induces an electric field parallel to $\vec{J}$ of magnitude:

$$\vec{E} = \vec{B} \times \vec{v} \tag{1.23}$$

where $\vec{v}$ is the flux lines velocity. This acts like a resistive voltage with power dissipation and, in this scenario, makes a type II superconductor to be unable to sustain a persistent current.

In order to be suitable for applications, type II superconductors must be able to carry high current in very high fields without resistance. In other words, there should be a threshold current value below which no power dissipation is observed. High values for such a critical current density can be reached if the flux lines are prevented from moving. Thus, a pinning force $\vec{f}_P$ associated with the introduction of a pinning center into the superconductor should neutralize $\vec{f}_{\mathrm{L}}$. In real type-II superconductors, vortices are pinned by any spatial inhomogeneity of the material causing a local minimum in the free energy landscape. Crystalline imperfections, columnar defects, grain boundaries, twin boundaries, or stochiometric deviations, amongst others, can act as pinning centers. The pinning can also be induced artificially by irradiation, ion implantation, film thickness modulation, doping, etc.

However, if currents are strong enough, and the pinning is weak compared to the driving force a regime sets in, in which the vortex moves. In the flux flow regime, the vortex velocity can be though as limited by a viscous drag. In this scenario, the total force acting on the flux line per unit length is the sum of several contributions [59]:

$$\vec{f} = \vec{f}_L - \vec{f}_P - \eta\vec{v}_v - \vec{f}_M \tag{1.24}$$

where $-\eta\vec{v}_v$ is a small friction-like contribution (the viscous damping force) proportional through η to the vortex velocity $\vec{v}_v$, and $\vec{f}_M = \alpha(\vec{v}_v \times \hat{n})$ is the Magnus force, where $\hat{n}$ is a unit vector in magnetic field direction and α a constant. As long as every individual vortex is prevented from moving, for the eq. (1.25) it holds the condition $\vec{f} = \vec{f}_L - \vec{f}_P = 0$. As the bias current increases, the Lorentz force will reach a value equal to the pinning force, beyond which the vortices will undergo a depinning. The current value for which this condition is reached is the critical current I$_c$, also referred as depinning current. The average macroscopic pinning force per unit volume is related to the depinning current density by the expression

$$f_P = J_c B \tag{1.25}$$

In a steady state, the vortex velocity $\vec{v}_v$, will achieve a constant value. In the limit of a pinning-free superconductor (f_P = 0), $\vec{v}_v$ is determined entirely by the viscosity of the medium, yielding $\vec{v}_v = (\boldsymbol{J} \times \Phi_0)/\eta$. From this expression, and from eq. (1.24) it is possible to define the *flux flow resistivity* [27]

$$\rho_f = \frac{E}{J} = \Phi_0 \frac{B}{\eta} \tag{1.26}$$

which arises exclusively from the viscous flow of vortices.

The critical current density may be determined experimentally as function of B. From eq. (1.25), the resulting $f_P(B)$ function shows a maximum in the $f_P(B)$ function, being zero at $B = 0$ and at $B = \mu_0 H_{c2}$ due to $J_c(\mu_0 H_{c2}) = 0$ for definition. Introducing the normalized magnetic field ($h = H/H_{c2}$), it is found that at different temperature

$$f_P(h) \propto H_{c2}^n(T) f_n(h) \tag{1.27}$$

where *n* and $f_n(h)$ are characteristic of the pinning mechanism operating in the superconductor.

Among the theories which have tried to account for the observations about pinning properties in materials, Dew-Hughes approach has a good general view [60]. In this approach, the pinning force per unit volume is expressed as:

$$f_P = -\gamma \frac{L\Delta W}{x} \tag{1.28}$$

where ΔW is the work done to move a unit length of flux-line from a pinning center to the nearest position where is unpinned, *x* is the effective range of pinning interaction, *L* is the total length of flux-line per unit volume which is directly pinned and γ is an efficiency factor determined by the extent to which the flux-line neighbours in the lattice allow to relax toward a position of maximum pinning. These quantities are influenced by the nature and the size of the pinning centers, the rigidity of the flux line lattice and the size of the pinning micro-structure compared to λ, intimately connected to fundamental nature of the pinning interaction. Fundamental pinning interactions are the ones between the normal core and a pinning site (core interactions), or the interactions between the pinning sites and the distribution of magnetic fields and supercurrents in the sample (magnetic interactions). The analytical expressions for the $f_n(h)$ in the various cases can be summarized as in Table 1.1 and sketched as in Fig. 1.7.

Regarding the behaviour of the vortex lattice in the presence of pinning forces, assuming a certain elasticity of the lattice, two cases can occur. In the first case, the pinning force exerted by the pinning sites is weak and so the lattice preserves its long range correlation, in the second one, the pinning force is so strong that the breaking of the lattice structure is possible. These possibilities as referred as weak pinning and strong pinning respectively [27, 61]. The action of many weak pins on the vortex system is described by the collective pinning theory while the interaction between vortices and strong pinning center is described by Labusch model. The crossover between weak and strong pinning is based on defining the Labusch criterion [62]:

$$f_{Lab} = \frac{\epsilon_0 \xi}{a_0} \tag{1.29}$$

where $\epsilon_0 = \Phi_0/4\pi\lambda^2$ is the line energy scale. In weak pinning regime $f_P < f_{Lab}$, while the strong pinning regime is characterized by $f_P > f_{Lab}$.

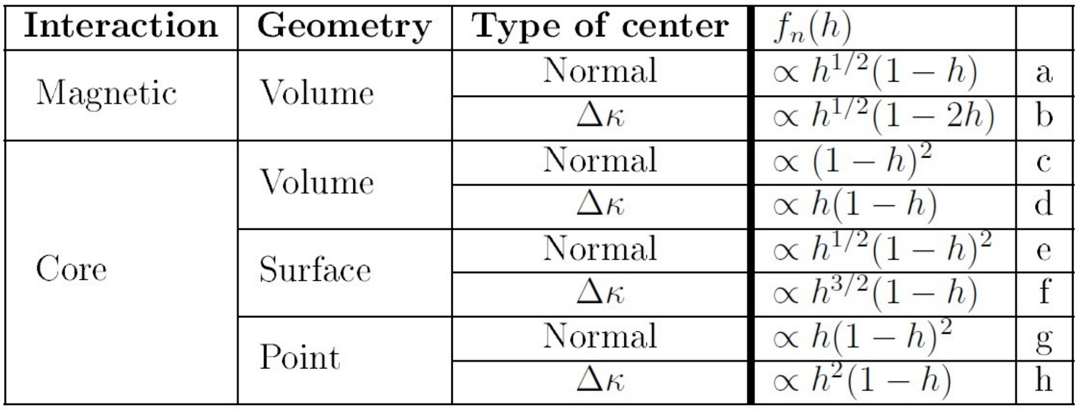

Interaction	Geometry	Type of center	$f_n(h)$	
Magnetic	Volume	Normal	$\propto h^{1/2}(1-h)$	a
		$\Delta\kappa$	$\propto h^{1/2}(1-2h)$	b
Core	Volume	Normal	$\propto (1-h)^2$	c
		$\Delta\kappa$	$\propto h(1-h)$	d
	Surface	Normal	$\propto h^{1/2}(1-h)^2$	e
		$\Delta\kappa$	$\propto h^{3/2}(1-h)$	f
	Point	Normal	$\propto h(1-h)^2$	g
		$\Delta\kappa$	$\propto h^2(1-h)$	h

Table 1.1

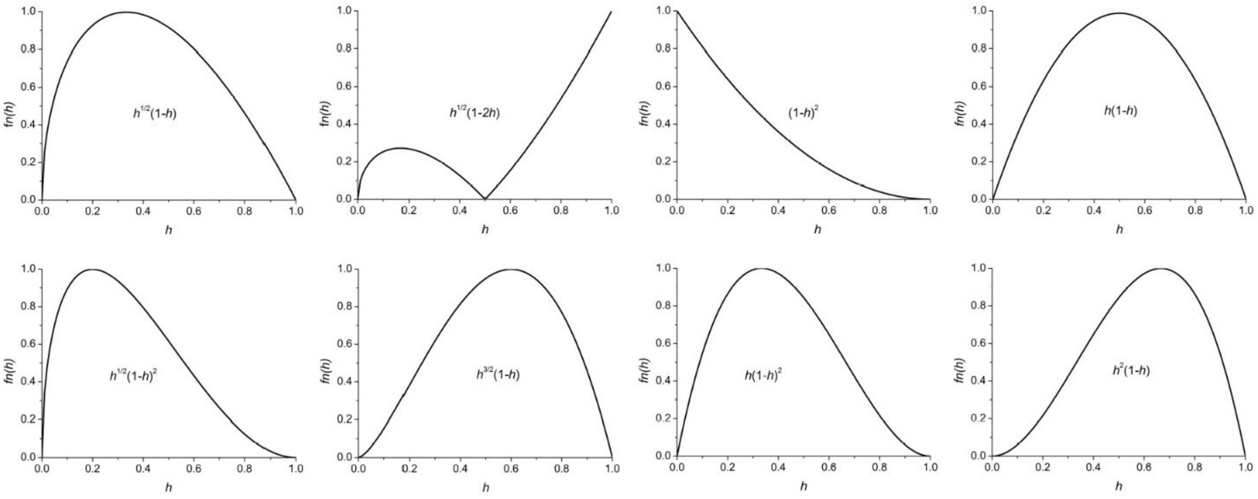

Fig. 1.7: $f_n(h)$ curves for the various expression given in the table 1.1 [60].

The vortex pinning and the condition $J < J_c$ do not warrant the complete absence of vortex motion. Indeed, thermal excitations can provide enough energy for vortices to hop from one pinning site to another at finite temperatures. This type of vortex motion generates a resistive voltage proportional to the average creep velocity. This regime is referred as *flux creep,* and its velocity is usually much smaller than the resistive flux flow velocity. In the Anderson-Kim Flux-Creep theory, which assumes flux line bundles jumping as a unit due the interaction between vortex, the electric field generated by the flux-creep-assisted vortex motion is given by [27]

$$E = v \cdot B = \omega_0 L \cdot e^{-\frac{U_0}{k_B T}} \cdot sinh\left(\frac{\alpha L^4}{k_B T}\right) \qquad (1.30)$$

Here v is the creep velocity, ω_0 is a characteristic frequency of flux-line vibration ranging within 10^5 to 10^{11} s^{-1}, L is the jump width, α is the driving force density so that αL^4 is the difference in potential energy between two neighbouring pinning sites, and $U_0 = U_0(T, B, J)$ is the activation energy or barrier energy, *i.e.* the height of the potential barrier between two adjacent pinning sites. For $J \ll J_c \frac{k_B T}{U_0}$, the system is in the so-called *thermally assisted flux flow* (*TAFF*) regime where for the electric field it is possible to write:

$$E_{TAFF} \propto J \cdot exp\left[-\frac{U_0}{k_B T}\right] \qquad (1.31)$$

1.1.4 Flux Flow Instability

The equation (1.26), obtained neglecting flux pinning, showed the Ohm's law behaviour $E \propto J$ of free flux flow regime. However, the constancy of the dumping η and the Magnus force α coefficients require that the vortex structure does not change. This scenario is reasonable at low vortex velocity, while at high vortex velocity strong deviation from linear Ohm's law can be observed.

This kind of non-linear flux flow behaviour can be explained through the Larkin-Ovchinnichov (LO) theory which assumes spatial homogeneity of the nonequilibrium quasiparticle distribution [63]. In the high temperature limit ($T \approx T_c$), where the order parameter is most sensitive to small changes in quasiparticle distribution function, the vortex core is approximated by a normal phase cylinder with radius ξ filled with quasiparticles [11]. The electric field generated by vortex motion provides to the quasiparticle energy sufficient to get out of the core. As a consequence, a fraction of the quasiparticles leaves the vortex core, thus the core shrinks and the damping coefficient of the friction force ηv_φ decreases with increasing vortex velocity v_φ.

The relation derived by LO for the damping coefficient is

$$\eta(v_\varphi) = \frac{\eta(0)}{1 + \left(v_\varphi / v_\varphi^*\right)^2} = \frac{\eta(0)}{1 + (E/E^*)^2} \tag{1.32}$$

Here $\eta(0)$ is the damping coefficient in the limit $v_\varphi \to 0$ while v_φ^* is the velocity value above which we have a negative differential resistivity. This critical velocity v_φ^* can be expressed as:

$$v_\varphi^{*\,2} = \frac{D[14\zeta(x = 3)]^{1/2}(1 - T/T_c)^{1/2}}{\pi \tau_\varepsilon} \tag{1.33}$$

where $D = v_F l/3$ (with v_F the Fermi velocity and l the electron mean free path) is the diffusion coefficient of the quasiparticles, $\zeta(x) = \sum_{n=1}^{\infty} \frac{1}{n^x}$ is the Riemann zeta function and τ_ε is the quasiparticle energy relaxation time. The relation between the critical voltage $V*$ and the velocity v_φ^* is [12]:

$$V^* = \left|\vec{v}_\varphi^* \times \vec{B}\right| L = \mu_0 v_\varphi^* H L \tag{1.34}$$

where L is the length of the current path between the voltage contacts and H is the applied magnetic field. In agreement with LO model the current-voltage characteristics is described by the relation [12]:

$$I - I_c = \frac{V}{R_{ff}} \left[\frac{1}{1 + (V/V^*)^2} + c \left(1 - \frac{T}{T_c}\right)^{1/2} \right] \tag{1.35}$$

Where I_c is the critical current and R_{ff} is the flux-flow resistance and c is a constant of order unity. At $V = V^*$, the corresponding current value I^* is the instability current at which the negative differential resistance appears. This branch, subsequently, merges the normal state branch $V = R_N I$ (in which R_N is the normal state resistance). In the current-driven measurements the S-shaped curve is hidden by an abrupt jump from flux flow regime to the normal state branch at $I = I^*$. This sudden voltage jump, also referred as quench, is the signature of the Flux Flow Instability (FFI) phenomenon. I-V curves of a Nb film, for different values of the magnetic field at $T = 4.2$ K, displaying the voltage jumps, are shown in Fig. 1.8. Although from (1.30) the critical velocity v_φ^* is expected independent of the magnetic field B, it has been experimentally found that at low magnetic fields $v_\varphi^* \sim B^{-1/2}$ [64].

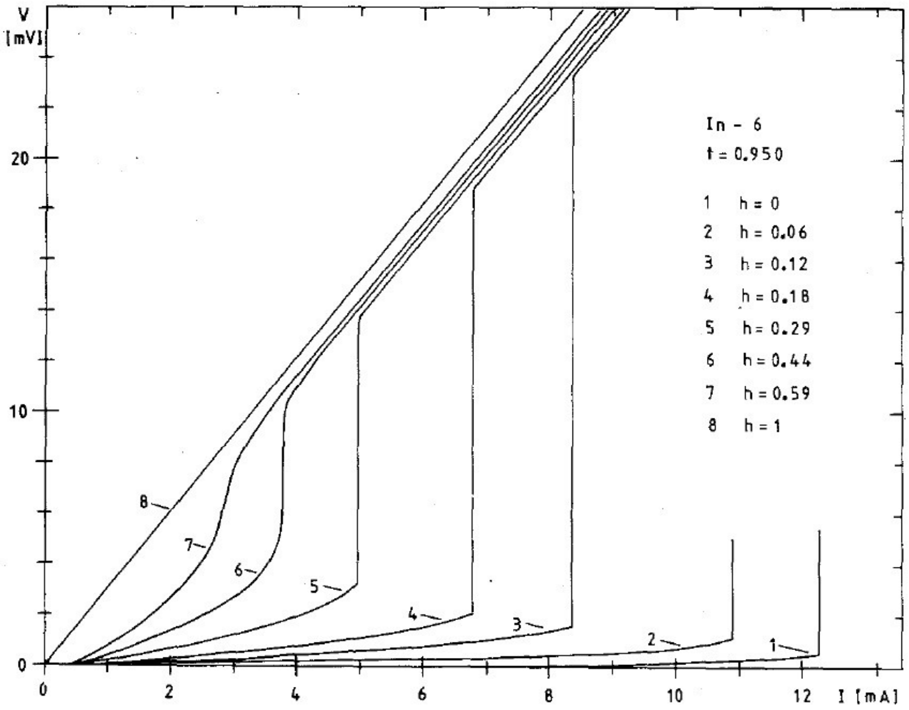

Fig. 1.8: Voltage-current characteristics for a superconducting thin film of In, grown on a sapphire substrate, at different applied magnetic fields. [11]

In the low-temperature limit ($T \ll T_c$), the electronic instability can be related to the electron overheating [65-66]. Due to dissipations in the flux-flow regime, electrons reach temperatures above the phonon temperature, which leads to an expansion of the vortex core and a consequent reduction of the viscous drag. The signature of the instability in the I -V curves is very similar between the LO as in the electron overheating regime, despite the different mechanisms present in the two distinct temperature ranges. Also, the magnetic field dependence of the critical vortex velocity is $v^* \propto B^{-\frac{1}{2}}$ [65], although it has been noted that, regardless of the temperature limit, a more complex dependence can be present at very low fields, due to the pinning properties of the material and sample geometry [67-72].

The quenching of the superconducting state can also occur due to the Joule self-heating caused by thermal dissipations of the vortex motion. The occurrence of this thermal instability in HTSCs at zero applied magnetic field has been theoretically described as a pure consequence of a temperature runaway, which takes place up to the quenching temperature *T**, where a very steep voltage jump sets in [73-74]. It is claimed that, under certain experimental conditions heating effects become predominant [73], and at sufficiently high current densities cuprate HTSCs become thermally unstable [74]. In Fig. 1.9 is illustrated an experimental procedure where the I-V curves obtained are not constant temperature curves [73].

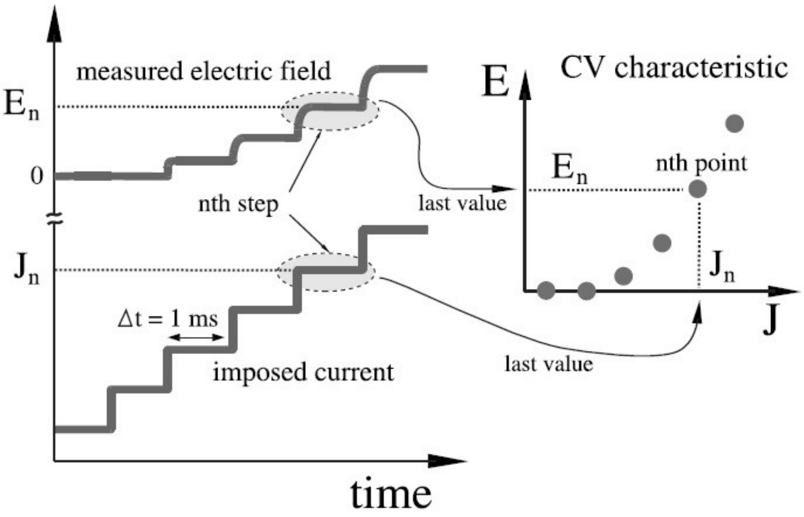

Fig. 1.9: Experimental building procedure I-V curves with a staircase ramp of current applied to YBCO microbridges [73].

On the other hand, also the LO model has been extended by Bezuglyj and Shklovskij [11] (BS) in order to include the effect of self-heating near T_c in a finite magnetic field. In this case, a crossover scenario emerges with a threshold value of the applied magnetic field B_T between the LO and pure self-heating regimes. For $B \ll B_T$ the instability is triggered by an intrinsic change of the distribution function of quasiparticles trapped in the vortex core, whereas for $B \gg B_T$ it is driven by pure thermal effects [75]. This crossover corresponds to a distinctive magnetic-field dependence of the Joule power $P^* = I^* V^*$ at the instability, which is field dependent for $B \ll B_T$ and saturates for $B \gg B_T$. This parameter is expressed in terms of the quasi-particle energy relaxation time τ_ε and the heat transfer coefficient h as:

$$B_T = \frac{0.374 \cdot e \cdot h \cdot \tau_\varepsilon}{k_B} \left(R_N \frac{W}{L} \right) \qquad (1.36)$$

with k_B the Boltzmann constant, *e* the electron charge and R_N the normal state resistance at T_{onset}, W is the width and L the length of the superconductor.

In general, the relative importance of thermal effects can be characterized by the value of the Stekly parameter α [76], defined as the ratio of the heat generation in the normal state $\rho_N J_c^2$ and the heat transfer $2(T_c - T)h/d$, being ρ_N, J_c, h, and d, respectively, the normal state resistivity, critical current density, heat transfer coefficient, and film thickness [76]. Self-heating is important if $\alpha > 1$, and negligible if $\alpha \ll 1$. This parameter gives a measure of thermal contributions to the flux flow instability, and depends on the intrinsic properties of the sample, but also on experimental conditions and on the substrate.

1.1.5 T_c, H_c, J_c: Critical Surface

In practical applications, superconducting materials biased by an electric current often must work in high magnetic fields. Therefore, let us analyse the behaviour of a cylindrical superconducting wire immersed in a magnetic field parallel to its axis. The superconducting perfect diamagnetism involves that within the superconductor the magnetic field is zero ($B_{in} = 0$), while on the surface it is equal to the external value ($B_{ext} = \mu_0 H_{ext}$). Moreover, Ginzburg–Landau and London theories provide the presence of a layer at the lateral surface of superconductor where the magnetic field drops exponentially to zero from its external value on a distance equal to the penetration depth. In this layer, a shielding current circulates to generate an inner field opposite to the external field which cancels the field inside the superconductor. We must also consider that when an electric current bias is applied to the wire, it generates a radial magnetic field with a linear radius dependence inside it and inversely proportional dependence outside it. Moreover, the current density cannot be uniform inside it, otherwise internal magnetic flux would be different from zero, but it must flow only in the λ spaced surface layer, perpendicular to the shielding current. Both for the shielding current and for the transport current we have that the current density is given by [55]:

$$J(r) = \frac{B_{surf}}{\mu_0 \lambda} exp\left[-\frac{(R-r)}{\lambda}\right] = \frac{I}{2\pi R\lambda} exp\left[-\frac{(R-r)}{\lambda}\right] \qquad (1.37)$$

Where B_{surf} is the magnetic field at surface of wire, R is the wire radius, r is the radial distance from the wire centre. The total current is obtained by integrating $J(r)$ over the cross section of the superconducting wire and is $I = 2\pi R\lambda J$ where $2\pi R\lambda$ is the effective cross-sectional area of the surface layer and J is $J(r)$ calculated at $r = R$.

In the case of superconductors, the fact that there is a critical field H_c also limits the amount of maximum current that can flow within it. For both the shielding and the transport case we have

$$B_c(T) = \mu_0 \lambda(T) J_c(T) \qquad (1.38)$$

Here the current value J_c is the value of the current at which the critical field H_c is reached. In Type I superconductors, where current can flow only in a surface layer of thickness λ, the average current density carried by a superconducting wire with $R >> \lambda$ is very low. It would be possible to obtain high average current densities if the radius R is less than penetration depth. The fabrication of such filamentary wire is not practical since Type I superconductors show a λ about 50 nm.

The explicit temperature dependences of $B_c(T)$ and $\lambda(T)$ and $J_c(T) = B_c(T)/\mu_0\lambda(T)$ are given by Ginzburg-Landau theory [55]:

$$
\begin{aligned}
B_c &= B_c(0)\left[1-\left(\frac{T}{T_c}\right)^2\right]\\
\lambda &= \lambda(0)\left[1-\left(\frac{T}{T_c}\right)^4\right]^{-1/2}\\
J_c &= J_c(0)\left[1-\left(\frac{T}{T_c}\right)^2\right]\left[1-\left(\frac{T}{T_c}\right)^4\right]^{-1/2}
\end{aligned}
\qquad (1.39)
$$

Where $\lambda(0) = \lambda_L$. The asymptotic behaviours at $T \rightarrow 0\ K$ [77] and near the transition temperature $T \approx T_c$ [78] were found respectively as:

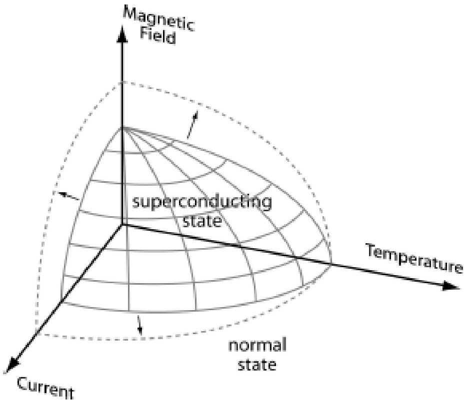

Fig. 1.10: Sketch of the critical surface that separates the superconducting from the normal state in the space span by temperature, magnetic field and current [54]

$$
\begin{aligned}
B_c &= B_c(0)\left[1-\left(\frac{T}{T_c}\right)^2\right] & & & B_c &\approx 2B_c(0)\left[1-\left(\frac{T}{T_c}\right)\right]\\
\lambda &\approx \lambda(0)\left[1-\frac{1}{2}\left(\frac{T}{T_c}\right)^4\right] & &and & \lambda &\approx \frac{1}{2}\lambda(0)\left[1-\left(\frac{T}{T_c}\right)\right]^{-1/2}\\
J_c &\approx J_c(0)\left[1-\left(\frac{T}{T_c}\right)^2\right] & & & J_c &\approx 4J_c(0)\left[1-\left(\frac{T}{T_c}\right)\right]^{3/2}
\end{aligned}
\qquad (1.40)
$$

Therefore, it can be introduced a three-dimensional space where the axes are the applied magnetic field B, the transport current I, and the temperature T in which the critical behaviour of a superconductor is represented through a critical surface (Fig. 1.10 from ref. [54]) separating the superconducting zone from the normal zone. We have that at a certain temperature T there is a magnetic field $B_c(T)$ at which there is the superconducting/normal switch. Similarly, you can carry a current density up to a certain value $J_c(T)$ above which the superconductor passes to the normal state. Technological applications development needs the expansion of this surface as far as possible and it represents one of the main topics in the scientific research on these materials.

1.1.6 Thermal Stability of technical superconductors

One of the most demanding aspects of all devices, is the reliability. In practical applications involving the use of superconducting wires such as magnets windings, the performances of these wires are always lower than those of tests carried out on short conductor samples. This effect, referred as coil degradation, consists in a magnet quench, i. e. any part of magnet goes from superconducting to the normal resistive state, at currents much lower than the critical current measured on a short sample, typically in the region Q of Fig. 1.11.

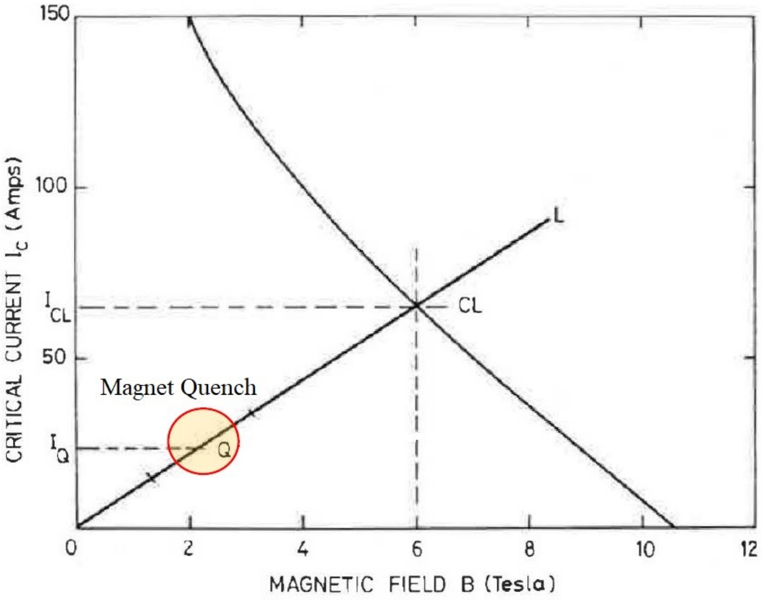

Fig. 1.11: Short sample critical current I_c for a NbTi wire of 0.3 mm diameter and load line for a small solenoid [14].

The problem is usually caused by a sudden rise of temperature in a wire region, due to different kinds of local disturbances (wire motion, flux jumping, AC losses, particle showers, etc [14, 79]), which causes the reduction of the superconductor critical current I_c. At the temperature value, referred as current sharing temperature T_{CS}, a sharing of the operating current I_{Op} between the superconductor and the metallic stabilizer starts, and an ohmic heating probably generates causing the quench. This process causes that the entire stored energy $\frac{1}{2}LI^2 \propto B^2$ of the magnet is dissipated as heat.

However, not only it is needed a certain density of energy to give life to a quench, but it is also important the energy impulse size. For triggering a quench, the dimension of the normal zone created volume (as showed in Fig. 1.12), must be greater than a certain volume referred as minimum propagation zone (MPZ). In determining the size of the MPZ it needs to consider the heat diffusion equation governing the temperature of a superconductor unit volume

$$C(T)\frac{\partial T}{\partial t} = \nabla \cdot [\kappa(T)\nabla T] + \rho(T)J^2 + g_d + g_{cooling} \tag{1.41}$$

where the left-hand side represents the time rate of change of thermal energy density of the conductor, with $C(T)$ as the heat capacity per unit volume of the composite conductor which consists of superconductor and normal-metal matrix [79]. In the right-hand side, the first term describes thermal conduction density into the composite superconductor element, where $\kappa(T)$ is the thermal conductivity of the composite. The second term is Joule heating, with ρ as the normal state electrical resistivity, and J as the current density at operating current $I_{Op}(t)$, which can depend on time. Thermal disturbance is described by g_d, primarily magnetic and mechanical in origin, and the last term represents cooling. Assuming that the conductor is characterized by a uniform and temperature-independent thermal conductivity κ, under time-independent and adiabatic conditions, with no dissipation other than Joule dissipation, i.e. $C(T)\frac{\partial T}{\partial t} = 0$ $g_d = 0$, $g_{cooling} = 0$, in eq. (1.41), an expression for the length of the MPZ is derived:

$$l_{MPZ} \approx \sqrt{\frac{2\kappa\left(T_{cs} - T_{Op}\right)}{J_c^2\rho}} \tag{1.42}$$

where T_{Op} is the operative temperature [14]. A normal zone which is longer than this will grow because generation exceeds cooling; conversely a shorter zone will collapse, and full superconductivity will be recovered.

The smallest energy able to trigger a quench, referred as minimum quench energy MQE, is a key parameter in the evaluation of superconducting devices stability. In case of superconducting wires or tapes it is calculated from l_{MPZ}:

$$MQE \approx l_{MPZ} S_{Tot} \int_{T_{Op}}^{T_{CS}} c(T)\, dT \tag{1.43}$$

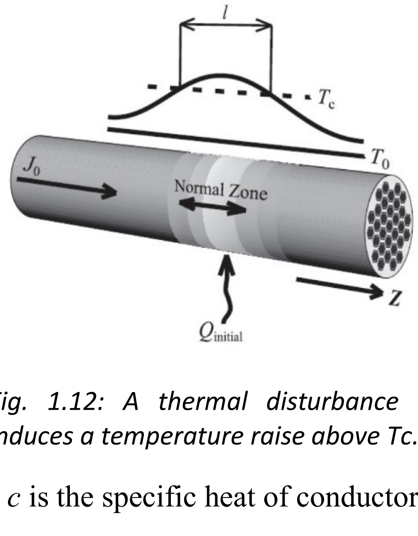

Fig. 1.12: A thermal disturbance Q_{in} induces a temperature raise above Tc.

Where S_{Tot} is the cross section and c is the specific heat of conductor [14, 79].

Superconductors have very small *MPZs* because they have very high resistivity ρ (in the normal state) and at the same time a very low thermal conductivity κ. Practical superconducting wires are therefore made in composite form, containing both superconductor and a normal conductor (usually copper or silver) [14]. Indeed, at low temperature, the resistivity of all pure metals decreases rapidly with temperature as the scattering of conduction electrons by lattice vibrations is reduced. At very low temperatures however, the resistivity reaches a constant value referred as residual resistivity ρ_{res}, very much lower electrical resistivity than the resistivity ρ(273 K), determined by the impurity level and by other lattice defects. Moreover, their thermal conductivity is higher than superconductors. For example, the ratio κ/ρ for the copper matrix is 7.5 x 10^6 higher than for the superconducting filaments of a NbTi wire [14].

1.1.7 Normal zone propagation velocity

By designing any superconducting device, one wants to keep the *MQE* as large as possible for enhancing its stability. Nevertheless, this is not the only parameter that has to be kept under control. In a quench phenomenon, once a normal zone has started to grow, it will continue to expand at constant velocity referred under the combined actions of heat conduction and ohmic heating. This irreversible process is referred as normal zone propagation velocity (*NZPV*) and causes the entire stored energy $\frac{1}{2}LI^2$of the magnet to be dissipated as heat. Therefore, the quench detection is a critical issue for superconducting magnets. The *NZPV* describes how fast the overheated zone propagates during a quench playing a key role in the protection strategies against quench-induced damages. In fact, the resistance of the normal zone and the corresponding resistive voltage are the vectors of the primary quench detection. Quench detection using voltage measurements is likely to be the fastest technical solution available [80].

The propagation of the perturbation along the conductor depends on the properties of the materials present in the winding. The *NZPV* can be evaluated following different approaches. The most practical way to evaluate the *NZPV* is to use the formulas that result from the solution of the heat equation describing the quench process [14, 79, 81]. The differential equation (1.41), describing the adiabatic quench process in a superconductor, with $g_d = 0$, $g_{cooling} = 0$, becomes:

$$C(T)\frac{\partial T}{\partial t} = \nabla \cdot [\kappa(T)\nabla T] + g_j(T) \tag{1.44}$$

Now, on the right-hand side, after the thermal conduction there is only the Joule heating [79]. In case of composite superconductor, the Joule heating is $g_j(T) = \rho_m(T)J_m(T)J$, where ρ_m is the matrix electrical resistivity, and J_m and J are the current density in the matrix and composite, respectively [82]. An analytical expression for the *NZPV* in adiabatic conditions was derived assuming it as the velocity of a translating coordinate system representing the normal-superconducting boundary moving during a quench

[83]. In order to take into account the effects due to the current sharing between superconductor and metal matrix, the *NZPV* expression was further modified and the deduced formula is [82]:

$$NZPV \approx J\left[\frac{1}{\rho_n(T_t)\kappa_n(T_t)}\left(C_n(T_t) - \frac{1}{\kappa_n(T_t)}\frac{d\kappa_n}{dT}\bigg|_{T=T_t} \times \int_{T_{Op}}^{T_t} C_S(T)dT\right)\int_{T_{Op}}^{T_t} C_S(T)dT\right]^{-1/2} \quad (1.45)$$

where the subscripts *n* and *s* indicate the normal and superconducting state, respectively, T_t is the transition temperature, T_{Op} is the operative temperature. The transition temperature T_t has been introduced in place of the T_c in technical superconductors, in order to define an effective superconducting/normal boundary during a quench, where the current sharing effects are important. In the case of LTS, T_t is generally considered as the average value between the current sharing temperature and the critical temperature $T_t = (T_{CS} + T_c)/2$. In HTS, T_t is more properly evaluated as the temperature at which the heat generation term in eq. (1.44) assumes its average value in the current sharing temperature range:

$$g_j(T_t) = \left[\int_{T_{CS}}^{T_c} g_j(T)dT\right]/(T_c - T_{CS}) \quad (1.46)$$

Neglecting the temperature dependence of the material properties, eq. (1.45) may be simplified to

$$NZPV \approx \frac{J}{C}\left[\frac{\rho\kappa}{(T_t - T_{Op})}\right]^{-1/2} \quad (1.47)$$

Different approaches have been proposed to evaluate the *NZPV* by eq. (1.47) in LTS [14, 79]. However, due to the complications encountered in solving the more general eq. (1.45) these approaches are extended in the practice also to HTS.

1.2 Superconducting materials relevant for applications

After its discovery in Hg, the superconductivity was found in other metallic elements of the periodic table. Elemental superconductors are typically Low Temperature Superconductors (LTS) and their behaviour is well described in the BCS theory. Only three metals exhibit Type II superconductivity, namely Niobium, Vanadium and Technetium, but among them Nb is the only one relevant for applications. Indeed, Niobium is the one with the highest critical temperature (T_c = 9.2 K) [80]. Unfortunately, metallic superconductors show very low critical magnetic fields, so their technological application was not promising because they did not support significant currents. When De Haas and co-workers began to investigate the behavior of superconducting alloys in magnetic field, they discovered that superconductivity could endure in significantly strong magnetic fields [84]. Today we know that it is possible thanks to the penetration of the magnetic field flux lines which are fixed through pinning forces in type II superconductors. Moreover, the introduction of defects enhances the magnetic field that the superconductor could tolerate before moving to the dissipative regime and the so-called hard superconductors are obtained.

Among the many metal alloys known today, Nb-based alloys have the best superconducting properties and are used in the manufacture of sensors, detectors, digital electronics and radio frequency devices [10, 85-87]. If the ratios between atomic species are well defined and there is a crystallographic order, we have intermetallic compounds. In general, superconducting intermetallic compounds achieve higher critical temperatures, the most important family of them being the A-15 type (with A_3B formula). Within this family we found Nb_3Ge (23 K), Nb_3Ga (20 K), Nb_3Sn (18 K) etc [88]. NbTi is another important Nb-based compound; it shows a critical temperature $T_c \approx 9.3\ K$ and an upper critical field $B_{c2} {\sim} 15\ T$.

The design of LTS materials for applications depends on several factors. For example, wires manufacture requires that they be used in the form of multifilament wires in a normal conductive matrix to increase the J_c, and to protect the device in case of quench (see wires section). NbTi multifilamentary wires with a Cu composed matrix (NbTi/Cu) represent the largest application of LTS and superconductors in general. Other LTS compounds are used in the manufacture of superconducting devices, which are recommended in some applications because of their quantum nature and low-noise cryogenic operation environment. For example, hot-electron detectors are the best least noisy receivers in the radiation wave ranges of hundreds of GHz and of THz [89]. In particular, superconducting NbN-based hot-electron devices are very suitable for fast and ultrasensitive optical detection due to their recovery time, inductance and system-detecting efficiency [10] . Indeed, due to the superconducting energy gap 2Δ, that is the energy needed to create a quasiparticle and which is much lower than the semiconductors gap, a single crossing photon in a superconducting detector can give rise to an avalanche electron charge resulting in devices with energy resolution much higher than in a semiconductor detector [90].

The discovery of high-T_c superconductivity (HTS) in the cuprate compound $La_{2-x}Ba_xCuO_4$, with an onset T_c of about 35 K, in 1986 by Bednorz and Müller [34], was followed by the discovery of copper-oxide compounds with higher and higher transition temperature. This gave rise to great interest in these materials due to the prospect of room temperature superconductivity and to its practical applications. The only fact that they could work with the much cheaper cryogenic liquid Nitrogen has made this class of materials one of the most studied at all. However, early excitation was placated by the hard realities of these new materials due to several reasons. Indeed, these materials show a value of the coherence length very small compared to the unit cell size and a large number of degrees of freedom in the preparation of the compounds, which facilitate to have defects inside them.

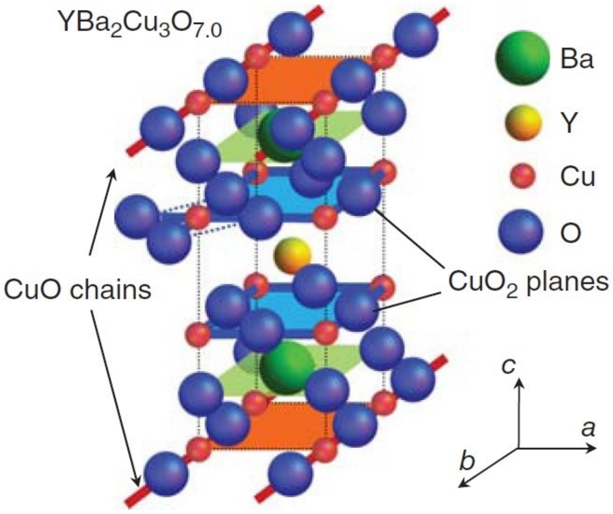

Fig. 1.13: Crystal structure of $YBa_2Cu_3O_7$ [80].

The many HTS cuprate compounds discovered after 1986 share some main aspects [91]. First, the presence of CuO_2 planes in their crystal structure (Fig. 1.13), which are responsible for the conduction phenomena. Second, the undoped cuprates are antiferromagnetic Mott insulators (i.e. a material in which conductivity vanishes as temperature tends to zero, while band theory would predict it to be metallic) and high-T_c superconductivity is created by doping them adding charge carriers. Being these charge carriers holes or electrons, the cuprates are thus classified as either hole- or electron-doped. Third, conventional BCS theory cannot explain the behaviour exhibited by them and new models have been proposed, which are still under debate.

After the discovery of copper oxide superconductors and the success for their high critical temperature, the demand for new superconductors was still high because, in addition to an ever-increasing critical temperature, new technological requirements need higher critical fields.

The discovery of the iron-based superconductors (IBSCs) by the Tokyo Institute of Technology (TIT) group in 2008 had striking impact because superconductivity occurs in materials including iron (Fe) that is a ferromagnetic element, which usually breaks Cooper pairs. In the last years, it has become clear that iron-based compounds are compatible with superconductivity under certain conditions. Moreover, there is a large variety in candidate materials and in pairing interaction, and many new superconductors have been discovered in this family in few years. Thus, it is still high the possibility of finding new superconductors with better physical characteristics.

There are many features of iron-based superconductors such as strength to impurities, a high upper critical field even close to the critical temperature, high magnetic field isotropy and an excellent grain boundary nature which are advantageous for wire application and allow IBSC wires to reach maximal critical currents under high magnetic field making them real competitors to cuprate high temperature superconductors. Moreover, in spite they have lower critical temperatures (the highest T_c for this class has been reported to be about 55 K [92]) compared to those of HTSs, almost all iron-based superconductors are not affected by technical hurdles such as the metal-insulator transition or the d-wave symmetry of the order parameter, which can limit their applications [92-94].

The first iron-based superconductor prototype, discovered in 2006, was the compound LaFePO with a T_c of 4 K [95]. Two years later was found the first high-temperature iron-based superconductor LaFeAsO which, after electron doping through substitution of O with F, reached the T_c at 26 K [41].

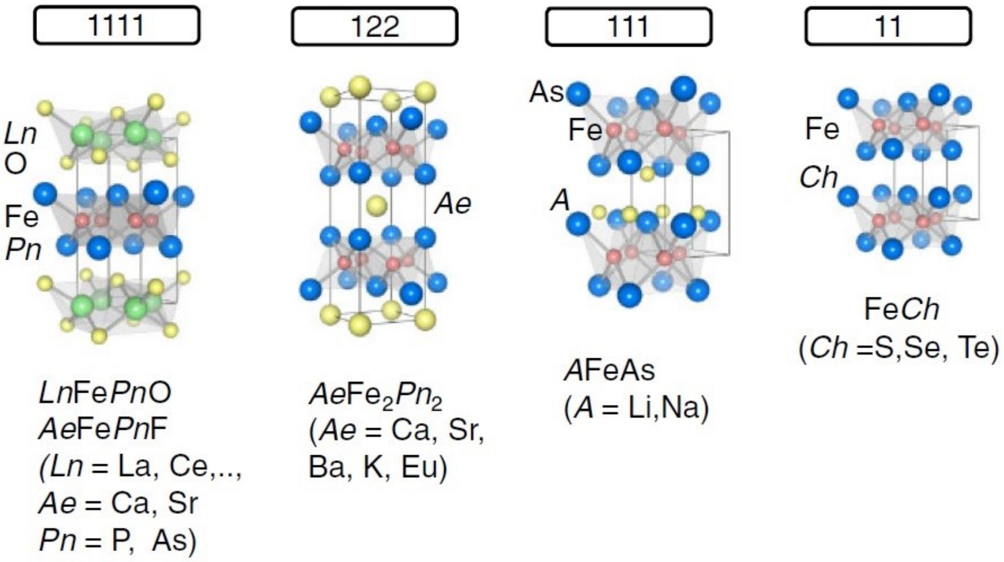

Fig. 1.14: Crystal structures of representative iron-based superconductors, 1111, 122, 111, 11 type compounds [94].

Until now, iron-based compounds have been distinguished in four main families of crystal structures identified by their atomic ratio (see Fig. 1.14):

- 1111 family, with generic compound *Ln*FeAsO, where Ln = lanthanides [96-97]; consisting of an alternate stack of FeAs (or in general Fe*Pn*, with *Pn* = pnictogen) and *Ln*O layers. The highest critical temperature T_c is about 55 K, that is the maximum ever reached by iron-based compounds and was obtained substituting La with another lanthanide element, i.e. SmFeAs(O,F) and NdFeAsO [43].

- 122 family, with generic compound $Ae\mathrm{Fe_2As_2}$, where Ae = alkaline earth metal [98-99]; consisting of alternate FePn stack and alkaline-earth layers too, but with the $\mathrm{ThCr_2Si_2}$ structure. The highest critical temperature for compounds belonging to this family is T_c = 30 K of $\mathrm{K_xFe_{2-y}Se_2}$ compounds.
- 111 family, with generic compound AFeAs, where A = alkali metal [100]. It has the CeFeSi structure and presents the highest T_c at 18 K.
- 11 family, with generic compound FeCh, where Ch = chalcogen ion [94]. It has the simplest FeSe structure called β-FeSe. With a slight excess of Fe, the compound T_c is at least 8 K, while under pressure it can reach T_c = 37 K.

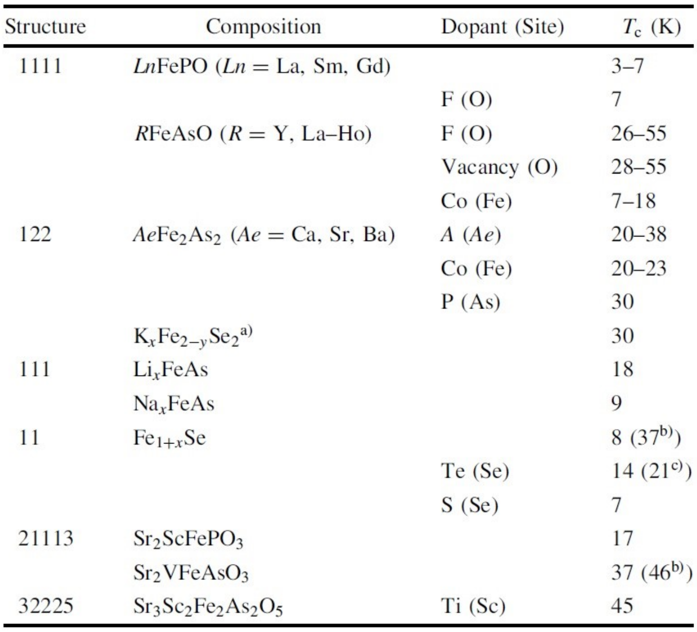

Structure	Composition	Dopant (Site)	T_c (K)
1111	LnFePO (Ln = La, Sm, Gd)		3–7
		F (O)	7
	RFeAsO (R = Y, La–Ho)	F (O)	26–55
		Vacancy (O)	28–55
		Co (Fe)	7–18
122	$Ae\mathrm{Fe_2As_2}$ (Ae = Ca, Sr, Ba)	A (Ae)	20–38
		Co (Fe)	20–23
		P (As)	30
	$\mathrm{K_xFe_{2-y}Se_2}$[a)]		30
111	$\mathrm{Li_xFeAs}$		18
	$\mathrm{Na_xFeAs}$		9
11	$\mathrm{Fe_{1+x}Se}$		8 (37[b)])
		Te (Se)	14 (21[c)])
		S (Se)	7
21113	$\mathrm{Sr_2ScFePO_3}$		17
	$\mathrm{Sr_2VFeAsO_3}$		37 (46[b)])
32225	$\mathrm{Sr_3Sc_2Fe_2As_2O_5}$	Ti (Sc)	45

Table 1.2: Structure, composition, dopant species, and Tc values for representative iron-based superconductors [94].

More complex structures with a longer c-axis and a perovskite-like block layers have also been synthesized. For example, the compounds $\mathrm{Sr_2VFeAsO_3}$, T_c = 37 K [101], and $\mathrm{Sr_3Sc_2Fe_2As_2O_5}$, T_c = 45 K [102] belong to the '21113' and the '32225' structures respectively. In Table 1.2, the structure, composition, dopant species, and T_c values for representative iron-based superconductors are summarized. The differences from the cuprates are: the presence of square lattices of iron atoms which have a tetrahedral bond with either phosphorus, arsenic, selenium, or tellurium anions arranged above and below the planar iron layer, while in cuprates we found a planar copper oxide structure; the metallic nature of parent compounds while the cuprate ones are Mott insulators; the possibility of doping the compound directly in active block while in cuprates the doping occurs in the reservoir block.

Electronic and magnetic properties are determined by the tetrahedral geometry and superconducting properties change by controlling several parameters such as strain, pressure or chemical substitution. As in the cuprates, the pair mechanism shows an unconventional nature and is still under debate. Some studies suggest that the pairing mechanism is attributed to spin fluctuations, which mediates pair scattering between electron and hole regions and leads to the so-called $s_{\pm}$ symmetry of order parameter [103-104]. However, a different pairing mechanism has been proposed based on orbital fluctuation [105]. In this case, an order parameter with s_{++} symmetry is more accredited.

Concerning superconducting properties, the most notable feature shown by iron-based superconductors is the high upper critical field value H_{c2}. Moreover, the slope of $\mu_0 H_{c2}^{\|c}(\mathrm{T})$ is very large around T_c $(2-2.5T/K)$ [106]. The in-plane coherence length, determined using the G-L relation $\xi_{ab} = \left[\Phi_0 / \left(2\pi\mu_0 \left(dH_{c2}^{\|c}/dT\right)\big|_{T_c} T_c\right)\right]^{1/2}$, is between 1.2 nm for 11 type, 1.8-2.3 nm for 122 type and 1.5-2.4 nm for 1111 type compounds and are slightly larger than in the cuprate compounds, despite the latter ones have higher T_c [106-108].

One of the most interesting families of iron-based superconductors for both basic physics and high-field applications is the iron-chalcogenide 11-family of FeSe [109-110]. Unlike the iron pnictides, containing arsenic, they combine the advantageous iron-based properties with the absence of poisonous elements in their composition. FeSe exhibits a significant pressure effect because: under external pressure, the T_c can be increased from 8 to 37 K under a pressure of 7 GPa, the highest increase in all iron-based superconductors [111-112]. Moreover, although in several FeSe crystals a high T_c has already reached around 10 K [113], very recently it has been claimed that much higher T_c (from about 80 to 100 K) can be obtained in single-layer FeSe films [114], making this compound potentially first iron-based 'nitrogen' superconductor.

Moreover, by substituting Te to Se, the doped $FeSe_{1-x}Te_x$ compound [in the following Fe(Se,Te)] is obtained which is characterized by a higher critical temperature ($T_c \sim 15$ K at x = 0.5) and higher upper critical field slope [115-116]. Assuming FeSe as the parent compound, the doping dependent phase diagram for $FeSe_xTe_{1-x}$ is shown in Fig. 1.15 *a*) [117]. It shows that the antiferromagnetic phase disappears at about 10% Se substitution. At 10 to 30% Se substitution, filamentary superconductivity emerges, turning into bulk superconductivity at higher x values. Unlike FeSe, $FeSe_{0.5}Te_{0.5}$ does not show improvements in T_c under pressure. As concerning thin films, early work on FeSe or Fe(Se,Te) seemed to indicate that it is relatively difficult to acquire high quality epitaxial thin films with critical temperatures as high as those of single crystals [118-120]. However, recent experiments have shown higher T_c values in thin films than in bulk iron chalcogenides [121-124].

Superconducting thin films have been fabricated mostly by pulsed laser deposition (PLD). The successful growth of thin films of iron chalcogenides tapes or coated conductors will boost their use for large scale applications [125]. Improvement of the fabrication techniques has led to an enhancement in the current-carrying capability of polycrystalline bulk, which looks promising in terms of wire production [15, 126]. It is thought that iron superconductors may be a more competitive candidate to replace Nb-based superconductors for high field applications at liquid helium temperatures (see the comparing in Fig. 1.15 b).

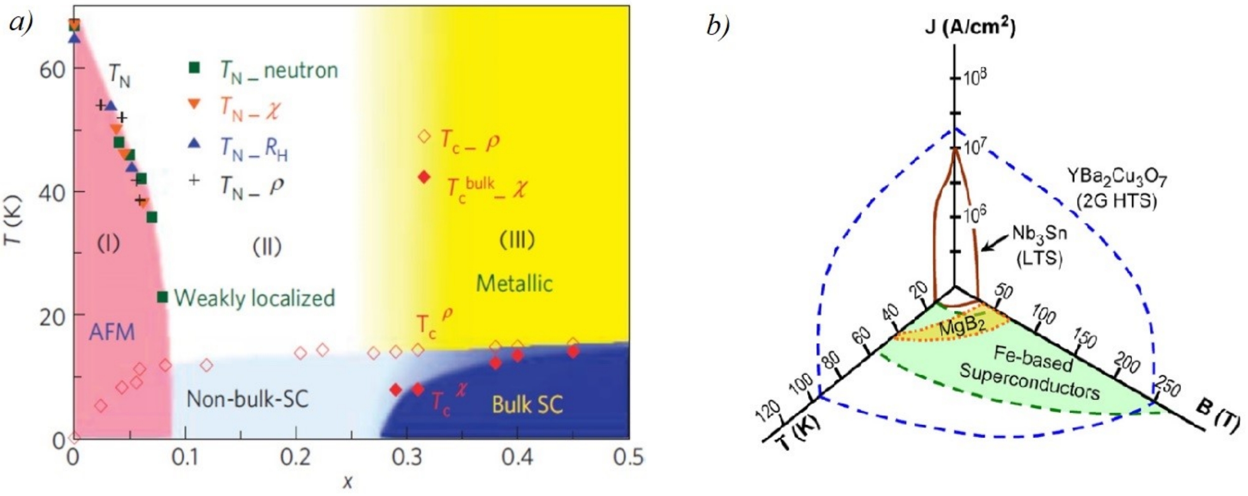

Fig. 1.15: a) Phase diagram for $FeSe_xTe_{1-x}$ system, AFM: antiferromagnetism, Sc: superconductivity. The Néel temperature T_N of the AFM phase, determined by neutron scattering (T_N_neutron), susceptibility (T_N_χ), Hall coefficient (T_N_R_H) and resistivity (T_N_ρ) [117]. b) Electrical current density-temperature-magnetic field plot of Nb3Sn (LTS), $YBa_2Cu_3O_7$, MgB2 (HTS) and Iron-based superconductors with their respective critical parameters approximated by the contour lines [110].

1.3 Electrical Characterization of Iron-Chalcogenides Superconductors

Several studies have been performed to elucidate the nature of superconductivity in Fe-chalcogenides [92, 127], however, the characterization of samples through electrical transport measurements can provide us with very interesting information in terms of applications. For example, a deep analysis of the superconducting vortex phase diagram is necessary in order to reach a full understanding and control of the high current transport in these materials. A simple but powerful tool to investigate vortex line dynamics is to perform electrical resistance measurements as a function of temperature at fixed magnetic fields. This allows the identification of the irreversibility line $H_{irr}(T)$ and the line of the upper critical field $H_{c2}(T)$, defined by the standard criterion $R(T, H_{irr}) = 0.1R_N$ and $R(T, H_{c2}) = 0.9R_N$, where R_N is the normal state resistance at the onset. In Fig. 1.16, the H-T phase diagram of the three different Fe(Se,Te) samples is shown [17]. The H_{irr} lines can be well fitted by a power relationship $H_{irr}(t) = H_{irr}(0)(1-t)^{\beta}$ where t is the reduced temperature $t = T/T(H_{irr} = 0)$ and thus it is possible to confidently extrapolate the H_{irr} values.

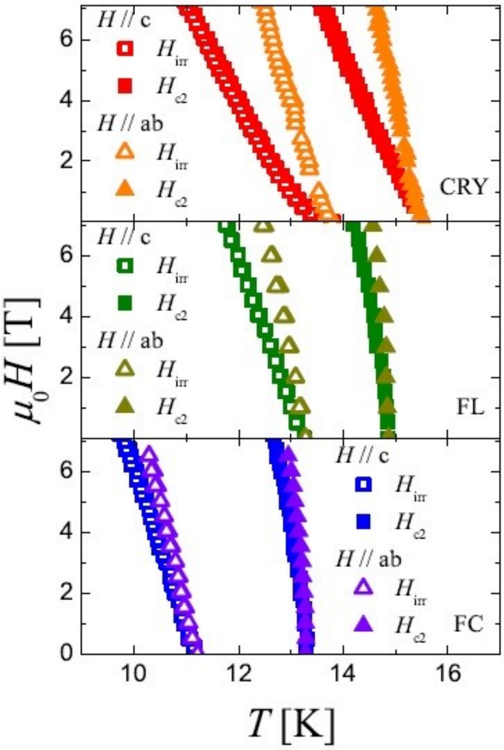

Fig. 1.16: Comparison of T-H phase diagram of three different Fe(Se,Te) samples, namely a single crystal (labelled with CRY), thin film on LaALO$_3$ substrate (labelled with FL), and thin film on CaF2 substrate (labelled with FC). $H_{c2}(T)$ (full symbols) and Hirr(T) (open symbols) curves of the three samples are indicated for applied field parallel to sample c-axis (squares) and to sample ab-plane (triangles) [17].

The pinning properties can be studied starting from the possible scaling of the normalized pinning force ($f_p = F_p/F_{p,max}$) as a function of the normalized magnetic field ($h = H/H_{irr}$) at different temperatures. Starting by eq. (1.25) $F_P = J_c B$, the $f_P(h)$ curves of the Fe(Se,Te) sample can be evaluated from J_c

measured by current-voltage characteristics or by magnetization measurements. The pinning force can be represented by the Dew-Hughes scaling law $f_p \propto h^p(1-h)^q$, which it is possible to correct because the particular nature of their intrinsic pinning centers [60]. In Fig. 1.17 is shown the *$f_p(h)$* experimental curves fitted by Dew-Hughes model with p = 0.8 and q = 2.1, quite close to the expected p = 1 and q = 2 for the case of normal-core and point pinning [18]. The *J_c* experimental values are obtained by electrical transport measurements.

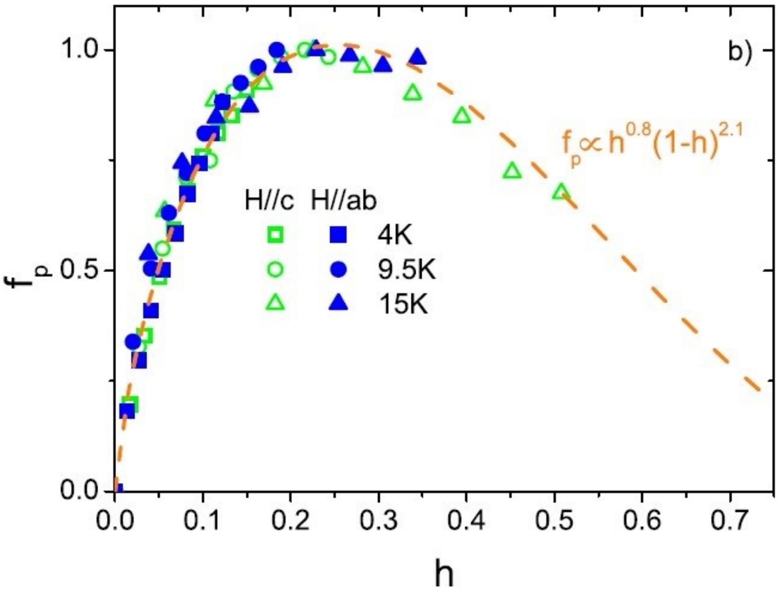

Fig. 1.17: The relative normalized pinning force as a function of the reduced magnetic field H/Hirr. The curves are fitted by Dew-Huges relation [18].

Another important physical quantity that characterizes vortex pinning is the pinning activation energy U. It can be estimated through the analysis of the R(T) curves at different applied magnetic field. In the mixed dissipative state, the vortices motion is described by the thermal activated flux flow, where the resistivity is described starting by the eq. (1.26) and (1.27), taking into account the simplifying hypothesis introduced for HTSC considered valid also for iron-based superconductors [128]:

$$R(T,H,J) = R_0\, exp\left[-\frac{U_0(T,H,J)}{k_B T}\right] \tag{1.48}$$

Thus, once the current density J is fixed, it is possible to estimate the pinning activation energy curve $U_0(T,H,J)$ by the Arrhenius plot, which is obtained by plotting $ln\, R(T,H,J) = lnR_0 - U_0(T,H,J)/k_B T$, with lnR versus $1/T$ of the resistance data. The Fe(Se,Te) thin film *U_0* values estimated by the linear fit are plotted as a function of the inverse of the applied magnetic field in Fig. 1.18. The data are usually fitted by a power law $U_0 \propto H^{-\alpha}$ but, as shown in the figure, a single exponent is not sufficient to fit the data in the whole magnetic field range. Indeed, in the literature data on U_0, a crossover from individual pinning regime ($\alpha < 0.5$) to collective pinning regime ($\alpha > 0.5$) is always observed [107, 129].

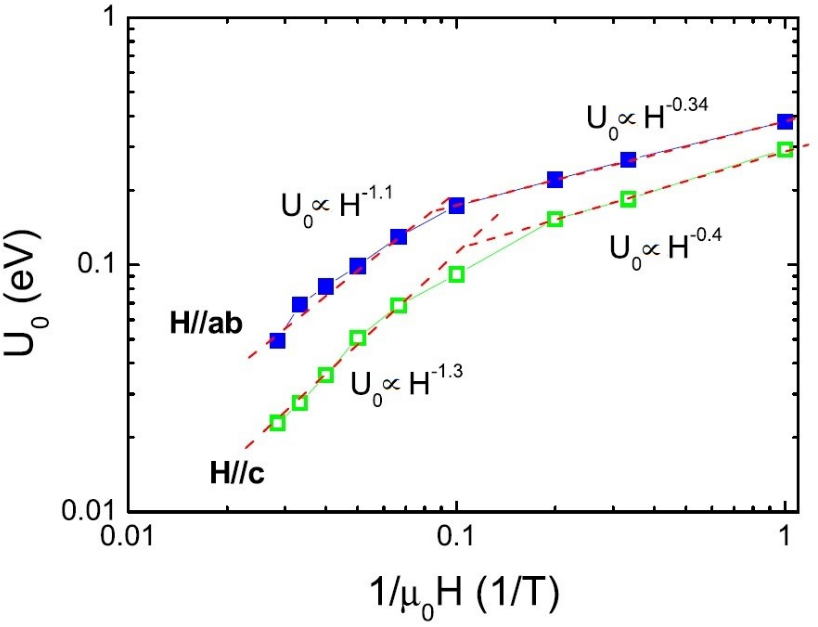

Fig. 1.18: Vortex motion activation energy as a function of the inverse of the field in parallel (blue full symbols) and perpendicular (green empty symbols) configurations as extracted from the Arrhenius plot [18].

1.4 Technical Superconductors

Superconducting technology represents a great opportunity for the development of high efficiency applications. Due to their high-power density and low losses, technical superconductors (i. e. wires and tapes) allow to minimize the volume and weight of superconducting devices, compared to those based on traditional materials.

Technological applications development needs the expansion of the critical surface as far as possible. Besides the efforts to obtain ever-increasing T_c, much progress has also been made in obtaining higher critical fields H_{c2} and, above all, a higher critical current J_c. The maximum possible value of J_c is the depairing current J_{dp}, which is determined by the microscopic material properties [130, 131]. In real technical superconductors, the value of J_c is determined by the superconducting material pinning properties, thus great efforts have been devoted to improve the performance of superconductors by acting on effective pinning mechanisms. Moreover, in choosing the suitable superconducting material and the best wire design for a certain type of application, there are many other parameters to refer, such as the engineering critical current density J_E [132], i. e. the critical current density calculated in the whole conductor cross section (see Fig. 1.19). Obviously, these parameters are however linked to the superconducting material fundamental properties.

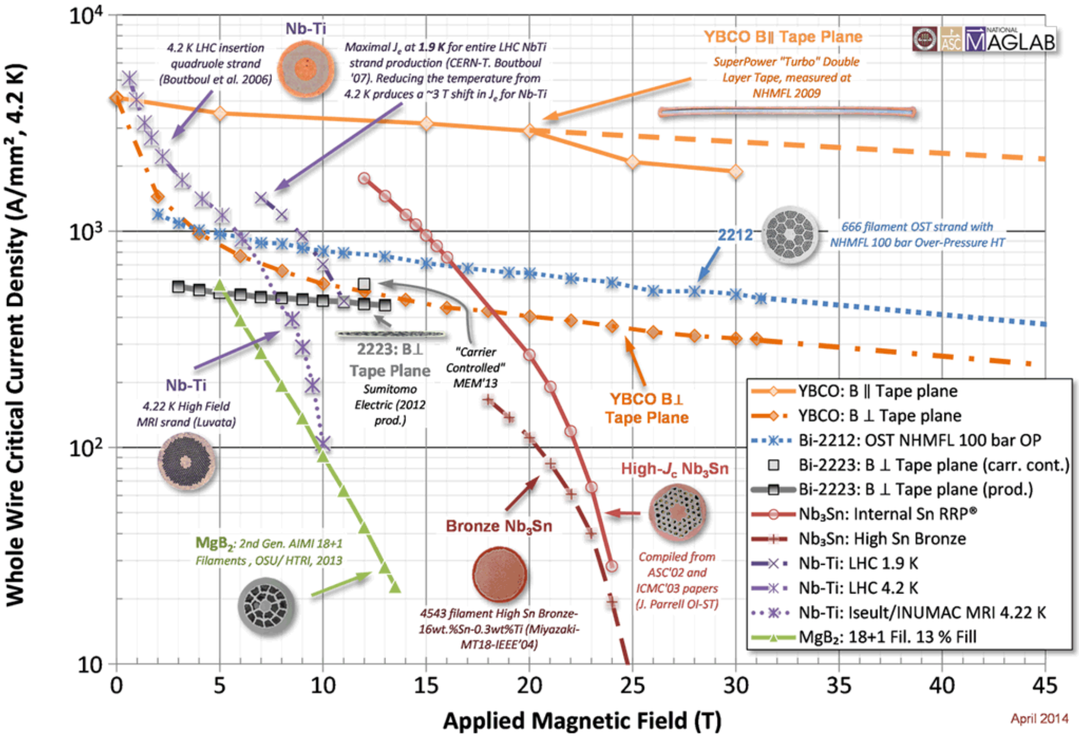

Fig. 1.19: Engineering Critical Current Density vs Applied Field [132]

The use of superconducting wires for large scale applications is conditioned by the possibility to manufacture very long cables (up to kilometers in length) based on wires with high values of J_c and H_{c2}.

Most of the large-scale devices rely on NbTi and Nb_3Sn superconducting cables, which require liquid helium for cooling. Recently, great attention has been devoted to HTS cables, based on BISCCO wires and REBCO tapes [133-134]. Compared to LTS, HTS exhibit higher values of H_{c2}, J_c, specific heat, thermal conductivity, and lower required refrigeration power (they can operate in the range 20 K–77 K, depending on the operating magnetic field), which makes them suitable for high field applications above 15 T.

Wires and tapes

In general, practical superconductors are composite wires containing a normal metal matrix in which superconducting filaments are embedded. Indeed, this special design is required by the several issues which are briefly discussed below [14, 80].

It is well known that in a magnetic field, to avoid losses in transport current due to the Lorentz force, the flux lines must be pinned. Therefore, the manufacture of practical conductors based on superconductors requires processes that lead to the introduction of efficient pinning centers in their microstructure to optimize the critical current density [135-138].

As a result of flux pinning, a cylindrical superconductor undergoes an irreversible magnetization whose curve loop width ΔM is proportional to the critical current density J_c and to its diameter d. Due to the screening currents, a magnetic energy proportional to $(\Delta M)^2$ is stored in the cylinder. An increase in temperature due to a small distortion leads to a lowering of the J_c and changes the flux distribution on the filaments, leading to further temperature increase, with the risk of triggering an avalanche process called *flux jump*. The condition to avoiding this process, under adiabatic condition, consists in a small value of $(\Delta M)^2$ compared with the volumetric specific heat C_v that is typically small at the operating temperature. The request to obtain the highest possible J_c without prejudice to stability, implies that d must be limited. For example, the most conservative NbTi magnets have filaments with a d = 30 - 50 µm, and d = 3 – 5 µm for Nb_3Sn, but the diameter values depend on the maximum field reached and on the ratio of the metal matrix, too. Thus, technical conductors consist of many superconducting filaments (typically from ~20 to ~100000) embedded in a normal metal matrix.

The normal metal matrix, typically, is made of copper or silver due to their very good electrical and thermal conductivity and ductility. The choice of one or the other material is however dictated by the problems related to the manufacture of each material. A good electrical conductivity provides greater dynamic stability that disadvantages flux jumping. The metal matrix has multiple functions since it allows the redistribution of the current if a filament is interrupted, it is the medium through which the heat is transferred, and it dampens the variations of the magnetic field. However, it also has the unintended effect to couple electromagnetically the filaments in a variable magnetic field. Since the filaments must be magnetically decoupled to avoid flux jumping, they must be twisted around their own axis with a pitch L_p. For mechanical reasons, $L_p \geq 5D_w$, where D_w is the diameter of the fraction of the transversal area occupied by the filaments. In addition, the overall size of the matrix is also limited due to the magnetic energy due to the self-field. It is proportional to $(\lambda \cdot J_c \cdot D_w)^2$ where λ is the filling factor of the superconductor in the matrix. For example, in the case of a high λ, the stable diameter of a NbTi wire is below 2 mm, while for a Nb_3Sn wire is below 1 mm.

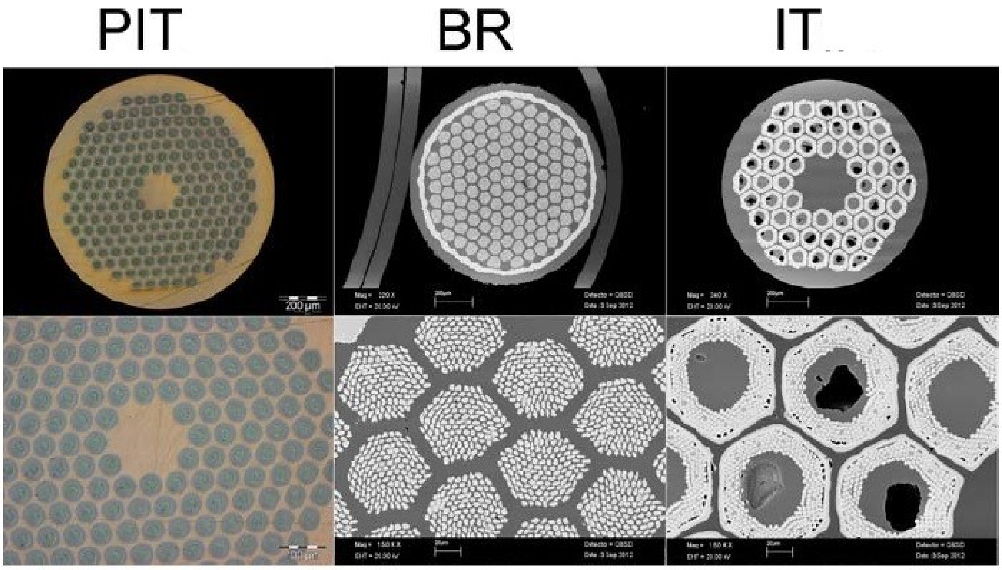

Fig. 1.20: Micrographs of the transverse cross-sections of Nb_3SN wires produced by different techniques, namely PIT, BR, IT [154]

The metal matrix in a composite wire is also useful as a mechanical strengthening and for the conductor protection against quench. Indeed, if the superconducting filaments switch to the normal phase, their large normal state resistance would lead to burning them. The presence of a normal metal such as copper or silver would allow the current to flow through the matrix preserving the filaments.

The fabrication of multifilamentary wires involves several hot- and cold-working processes and steps well established, during which purity of the used materials and cleanliness are required. The implementation of industrial production has essentially led to three processes, namely Bronze Route (BR) [139], Internal Tin process (IT) [140], Powder-in-Tube method (PiT) [141] (see Fig. 1.20).

LTS wires

The LTS NbTi is the ideal material for the manufacture of filaments for its high-density critical currents in magnetic fields up to 10 T and at a temperature of 4.2 K, as well as for its workability together with the copper matrix. The Nb_3Sn intermetallic compound, instead, is used to fabricate multifilamentary cables that bear major fields. In fact, these cables can sustain significant currents within 18 T while the top critical range is 22 T (Fig. 1.21). However, their use is more limited because their manufacturing cost is higher than NbTi wires [142].

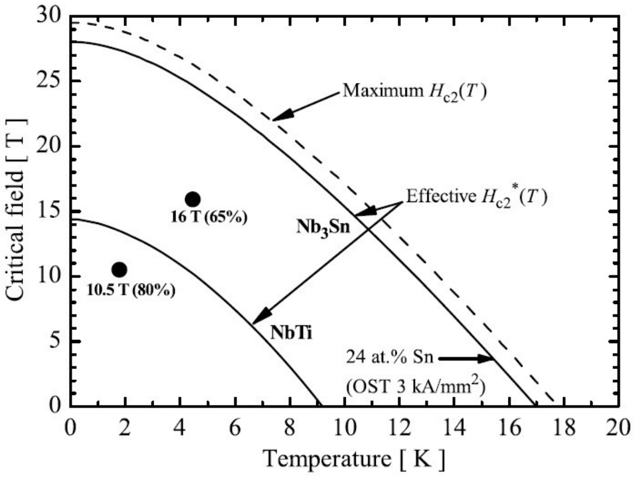

Fig. 1.21: Field-temperature phase boundaries and record magnetic fields in dipole magnets for NbTi and Nb_3Sn [142].

HTS wires and tapes

Due to their small coherence lengths, in HTS it is easier to encounter imperfections that have the size of the ξ and thus can work as pinning centers preventing the resistive regime. However, since technical superconducting materials consist of a network of connected grains, small imperfections at the grain boundaries weakening the superconducting connection among the grains must be avoided in technical conductor by a careful control of the growth process [143]. Moreover, the misalignment angle of the grains leads to a degradation of the supercurrent transport, which is accentuated if it is also present an accumulation of charge inhomogeneities as recent microscopic modelling have identified [144]. This weak-link behaviour requires the manufacture of technical conductors with perfectly aligned single-crystalline materials such as epitaxial films and well-textured bulk material.

Applications in electric power area, such as magnets, motors and power-transmission lines require that technical superconductors would substitute copper wires. This implies that superconducting material is formed into a long, strong and flexible conductor, while the HTS materials, unlike the metals, are non-ductile and non-malleable ceramics.

BSCCO wires and tapes

To fabricate a technical superconductor the basic idea is to pack BiSrCaCuO (BSCCO) superconducting powder in Ag tubes which subsequently undergo several mechanical deformation steps of drawing and rolling with intermediate annealing process. The resulting product, in tape or wire forms, can carry over 100 A at 77 K and is equipped with the necessary flexibility given by the silver matrix which even short-circuits unavoidable microcracks occurring in the BSCCO filaments. Nevertheless, this results in small resistive voltage drops that do not allow to operate persistently. Moreover, the amount of silver used for making the wires and the fact that at 77 K the current that can circulate in the magnetic field is considerably reduced, make the use of these cables restricted to some applications only.

The increase of the engineering critical current density J_E has made $Bi_2Sr_2CaCu_2O_{8+x}$ (Bi-2212) a reliable candidate for solenoids and accelerator magnets able to generate magnetic fields unattainable with low-temperature superconductors. The difficulties in achieving the huge potential for applications envisaged in the early 1990s. They were overcome when it was seen that a passage through the melt phase of Bi-2212, could produce a self-organized local grain alignment with a much higher J_c than was possible in randomly oriented polycrystals [145]. However, the J_c suffered a limiting mechanism due to bubbles formation during the melting process. Bubbles formation is prevented by applying a sufficient overpressure during the heat treatment which also has the function of fully densifying the 2212 powders [146-147]. The reaction under pressures up to 100 bar can raise the engineering current density J_E by up to 8 times (J_E reaches almost 1,000 Amm^{-2} at 4.2 K and 5 T) [21].

Mechanical, thermal and electrical stability of the Bi-2212 are important features that must be studied for high-field applications [23, 147]. The residual-resistivity ratio of the normal-metal matrix is a key parameter for both the thermal and the electrical stabilities. In Bi-2212 wires, the thermal transport at cryogenic temperatures is dominated by the contribution of Ag, because of the low κ of the Bi-2212 phase and of the Ag alloys normally used to strengthen the conductor. A correlation between the so called residual resistivity ratio $RRR = \rho(273\ K)/\rho_{res}$ and κ is observed, indeed, the higher the RRR, the higher the κ [148]. Thus, high RRR is desired to protect superconducting magnets in case of quench, as the Joule heating generation term is proportional to the electrical resistivity (ρ) of the normal matrix [79, 149]. An open issue about Bi-2212 conductors is understanding to what extent the Ag matrix is contaminated during the heat treatment due to Bi-2212 element diffusion.

REBCO Coated Conductors

A second-generation wire much more competitive than those using a metallic matrix were developed. The second-generation wire, also referred as Coated Conductors (CC), consists in thin metal tapes on which it is epitaxially grown an $YBa_2Cu_3O_{7-\delta}$ (YBCO) coating. This coating carries much higher current in a magnetic field and very little silver is needed, getting significant cost reductions [150]. The optimization of production systems has led to the possibility of producing these second-generation tapes in long lengths with the performance required for commercial applications, but the rather complicated fabrication process makes the production of coated conductors still quite expensive. Anyway, although not all the problems with the use of cuprate HTS have been resolved, within the next few years they are going to become the most important materials for the realization of technical conductor [151].

Iron-based wires and tapes

As concerning Iron-based materials, wire and tape applications have been tried and significant progresses have been made. The fabrication of superconducting wires is based on the PIT method and a J_c of approximately 10^4 A/cm^2 has been obtained with a slow reduction of J_c in high magnetic fields [152]. It has been recently demonstrated that it is possible to realize coated conductors based on iron-chalcogenides able to carry very high current densities (critical current densities J_c at 4.2 K and 30 T up to 10^5 A cm^{-2}) [15], and that it is possible to improve this performance by choosing the right buffer layer [16-18].

1.5 Thermal Characterization of Technical Superconductors

Thermal Conductivity and RRR

Thermal transport in composite conductors can be treated with a formalism analogous to the case of electrical resistances connected in parallel. The overall longitudinal thermal conductivity (κ_{tot}) is the weighted sum of the thermal conductivity of each material composing the conductor $\kappa_{tot} = \sum \kappa_i \, s_i$, the weight being the surface fraction $s_i \equiv S_i / S_{tot}$, where S_i and S_{tot} are the surface of the cross section occupied by the i-th component and the total cross section area of the conductor, respectively. For this reason, if a local heating of a superconducting wire occurs during operation, heat transfer through the conductor is the main channel for distributing heat and, consequently, preventing a quench.

It can be found that in metals the so called residual resistivity ratio $RRR = \rho(273\ K)/\rho_{res}$ can describe the temperature dependence of thermal conductivity κ [148]. For example, for the copper, the temperature dependence of κ can be predicted within 15% by the following expression:

$$\kappa_{Cu} = (W_0 + W_i + W_{i0})^{-1} \tag{1.49}$$

where

$$W_0 = \frac{\beta}{T}, \qquad W_i = \frac{P_1 T^{P_2}}{\left(1 + P_1 P_3 T^{(P_2+P_4)} e^{-\left(\frac{P_5}{T}\right)^{P_6}}\right)}, \qquad W_{io} = P_7 \frac{W_i W_0}{W_i + W_0} \tag{1.50}$$

with $\beta \approx 0.634/RRR$, $P_1 = 1.754 \cdot 10^{-8}$, $P_2 = 2.763$, $P_3 = 1102$, $P_4 = -0.165$, $P_5 = 70$, $P_6 = 1.756$, $P_7 \approx 0.235\ RRR^{0.1661}$ in SI units [148]. W_0 and W_i represent the electron-defect and the electron-lattice scattering contributions, respectively. W_{i0} is an interaction term between W_0 and W_i. In Fig. 1.22, the thermal conductivity as a function of temperature curves at various RRR calculated from equation (1.49) and (1.50) are shown [153]. As a consequence, for superconducting magnet design is crucial the study of the temperature and magnetic field dependence of technical superconductors thermal conductivity that can be done investigating the thermal conductivity of the normal metal present in the samples, κ_{metal}, by supposing that $\kappa_{meas} \approx \kappa_{metal} s_{metal}$ [154-156]. The comparison of the $\kappa(T)$ curves, measured at different magnetic field values, points out that the differences in the thermal properties of technical superconductors are strongly reduced after the application of an intense magnetic field (see Fig. 1.23).

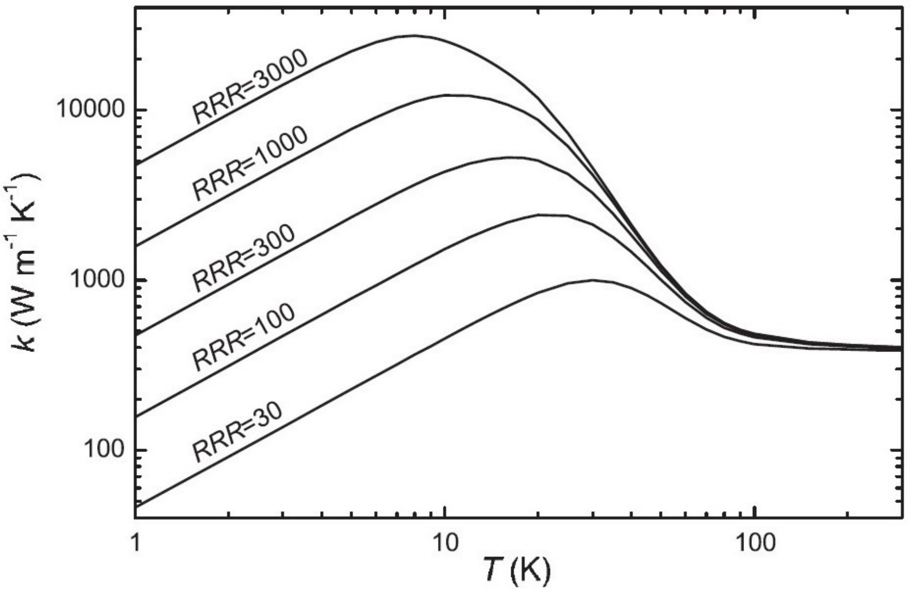

Fig. 1.22: Temperature dependence of the thermal conductivity at zero magnetic field expected for copper with different RRR. Curves have been derived from equations (1.49), (1.50) [153].

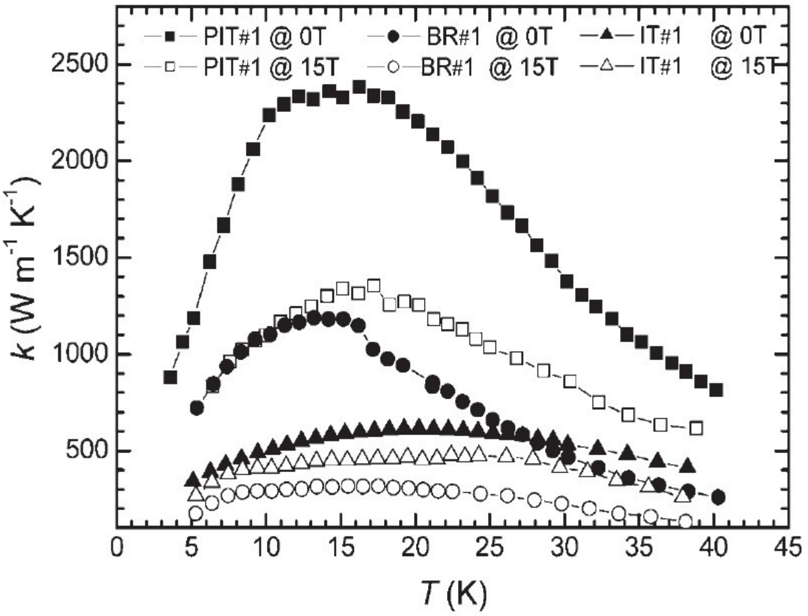

Fig. 1.23: Thermal conductivity as a function of temperature for three Nb3Sn wires fabricated with different techniques, namely PIT, BR, IT, acquired at μ_0H = 0 T (full symbols) and μ_0H = 15 T (open symbols) [154].

The reduction of κ upon increasing the magnetic field can be qualitatively understood considering that the thermal conductivity of normal metals at low temperatures is proportional to the electron mean free path. The latter decreases with the magnetic field because of the action of the Lorenz force on the charge carriers. The Wiedemann-Franz law defines quantitatively the correlation between the thermal conductivity and the electrical resistivity in metals: $L = \kappa\rho/T$, that at low temperatures is $L = L_0 = \frac{\pi^2}{3}\left(\frac{k_B}{e}\right)^2 \approx 2.44 \times 10^{-8} \mathrm{W\Omega K^{-2}}$, where L is the Lorenz number where k_B is the Boltzmann constant and *e* is the electron charge [157]. At very low temperatures, the constant electrical resistivity value $\rho = \rho_{res}$ implies that κ is expected to increase linearly with T. On further increasing the temperature, ρ starts increasing as T^n with $n > 1$, implying a consequent reduction of κ. As the temperature range where $\rho = \rho_{res}$ is wider for low RRR values, it follows that dirtier samples have higher T_{max}.

Predictions of the Wiedemann-Franz law are in good agreement with experiments at low temperatures and zero magnetic field, provided that the phonon contribution to thermal transport is negligible and that electron scattering processes are elastic [158-159]. In the case of Ag, very few studies are present in the literature and show that L varies with T going from $L \approx 2.4 \times 10^{-8}\, W\Omega K^{-2}$ at 2 K to $L \approx 1 \times 10^{-8}\, W\Omega K^{-2}$ at 15 K [160-161]. To the best of our knowledge, there are no published data over a wider range of cryogenic temperatures or at fields higher than 0.5 T [160]. The field-induced reduction of κ can be viewed in the framework of the Wiedemann-Franz law as a consequence of the increase of ρ due to magneto-resistance effects [26-162].

NZPV in REBCO CC

Recently, based on a study of the thermo-physical properties, a practical formula for the normal zone propagation velocity appropriate for REBCO coated conductors in high magnetic fields have been derived [149]. It takes into account the fact that in HTS, T_t assumes values higher than 45 K. In this range of temperatures, the derivative of κ(T) is strongly reduced on increasing the field and so the term in the eq. (1.45) can be neglected respect to $C_n(T_t)$

$$\frac{1}{\kappa_n(T_t)} \frac{d\kappa_n}{dT}\bigg|_{T=T_t} \times \int_{T_{Op}}^{T_t} C_S(T)dT \ll C_n(T_t) \qquad (1.51)$$

and the expression (1.45) for *NZPV* becomes the approximated *NZPV'*:

$$NZPV' \approx J\left[\frac{\rho(T_t)\kappa(T_t)}{C(T_t)\int_{T_{Op}}^{T_t} C(T)\,dT}\right]^{1/2} \qquad (1.52)$$

The relative error made in using eq. (1.52) in place of eq. (1.45) is a function of T_t for given operative conditions (T_{Op}, B). Indeed, we can rewrite the (1.45) as:

$$NZPV \propto \sqrt{C_n(T) - \frac{1}{K}\frac{dK}{dT}\bigg|_{T_t} \cdot \int_{T_{Op}}^{T_t} C_s(T)dT} \qquad (1.53)$$

Considering the relation (1.51), the approximated expression *NZPV'* is obtained:

$$NZPV' \propto \sqrt{C_n(T)} \tag{1.54}$$

Thus, the relative error committed can be calculated as:

$$\varepsilon = \frac{NZPV' - NZPV}{NZPV'} = 1 - \frac{NZPV}{NZPV'} =$$

$$= 1 - \sqrt{\frac{C_n(T) - \frac{1}{K}\frac{dK}{dT}\Big|_{T_t} \cdot \int_{T_{Op}}^{T_t} C_s(T)dT}{C_n(T)}} = 1 - \sqrt{1-\Delta} \tag{1.55}$$

where

$$\Delta = \frac{\frac{1}{K}\frac{dK}{dT}\Big|_{T_t} \cdot \int_{T_{Op}}^{T_t} C_s(T)dT}{C_n(T)} \approx \frac{\frac{1}{K}\frac{dK}{dT}\Big|_{T_t} \cdot \int_{T_{Op}}^{T_t} C(T)dT}{C(T)} \tag{1.56}$$

In Fig. 1.24, the relative error made when using equation (1.52) in place of equation (1.48) is plotted as a function of T_t, for different operating conditions (T_{Op}, B). The experimental results obtained for REBCO CCs prove that the error decreases on increasing B and is always smaller than 7 % at 19 T [149].

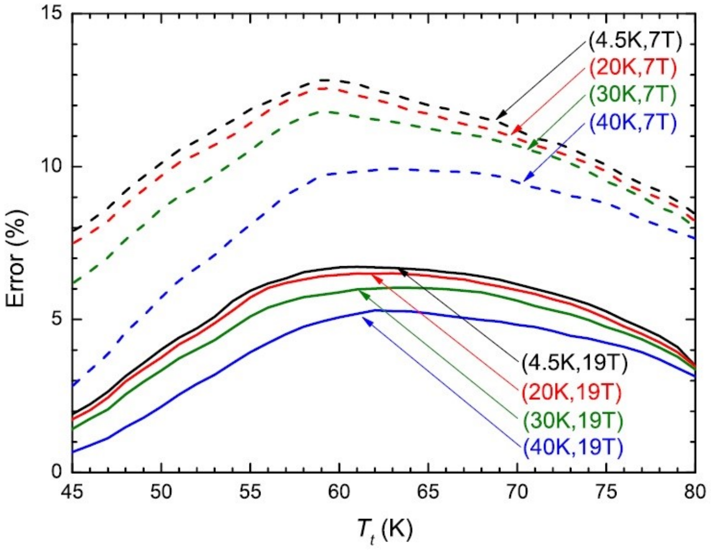

Fig. 1.22: Relative error when using eq. (1.52) in the place of the more general eq. (1.48) for different operating conditions (Top, B), as determined for REBCO CC in ref [149].

2 EXPERIMENTS ON ELECTRICAL AND THERMAL TRANSPORT PROPERTIES

2.1 Introduction to cooling methods

The best cooling method, is supposed to be the direct immersion of the superconductors into a cryogenic liquid bath [163]. This method is useful for cooling samples of any shape such as wires, films, bulk materials, etc. In a typical cooling system (or cryostat), the cryogenic liquid is contained in a vacuum-jacketed dewar to reduce the heat load due to conduction and convection. The temperature of the bath is the boiling temperature at atmospheric pressure, namely 4.2 K for liquid helium (He) or 77 K for liquid nitrogen (N_2), that are the most common cryogenic liquid used. If a lower temperature is required, it is possible to partially evacuate the dewar space above the cryogenic liquid. To make measurement, typically the test sample is attached on a sample holder to the end of a probe-stick equipped with a cryogenic thermometer which is dropped into the thermal bath. For measurements in magnetic field, a normal or superconducting magnet can be inserted in the cryostat in such a way that the sample is in the center of the solenoid (Fig. 2.1). However, the simple thermal bath does not allow either a fine temperature control or a wide range of temperature.

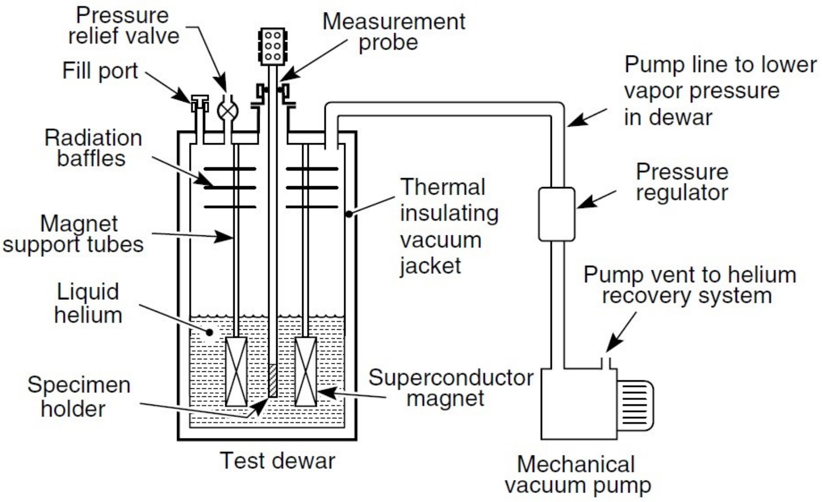

Fig. 2.1: Schematic of an immersion measurement probe in a cryogenic liquid with a vacuum pump for lowering the boiling temperature of the cryogen bath [163].

The need to perform measurements in a temperature range within 1.2 – 300 K with accurate control is met using gas-flow wet cryostats. This kind of cryostats are equipped with a variable temperature insert (VTI), that is a vacuum chamber separated by the cryogenic bath in which the sample is inserted. In the

VTI, the thermal exchange is ensured by means of a He vapor flow taken from the thermal bath and introduced into the VTI by means of a needle valve (Fig. 2.2 (a)).

In the *dynamic gas flow systems*, the sample is in a flowing cryogenic liquid vapor. The temperature can be varied by passing the cryogen through a heat exchanger with a heater and by controlling the gas flow rate [163] [164]. Then, the exhaust gas is evacuated by a pump. Dynamic gas flow systems respond very quickly if the set temperature changes and they also have greater temperature stability during a measurement than the thermal bath.

In addition, to achieve an even greater temperature stability, it can be inserted in the VTI a separate chamber externally cooled by the gas flow flux (Fig. 2.2 (b)). The chamber hosts the sample and is filled with a certain pressure of exchange gas to obtain a *static gas system*. The stability is obtained because rapid temperature changes are filtered out due to the increased time taken to change the sample temperature to a new value.

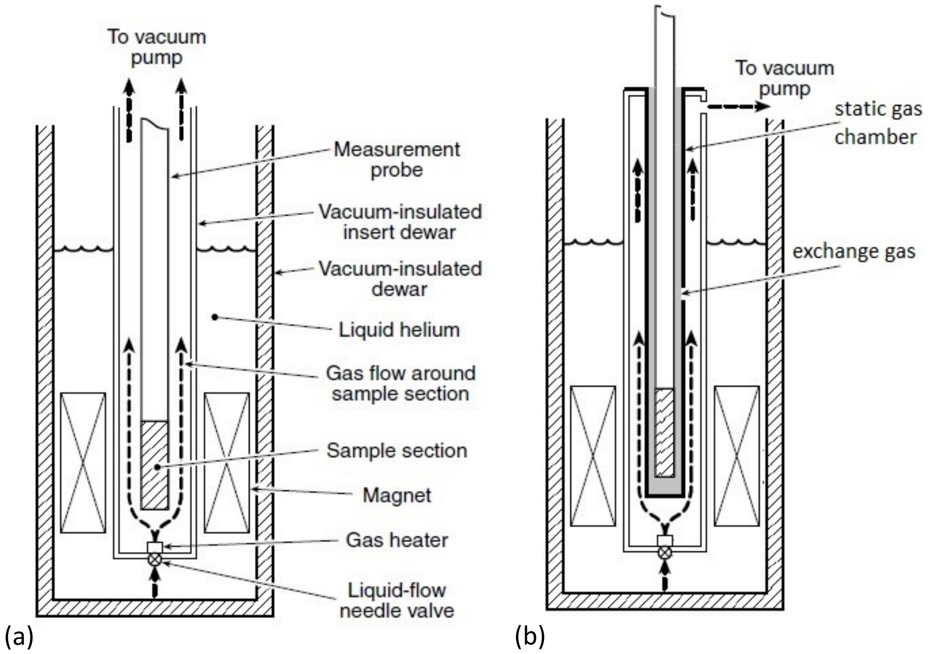

Fig. 2.2: Schematic diagram of a variable temperature cryostat based on continuous flow of cold helium gas (a) directly over the sample and (b) over a static gas chamber hosting the sample [163].

However, liquid He is expensive and its handling requires training for correct use. In industrial application contests, others cooling methods such as cryocooler-based ones are preferred. The cryocooler is a cryogenic refrigerator in which refrigeration is provided by a *closed-loop* system, which eliminates the cost of continually supplying liquid helium and avoiding its problematic handling [163, 165]. The two stage Gifford-McMahon (G-M) refrigerator is one of the most common types of cryocoolers. The cold part of the cryocooler has a cold finger shape and typically in the middle it houses the first stage at 40-80 K and serves as a thermal anchor for a radiation shield that surrounds the second-stage cold head (Fig. 2.3). The second stage typically achieves temperature in the range 3 - 10 K and the cooling power of commercial G-M refrigerators is usually in the range 0.5-2W [163]. G-M cryocoolers advantages are their convenience and absence of cryogenic liquid externally supplied. Their disadvantages are the relative long time needed to reach the required temperature and the significant vibration at the cold head, which can affect the validity of some measurements in addition to being suitable only for low power applications.

A more recent type of closed-loop cryocooler is the Pulse-Tube cryocooler, which has an internal operating design that reduces vibrations and noise of about two orders of magnitude respect to G-M, due to the absence of cold moving parts and offers several significant advantages over other designs [166]. The principle of operation of a Pulse-Tube refrigerator is shown in Fig. 2.4. The basic refrigeration cycle starts with the *piston* (typically located in an external compressor unit) moving down to compress room-temperature helium gas, causing it to flow through a *regenerator* (heat exchanger), where it enters with temperature T_0 and leaves it at the *cold stage* with temperature T_{cold}. Hence, heat is transferred into the regenerator material [163]. Then, it enters the *pulse tube* where it is compressed and, consequently, heated. As gas exits the pulse tube, it is refrigerated to ambient temperature by a heat exchanger at its warm end (T_{hot}). The gas then flows through a flow restriction provided by an *inertance tube* (or a primary orifice, not shown here), and, finally, into a room-temperature *reservoir*. Gas flow out of the pulse tube stops when the pressure in the pulse tube equals the average pressure in the reservoir. Then, the piston moves up causing the reverse flow of gas from the reservoir. In this way, the gas expands in the pulse tube *adiabatically*, cooling down. As the cooled gas flows back through the lower heat exchanger, it absorbs heat from the cold stage. The entire cycle is then repeated.

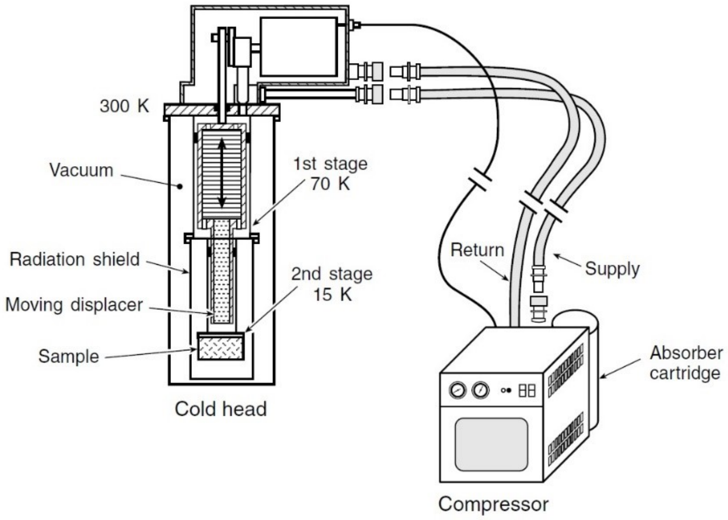

Fig. 2.3: Sample mounted on cooling stage of a commercial Gifford-McMahon (G-M) cryocooler *[163]*.

Cryocoolers are the basic components of the cryogen-free systems. A cryogen-free system is characterized by the presence of a cryostat in which is inserted a VTI but the sprayed cryogen flowing into it is cooled by a cryocooler. Some of these systems are described in the following section.

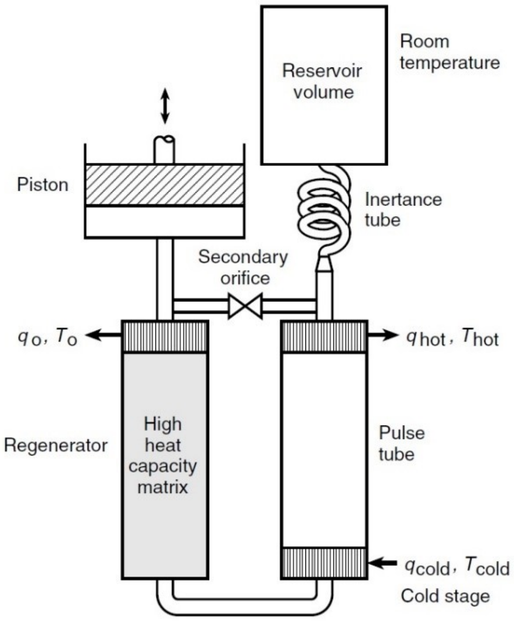

Fig. 2.4: Operation of a Pulse-Tube cryocooler, q is the heat flow and T is the temperature) [163].

2.2 Electrical transport measurements on superconducting thin-films: setup and samples

2.2.1 Measurement Systems

The electrical transport measurements contained in this work were performed at MaSTeR-Lab of CNR-SPIN Salerno and Physics Department of Salerno University. The samples were measured using three cryogenic Cryogenic Ltd. Systems:

- Cryogen Free Measurement System equipped with a superconducting magnet of 9 T (CFM9T)
- Cryogen Free Measurement System equipped with a superconducting magnet of 16 T (CFM16T)
- Liquid He Storage Dewar Magnetic Insert equipped with a superconducting magnet of 2 T.

Cryogen-Free Measurement Systems

The Cryogen Free Measurement System (CFM) from Cryogenic Ltd is a modular research system designed to perform a wide range of material characterisation experiments in variable field and variable temperature. The CFM setups for this work are composed by the following main components:

- Cryostat
- Superconducting magnet
- Variable Temperature Insert (VTI)
- DC-Probe Rod
- Static Gas Chamber insert
- Electronics and software for control and measurements.

Cryostat

The cryostat is a thermally insulated vacuum chamber with a pressure about 10^{-6} mbar, equipped with thermal and magnetic screens. Inside, it houses the VTI, the superconducting magnet, and a two stage Pulse-Tube cryocooler which serves the VTI cryogenic line and the magnets. The cryocooler first stage operate typically at about 40 K while the second stage at less than 4 K.

Magnets

The CFM9T magnet is made by NbTi wire winding, while the CFM16T magnet is a composite solenoid with the inner coil made by Nb_3Sn and the outer coil made by NbTi. The reason for this type of choice is in the fact that the maximum upper critical field of NbTi is 14 T, while for Nb_3Sn it is up to 22 T. These values are just estimations at T = 0 K, while at the system operating temperatures varying from 3.5 to 5.5 K these values are lower (see section 1.4 and Fig. 1.21).

The current leads of the magnet are two-stage connections. The first stage, from room temperature down to cryogenic temperatures, consists in copper current leads, while the second stage, at cryogenic temperature, consists of superconducting cables. This is to avoid heat input to the solenoid due to the joule heating of resistive copper wires.

The magnet is powered by a power supply with a current up to 120 A. The magnet can work in persistent mode, by short-circuiting the current leads through a superconducting switch, once the magnet has reached the working field. In this mode, the current circulates entirely in the superconducting circuit continuously with very long decay times, typically of 0.01 ‰ per hour. In normal operation mode, the superconducting switch is kept in the normal state by a heater, which is switched off whenever the persistent mode is needed.

Cernox thermometers are mounted on the solenoid and the switch through which the magnet subsystem can be monitored continuously.

Variable Temperature Insert (VTI)

The VTI is a cylindrical chamber vertically inserted inside the solenoid in which the temperature can vary within 1.6 K and 325 K. The sample space in the magnet bore is 25 mm in CFM9T and 30 mm in CFM16T. The VTI external part is topped with a load lock chamber linked to VTI through a gate valve, which allows the sample to be loaded without exposing the VTI to atmospheric pressure. Indeed, the VTI is previously evacuated up to a pressure of 10^{-6} mbar to eliminate gases that could compromise the achievement of cryogenic temperatures. The description of the cooling operation can be followed by referring to Fig. 2.5. A helium gas line, taken from a dump, is fed inside the cryostat through a self-sealing inlet valve. The first section of the gas line is in thermal contact with the first stage of the cryocooler of 40 K. At this temperature, any oxygen or nitrogen particles have solidified and are captured by the charcoal trap, i.e. an activated carbon filter, to avoid blockades in the lower temperature sections. The second section of the gas line is thermally linked to the cryocooler second stage at 4.2 K. In this section the circulating He gas condenses and it is collected in a helium pot. Vapours from the He bath in the pot are forced to circulate into the VTI chamber by the meaning of an oil-free rotary pump. The vapours flow is regulated by a

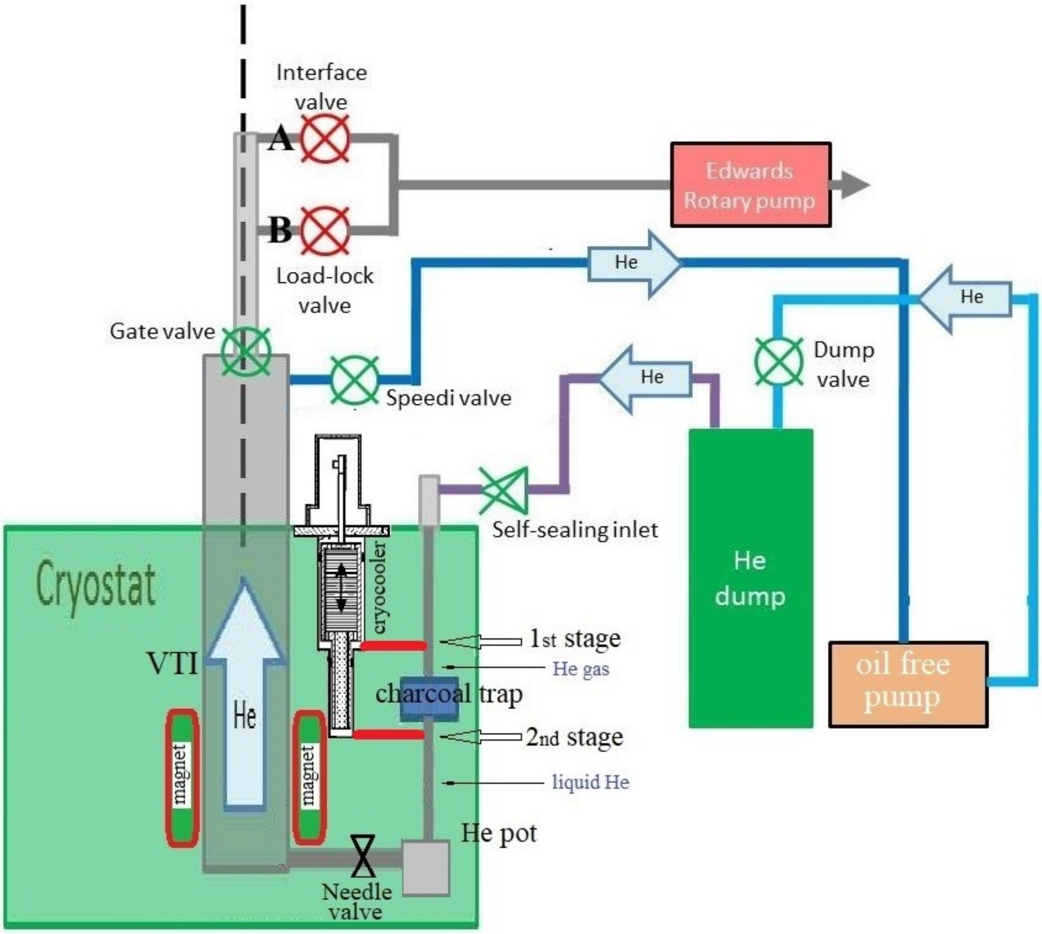

Fig. 2.5: Cooling operation scheme of the cryogen-free systems used in this work (Cryogenic Ltd. Technical manual).

needle valve. The temperature in the VTI is monitored by a high sensitivity temperature cernox sensor placed near to the gas outlet of the needle valve. The outlet on top of the VTI chamber is connected to the He dump inlet through the oil-free rotary pump.

DC-Probe

The Cryogenic Ltd. DC probe is composed by a Probe Stick and a Probe-end that are connected through a plug-in connection. It is designed for electrical transport measurements powered by direct current. The wiring consists of 12 twisted lines for the transport measurements and 6 for the cernox thermometer and the heater placed on the probe end. The sample is usually mounted on a sample holder platform which can be pluged-in two slots on the probe-end, one displaced perpendicularly and the other parallel to the magnetic field axis (Fig. 2.6)

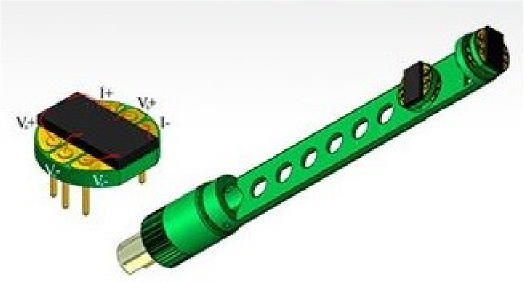

Fig. 2.6: Sketch of the CFM system Probe-end (Cryogenic Ltd. Technical manual).

Static Gas Chamber insert

Measurements can be made through a ***dynamic gas flow system*** or a ***static gas system***, as it has been mentioned in section 2.1. In the former case, it is sufficient to insert the DC probe into the VTI. In the latter case, an auxiliary chamber can be inserted into the VTI, and filled with He gas up to 2 bar.

Electronics and software for control and measurements

- Magnet Power supply: Cryogenic Ltd. SMS120C-H for CFM9T and CFM16T, with maximum current up to 120 A. It also controls the switch heater.
- Temperature Controller: LakeShore 340 for CFM9T; LakeShore 350 with an auxiliary temperature monitor LakeShore 218 for CFM16T.
- Measurement instruments: Keithley 2430, Keithley 6221, Keithley 2182.
- Software for CFM: LabVIEW Cryogenic Ltd edited software for automated control of magnetic field and temperature. LabVIEW homemade software for measurement instruments control. All instruments are connected through RS232 interfaces to the control computer.

Liquid Helium Modular System

The Liquid Helium Modular System (LHe2T) system has been manufactured by Cryogenic Ltd. and consists of a superconducting magnet that generates magnetic fields up to 2 T mounted on a insert for 50 mm diameter dewar. It allows to insert the same DC probe stick of the CFM systems into a liquid helium bath and to carry out the measurements with the same instrumentation. The electronic instrumental part of the experimental set up for measurements in liquid helium bath consists of the following units:

- Magnet Power supply: Cryogenic Ltd. SMS60C-H – with maximum current up to 60 A.
- Temperature Controller: LakeShore 350
- Measurement instruments: Keithley 2430, Keithley 6221, Keithley 2182.
- Software for LHe2T: LabVIEW Cryogenic Ltd edited software for automated control of magnetic field and temperature. LabVIEW homemade software for measurement instruments control. All instruments are connected through RS232 interfaces to the control computer.

2.2.2 Voltage measurement accuracy

One of the major problem in electrical transport measurements is the presence of considerable spurious voltages generated by the current flow through the wiring and through the contacts to the sample. To reduce the impact of these spurious voltages affecting the voltage measurements usually samples are contacted according to the four-probe configuration [167-169]. This configuration can be used to perform electrical transport measurement on either bulk or thin film specimen. In this configuration four contacts, usually collinear, are realized on the sample: two of them are connected to current source and the other two are connected to the voltage measurement instrument (Fig. 2.7 shows a schematization of the equivalent measuring circuit). In this configuration, the voltage measured by voltmeter is given by [163]:

$$V = (I - I_V)R_{Sample} - I_V(2r_{contact} + 2r_{lead}) \qquad (2.1)$$

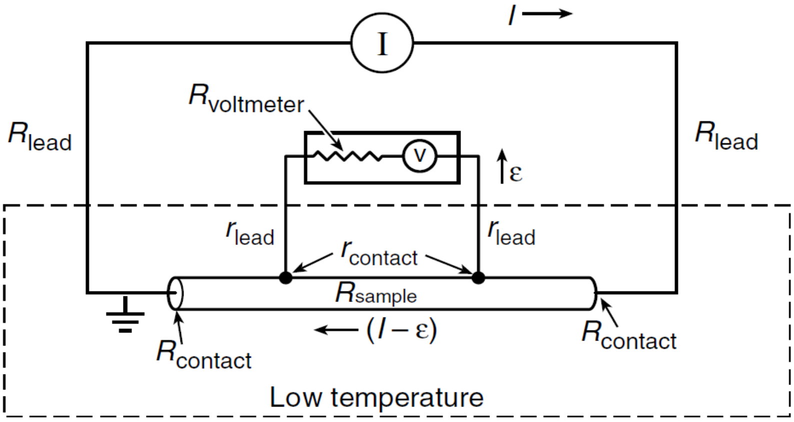

Fig. 2.7: Connection diagram of wire samples for resistance measurements with collinear 4-probe method *[163]*.

Here, I is the transport current supplied by the power supply, I_V is the current through the voltmeter. Since resistance of voltmeter is much larger than the other circuit resistances, I_V is negligible compared to the current I. So, the equation (2.1) become

$$V \cong IR_{sample} \tag{2.2}$$

giving a true reading of voltage drop through the sample voltage taps.

However, there are offset voltages at microvolt and sub-microvolt levels that must be considered in voltage measurements. One of the factors creating additional offset voltages is the thermoelectric effect (or Seebeck effect). Thermoelectric voltages are generated by the junction of two dissimilar metals and/or when different parts of a circuit are at different temperatures. Typically, thermoelectric voltages change from 200 – 500 nV per degree Celsius and can cause significant errors in low voltage measurements [170]. To overcome these unwanted offsets in voltage measurement the current-reversal method is used. It consists in making two measurements with currency of opposite polarity [171]. With the positive current applied as in Fig. 2.8 (a), the measured voltage is $V_{M+} = V_{EFM} + IR$. Reversing the current polarity (Fig 2.8 b) the measured voltage is $V_{M-} = V_{EFM} - IR$. Thus, the two measurements are combined to cancel thermoelectric voltages:

$$V_M = \frac{V_{M+} - V_{M-}}{2} = \frac{(V_{EFM} + IR) - (V_{EFM} - IR)}{2} = IR. \tag{2.3}$$

Finally, the measured resistance is computed in the usual manner: $R = V_M / I$.

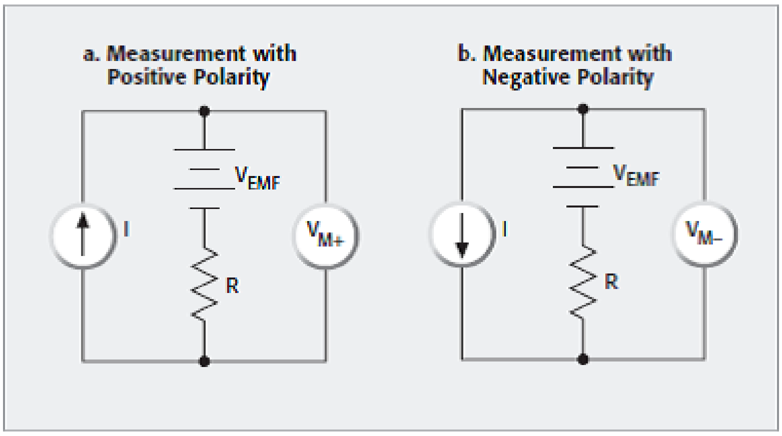

Fig. 2.8: Voltage measurements sketch by making two with currents of opposite polarity, V_{EFM} is the thermoelectric voltage, $V_{M\pm}$ is the measured voltage with its sign [171].

2.2.3 Samples and measurements

Nb-based ultra-thin films

In section 3.1, high quality NbN and NbTiN ultra-thin films have been studied [172-173]. These ultra-thin films were realized in collaboration with CNR-SPIN Salerno and CEA Grenoble (J. C. Villégier Group). The films have been epitaxially grown on a sapphire substrate by DC-magnetron sputtering in the superconducting B1-cubic phase with 5 nm thickness [172]. In order to detect any flux flow instability phenomena by current-voltage (IV) measurements, samples have been patterned by standard UV lithography and several micro-bridges, 1mm long and 50 μm wide, have been obtained (see Fig. 2.9) [69]. In particular, measurement have been focused on NbN sample indicated as NNA_1 and the NbTiN sample indicated as NTNB_1.

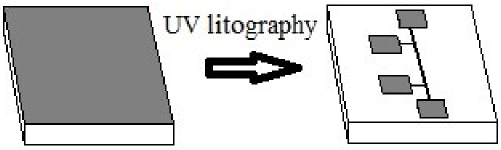

Fig. 2.9: Sketch of NbN and NbTiN ultra-thin film photolithography.

Resistance measurements of the two micro-bridges NNA_1 and NTNB_1 were performed in the CFM9T System in a cryogenic gas flow, in the temperature range from 300 to 1.6 K, with the current bias $I = 100\ \mu A$ supplied by a SourceMeter Keithley 2430. The voltage measurements have been performed by a Nanovoltmeter Keithley 2182. The current-reversal technique has been applied.

Current-voltage characteristics have been acquired at the fixed temperature of 4.2 K and in fields range up to 2 T. Measurements have been carried out in three different cooling environments, namely Liquid-Helium, Dynamic-Helium gas flow and Static-Helium gas flow. For the Liquid-Helium measurements was used a Liquid-Helium cryostat equipped with the LHe2T described in Sec. 2.2.1; we will mark measurement carried out in this system with the label LHe. The second cryogenic system involved is the CFM16T System described in Sec.2.2.1 used for both cryogen-free Dynamic- and Static-Helium gas measurements, marked by the labels Dyn-He and St-He, respectively. The St-He measurements have been taken inserting in the VTI a cylindrical chamber (as described in Sec. 2.1), in which was inserted the probe-rod and then filled with a Helium pressure of 250 mbar. The current bias has been supplied by SourceMeter Keithley 2430 in a pulsed current operation mode, to avoid effects due to Joule self-heating [67, 174-176]. Each current pulse has been supplied in rectangular shape with power-on time (or Pulse Width, PW) set at 2.5 ms and the time separation between each pulse (or Pulse Delay, PD) set at 1 s. The critical current I_c has been estimated at 1 μV. The external magnetic field is always perpendicular to the bias current and applied perpendicularly to the film surface.

Fe(Se,Te) thin films

The samples investigated in Section 3.2, are microbridges obtained from Fe(Se,Te) thin films grown on a CaF_2 (001) oriented substrate by standard UV photolithography and Ar ion-milling etching (Fig. 2.10) [177]. The films have been fabricated by Pulsed Laser Deposition (PLD) starting from a target with the nominal composition $FeSe_{0.5}Te_{0.5}$. These samples belong to an optimized second generation of high quality and purity thin films [18]. All samples are provided by CNR-SPIN Genova in collaboration with Physics Department of Salerno University.

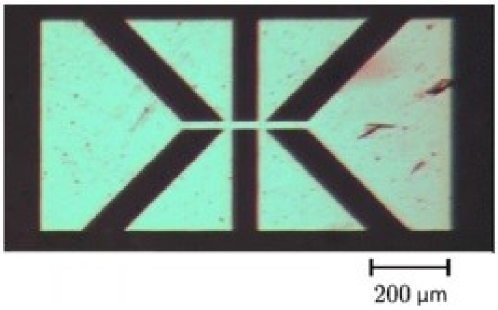

Fig. 2.10: Image of Fe(Se,Te) thin film microbridge [17].

Three types of Fe(Se,Te) samples have been analyzed. W1K is a wide bridge of width W of about 1 mm, length (considered as the distance between voltage tips) L of about 10 mm and thickness S of about 100 nm. The typical $T_c(0)$ for this type of samples is 13.5 K, while the estimated $B_{c2}(0)$ is about 31.1 T. Samples W20 and W10 have a microbridge geometry defined as $W = 20$ µm, $L = 65$ µm and $S = 120$ nm for sample W20 and $W = 10$ µm, $L = 50$ µm and $S = 150$ nm for sample W10. The $T_c(0)$ values are 20.5 K for sample W20 and 18.9 K for sample W10, while $B_{c2}(0)$ are estimated to be respectively 41.8 T and 38.7 T. These data are summarized in Table 2, while more information about sample fabrication and their structural properties can be found elsewhere [16] [178].

Sample	***Width***	***Length***	***Thickness***	***Tc(0)***	***$\mu_0 H_{c2}(0)$***
W1K	1 mm	10 mm	120 nm	13.5 K	31.1 T
W20	20 µm	65 µm	120 nm	20.5 K	41.8 T
W10	10 µm	50 µm	150 nm	18.9 K	38.7 T

Table 2.1

The equipment used for DC transport measurements in order to characterize the above-mentioned samples consists of both the CFM systems, a Keithley SourceMeter model 2430 used as bias current source, and a Keithley Nanovoltmeter model 2182 for voltage measurement. Resistance vs temperature measurements at different magnetic field values have been performed by a standard four-probe technique in the current reversal mode. I-V characterization have been performed by a four-probe technique with a pulsed current operation mode. Each current pulse has been supplied by Keithley SourceMeter model 2430, with rectangular shape. The PW has been set at 2.5 ms and the PD at 1 s in order to allow complete recover of the sample temperature to the heat flow temperature.

2.3 Technical Superconductors Characterization: setup and samples

In this section, experimental methods which involve the technical superconductors BSCCO Round Wires are described. Our work is focused on Superconducting wires manufactured by Oxford Superconducting Technology (OST). The electrical and thermal characterization were carried out in facilities and experimental setups of "Département de Physique de la Matière Quantique" of Geneva University (Switzerland).

2.3.1 Bi-2212 Round Wires - Samples

The technical superconductors investigated are Bi-2212 round wire samples fabricated as multifilamentary conductor by the powder-in-tube (PIT) method [80, 179-180]. Moreover, J_c is enhanced removing porosity in Bi-2212 filaments with densification treatments, obtained through overpressure partial melt processing [22, 143, 147, 181]. In particular, the samples measured in this thesis are three Ag-0.2wt.%Mg (AgMg) reinforced 0.8-mm-diameter Bi-2212 round wires composed by 37 x 18 filaments embedded in a Ag matrix. Samples have been extracted from the same batch manufactured by Oxford Superconducting Technologies (billet number: ppm130723) and reacted by heat treatment at the National High Magnetic Field Laboratory under different total pressures, namely 1 bar, 10 bar and 100 bar, named respectively as Bi-2212_1bar, Bi-2212_10bar and Bi-2212_100bar (Fig. 2.11 [182]).
The heat treatment employed pure O_2 for 1 bar treatment and O_2-Ar mixtures for overpressure treatment, with a maximum temperature T = 890°C [143]. For resistivity, *RRR* and calorimetry measurements, samples must be appropriately prepared as shown in the following paragraphs.

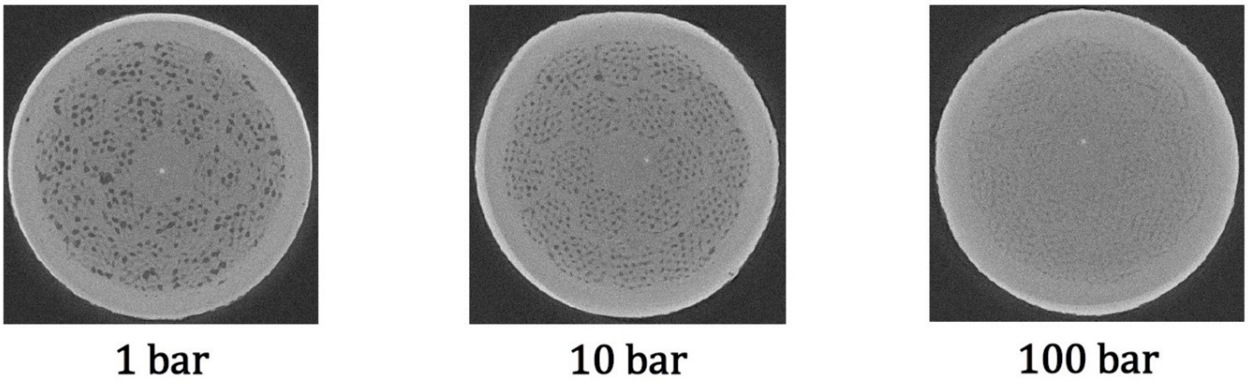

Fig. 2.11: Void reduction observed by high-energy X-ray micro tomography [182].

2.3.2 Resistivity Measurements

Cryocooler

The experimental system for resistivity measurements, in a temperature range of 10 K to 320 K, consists in a cryocooler Janis series closed cycle refrigerator system based on the G-M thermodynamic cycle [183-184]. On the cold head (see Fig. 2.3), a heater and a Cernox thermocouple used to control the sample temperature are installed.

The experimental system is equipped with a power supply Keithley 224 as current source. In Bi-2212 round wires *R(T)* measurements, the 224 has been set to supply 100 mA due to high noise levels for lower current values. Voltage measurements in R(T) are performed by a nanovoltmeter Agilent 34420A. A temperature controller LakeShore 332 is used to supply current to the cold head thermocouple.

The electronic units and the computer are connected via GPBI parallel interface with IEEE 488.1 communication protocol. Synchronization of input and output start-up of various units is ensured through external triggers. LabView homemade software provides the measurement instruments control.

Resistivity measurement - Samples preparation

Resistivity measurement of the Bi-2212 round wire was performed with the four-probe technique. High thermal conductivity adhesive resin G-Varnish made possible thermal coupling with the sample holder and then with the cold finger using it to paste the sample to the sample holder (Fig. 2.12 a) and the sample holder to the cold finger plate, moreover, applying a thermally conductive gel (Fig. 2.12 b) to the sample holder that also incorporated the sample.

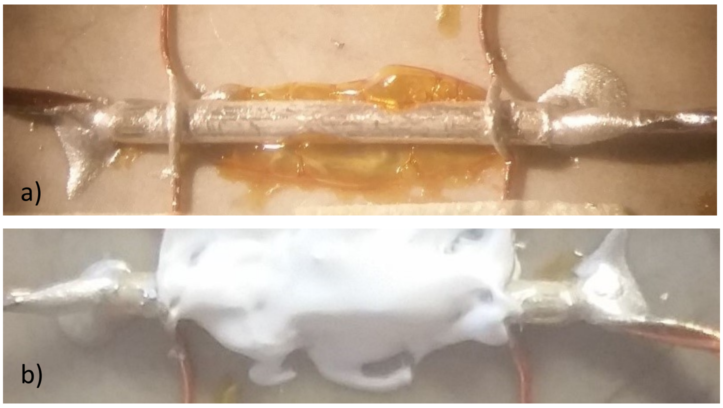

Fig. 2.12: Bi-2212 sample coupling with the sample holder by means of G-Varnish (a), and thermal conductive gel (b)

The copper leads were linked through gluing with silver paint. Moreover, the distance between the voltage contacts is acquired with a digital caliper because it is necessary to calculate resistivity by resistance measurements.

RRR measurement – Sample preparation

In order to determine the Ag Matrix *RRR*, the superconducting filaments were removed dissolving the Bi-2212 in glacial acetic acid. The matrix has not been degraded since it is inert to the used acid. The chemical etching was carried out on a Bi-2212_100bar sample, of about 2 mm of length, cut by a diamond wire saw from the original sample. The duration of the process was about 8 days at room temperature. For longer samples, even with a longer chemical etching, not all filaments can dissolve.

Due to the small wire size and very low resistivity of the Ag-matrix, the resistance of the sample at low temperatures is too low to be measured in the cryocooler system. In fact, the noise due to the mechanical vibrations of the cryocooler is greater than the low temperatures characteristic resistance of the sample. For this reason, the *RRR* was determined by a 4-wire *R* measurement performed at zero field using a low-noise probe for electrical transport [185]. A Keithley 2400 source-meter, which allows measuring the actual current in the circuit, was used as a current source. An excitation current of 0.1 A was chosen in order to avoid heating effects. The voltage drop across the sample has been amplified by a factor 10000 by means of an EM-Electronics nanovolt amplifier (no filter used) and measured with a Keithley 2182A nanovolt-meter in current reversal mode [182].

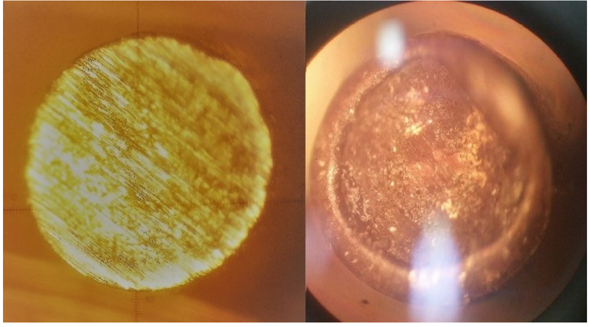

Fig. 2.13: Image of Bi-2212 wire before and after chemical etching treatment.

2.3.3 Calorimetry measurements

Physical Property Measurement System

Fig. 2.14: PPMS cryostat and instrumentations [186] .

Heat capacity measurements have been performed in a Physical Property Measurement System (PPMS) produced by Quantum Design (Fig. 2.14). The PPMS consists in a cryostat where the sample is hosted in a vacuum chamber immersed in a liquid helium bath. Around the sample chamber, there is a superconducting magnet that can generate a field of up to 7 T. The sample chamber is vacuumed with a low vacuum rotary pump and high vacuum absorbing pump.

PPMS is equipped with a Heat Capacity option consisting of a specially designed calorimeter puck. The calorimeter puck is a circular frame in which a calorimeter chip, which functions as a sample platform, is located. The sample platform is suspended in the puck centre and supported by eight thermally conducting wires that form the electrical connections to a heater and a thermometer attached to its bottom. Below the frame there is a chuck through which the puck is fixed to the bottom of the sample chamber and guarantees the electrical connections and the thermal coupling. On the top of the puck a thermal radiation shield is placed. This shield prevents the wires and platform from being damaged and protects them from unwanted heating that is created by warmer surfaces in the sample chamber (cf. Fig 2.15).

System management takes place via the PPMS Model 6500 controller that houses the Heat Capacity DSP card. The DSP card contains the electronics needed to simultaneously control the heat applied by the heater and the temperature measurement by the thermometer. When the system performs a heat capacity measurement, the DSP card sets the heater platform current applied by a precision current source. The current ranges allowed by the electronics is between few nanoamps to a few milliamps, and the heater power is determined as a time function with high precision. In the

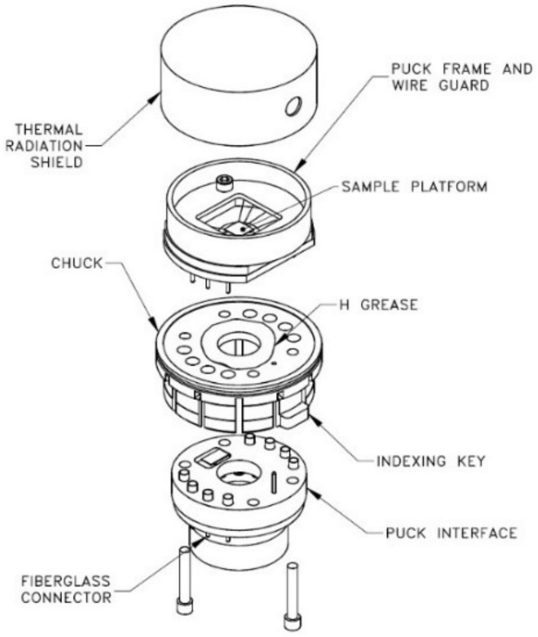

Fig. 2.15: sketch of PPMS Calorimeter puck [186]

same time, a precision current source provides a square-wave AC excitation current at 244 Hz for reading the platform thermometer, while a high precision ADC reads the voltage across the thermometer in both positive and negative parts of the square-wave. The differences between the two measurements provides the value of the resistance at about 4 ms intervals and thus one obtains the corresponding temperature through the thermometer calibration.

The sample connection to the thermal bath takes place through the sample-platform connection wires to the puck frame. This connection is well-controlled. To eliminate the non-controllable thermal connections through the gases surrounding the sample, the sample chamber must be emptied. The sample chamber pressure must be about 1 mTorr. Thus, in addition to a membrane pump, a cryopump, that uses a charcoal sorption pump maintained at liquid-helium temperatures as active pumping element, drops the pressure to about 0.01 mTorr.

An integral part of the Cryopump High-Vacuum system is the contact-baffle assembly that helps to create a more uniform thermal environment for the disc. Indeed, when high vacuum is enabled, the heat exchange gas in the sample chamber are reduced so the contact baffle is the only way to uniform the temperature throughout the sample chamber. The contact baffle includes a charcoal holder into its bottom that prevents helium from adsorbing on the sample platform at temperatures below 10 K.

Heat Capacity measurements

In the PPMS is measured the thermal capacity at constant pressure

$$C_p = \left(\frac{dQ}{dT}\right)_p \tag{2.4}$$

The measurement is obtained yielding to sample a known amount of heat, and then measuring the corresponding change in temperature. The heating cycle is followed by a cooling cycle of the same duration [186].

To measure the heat capacity of a material it must be considered that in adiabatic conditions, if a power *P(t)* is supplied to a sample whose thermal capacity is $C_S(T)$, starting from eq. (2.4), the sample heating is described by

$$\frac{dQ}{dt} = C_S(T)\frac{dT}{dt} = P(T(t)) \tag{2.5}$$

The temperature *T* of the sample at time t is given by the integral of (2.5):

$$Q = \int_{T_0}^{T} C_S(T)dT = \int_{t_0}^{t} P(T(t))dt \tag{2.6}$$

where T_0 is the initial temperature (at $t = t_0$) and Q is the total heat given to the sample at time t (cf. [187]). If we are in non-adiabatic situation in which there are thermal connections, experimental problems can rise because the connections can have a dominant influence especially for small samples at very low temperatures. Therefore, various measurement techniques have been developed to optimize situations with different sample sizes and accuracy requirements. The Heat Capacity option uses a relaxation technique that combines good accuracy with good analysis techniques [188]. In a non-adiabatic regime, where we also consider a thermal conductivity K between the sample holder and the thermal bath, equation (2.5) becomes the so called *Simple model* equation:

$$C_{total}(T)\frac{dT}{dt} = P\big(T(t)\big) - K_w[T - T_B] \tag{2.7}$$

Where C_{total} is the heat capacity of the sample and the sample platform, K_w is the thermal conductance of the supporting wires, T_B is the temperature of the thermal bath and $P(t)$ is the power applied by the heater. During the heating cycle $P(t) = P_0$ while during the cooling cycle the power is zero.

If there is a poor thermal attachment between the sample and the platform, we can find a temperature difference between them. To take into account the flow of the heat between the sample, the platform and the puck, it has been developed the so called *Two-tau model*[1], expressed by the following equations:

$$C_p(T)\frac{dT_p}{dt} = P\big(T(t)\big) - K\big[T_p - T_B\big] + K_g\big[T_s(t) - T_p(t)\big] \tag{2.8}$$

$$C_s(T)\frac{dT_s}{dt} = -K\big[T_s(t) - T_p(t)\big] \tag{2.9}$$

where C_p and C_s are the heat capacity of platform and sample, respectively, K_g is the thermal conductance between the platform and sample due to the grease, T_p and T_s are the platform and sample temperatures, respectively [186].

The solutions for the Simple model and the Two Tau model equations is the function

$$T(t) - T_B = A_1 e^{-\frac{t}{\tau_1}} + A_2 e^{-\frac{t}{\tau_2}} \tag{2.10}$$

Here, the Simple Model parameters are $\tau_1 = C_{total}/K$ and $\tau_2 = 0$, while the Two Tau Model parameters are $\tau_1 = 1/(\alpha + \beta)$ and $\tau_1 = 1/(\alpha + \beta)$, with

$$\alpha = \frac{K}{2C_p} + \frac{K_g}{2C_p} + \frac{K_g}{2C_s}$$

---

[1] Two-tau model is a trademark of Quantum Design

$$\beta = \frac{\sqrt{K_g^2 C_s^2 + 2K_g^2 C_s C_p + K_g^2 C_p^2 + K^2 C_p^2 + 2K C_s^2 K_g - K C_s K_g C_p}}{2 C_p C_s}$$

The heat capacity measurement is divided into two steps. The first step is dedicated to measuring the heat capacity of the *addenda*, i. e. of the platform, the grease, etc., without the sample housed in it. The second step consists in measuring the *total* heat capacity, i. e. of the platform, the grease, the sample, etc. The sample heat capacity is then obtained by the difference:

$$C_S = C_{total} - C_{addenda}$$

Heat capacity is determined using a non-linear, least-square fit to compare the solution to the simple model to the actual measurement. The values of the parameter that give the smallest fit deviation determine the heat capacity. The standard errors for the heat capacity is estimated using the sensitivity of the fit deviation to small variation in the fitting parameters (Chi-square method).

Except when measuring the addenda, a fit to the solution of the two-tau model is also performed. The heat capacity numbers derived in this way are used only if the fit has a smaller fit deviation than in the first case. Under some circumstances, the fit to the two-tau model does not converge, in which case the simple fit is again used. Such a lack of convergence can occur when the sample is perfectly attached to the platform, in which case the simple model is correct [186].

Heat Capacity measurement - Samples preparation

For the Heat Capacity measurement with the PPMS, the size of the samples must be a compromise between opposing needs. The need to have no prohibitive times requires small sample sizes. On the other hand, having a too small sample would mean having a much lower thermal capacity than the addenda thermal capacity, and this is at the expense of accuracy. Therefore, the sample should have a weight between 1 and 200 mg. To this end, the three samples we measured were obtained by cutting about 1.5 mm of length and 8 mg of weight from the original samples through a diamond wire saw. Each sample is then placed on the sample holder of the Calorimeter Puck (Fig 2.16).

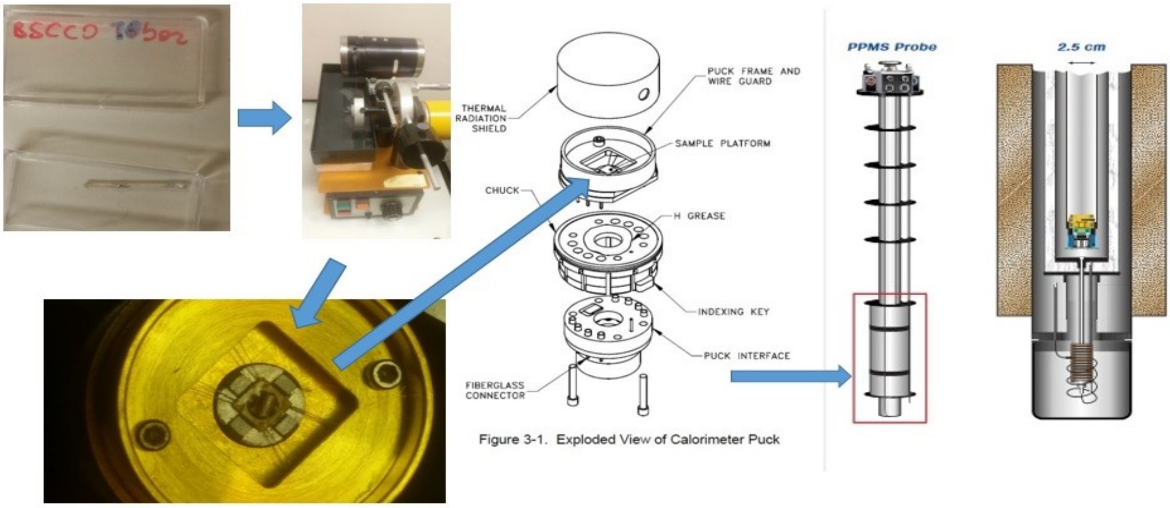

Fig. 2.16: Bi-2212 sample preparation and housing in the Calorimeter puck [186].

2.3.4 Thermal transport measurements

Superconducting 21 T Measurement System

Thermal Conductivity has been measured using a set up specifically designed for high-field measurements in technical superconductors [153-155]. The experimental set up is based on a Bruker Bio-Spin Cryostat MC21T/64A SD321, equipped with a 21 T superconducting magnet. It contains a liquid Helium vessel isolated by a liquid nitrogen vessel and a vacuum vessel. Along the central axis is placed a variable temperature insert VTI in which the probe is inserted for cryogenic and magnetic field measurements. To further lower the 4.2 K liquid helium temperature, it is possible to pump the VTI through a turbo pump, thus reaching temperatures of about 1.6 K. The superconducting magnet is a composite solenoid with the inner coil made by Nb_3Sn and the outer coil made by NbTi (see also section 2.2.1), supplied by a Bruker Power supply controlled through Bruker B-MC20 model. The technical characteristics of the cryostat, the magnet and the power supply are summarized in the table 2.2.

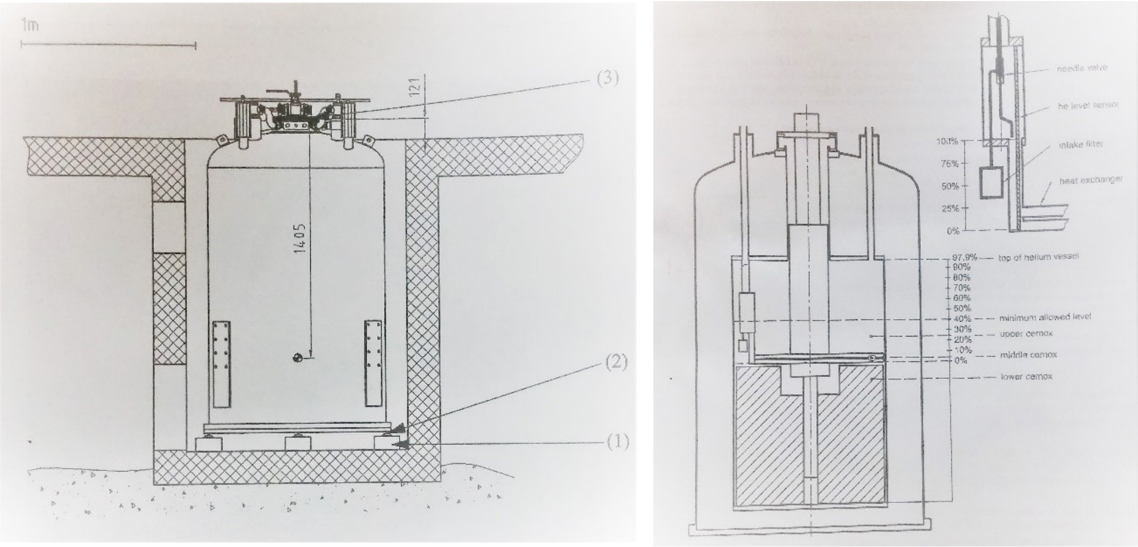

Fig. 2.17: Sketch of Superconducting 21 T cryostat (Bruker technical manual)

Measurements within 10 K are carried out in liquid helium bath while those beyond 10 K are performed in gas flow mode. In both cases, to obtain measurements for higher temperature values, the sample is heated through a heater. The VTI temperature is controlled by a LakeShore 340.

Cryostat components / features	**Quantities/Types**	**Operative conditions**
Helium total volume	200 litres	
Nitrogen total volume	229 litres	
Maximum central field	19 Tesla	at 4.2 K
	21 Tesla	at 2.35 K
Maximum current	271.72 Ampere	at 21 T
Coil inductance	78.5 Henry	
Magnetic energy	2.9 MJoule	at 21 T
Cryostat minimum diameter bore	64.1 mm	
VTI Sample space	52 mm	
VTI Temperature range	1.6 – 100 K	
Maximum current	300 A	
Maximum voltage	20 V	
Magnet Manufacturing materials	Nb_3Sn/NbTi	

Table 2.2

Thermal Conductivity Probe

In order not to affect thermal conductivity measurements with errors caused by undesired thermal dispersion, considerable attention has been paid to minimizing heat transfers that do not occur through the sample. Indeed, the heat flowing from the heater to the heat sink can be transferred through parallel channels rather than through the sample. The heat flows through three types of parallel channels, the heat transmitted through the gas surrounding the sample that is the dominant effect, the heat transmitted through the connection wires and the one transmitted by irradiation. In the latter case, for a small object heated to a temperature $T + \Delta T$ in an isothermal chamber at temperature T, the radiate heat W_1 is given by Stefan-Boltzmann law

$$W_1 = \sigma A \varepsilon (T + \Delta T)^4 \qquad (2.11)$$

where $\sigma = 5.6704 \cdot 10^{-8}$ W/m^{2}K^4 is Stefan-Boltzmann constant, A is the heater surface and ε is the emissivity. However, even the walls of the sample chamber radiate toward the sample and the amount of heat absorbed by the object is

$$W_2 = \sigma A \varepsilon T^4 \qquad (2.12)$$

So, the net heat emission by the heater is

$$W_{net} = W_1 - W_2 = 4\sigma A \varepsilon T^3 \Delta T + O(\Delta T^2) \qquad (2.13)$$

To minimize the heat transfer through the aforementioned three channels, the following solutions have been adopted [154]:

1. The heat loss through the gas is countered inserting the probe-end into a cylindrical vacuum chamber and evacuating the space around the sample to pressure below 10^{-5} mbar.
2. The wiring of the heater and of the thermometers is made with wires of 0.06 mm diameter, so that wiring conductance is at least 100 times lower than sample conductance. Moreover, the contact between the hot-terminal, where the heater is placed, and the rest of probe is limited to two 0.1 mm diameter nylon wires.
1. The contribution due to irradiation is minimized using materials with very low emissivity ($\varepsilon \approx 0.018$).

It results that even for samples whose thermal conductivity is 1 Wm^{-1}K^{-1}, the residual heat fraction generated by the heater reaching the thermal bath through parallel channels is less than 0.05%.

Probe Hardware

The thermal conductivity probe is equipped with a cylindrical vacuum chamber that encloses the sample holder and is evacuated through a pumping port located at the probe head by a turbo-molecular pump running continuously during the measurement. The ‘cold terminal’ of the sample holder is a heat sink which houses a heater and a calibrated thermometer, through which the operating temperature of the sample holder is controlled. Typically, the sample has the shape of a bar about 1-2 cm long and a circular or rectangular cross-section of about few mm^2 of area. An end of the sample is attached to the heat sink in a suitable mounting housing and it is possible to place it with its axis both perpendicular (Fig. 2.18) and parallel to the magnetic field. The other end of the sample is attached to a housing that constitutes the ‘hot terminal’ on which is placed the heater used to create the temperature gradient. Two bare-chips are glued to the sample with a varnish resin which ensures a non-permanent attachment, is an excellent thermal conductor and is easy to apply and remove. The choice of bare-chips is due to the extremely small size and therefore the lesser effect they have on the heat radiation, as well as the accuracy and the speed of response, as well as their low typical magnetic field-dependent temperature errors $\Delta T/T$ (%). Bare-chip characteristic are summarized in Table 2.3 [189]. The bare chips are calibrated each time through a

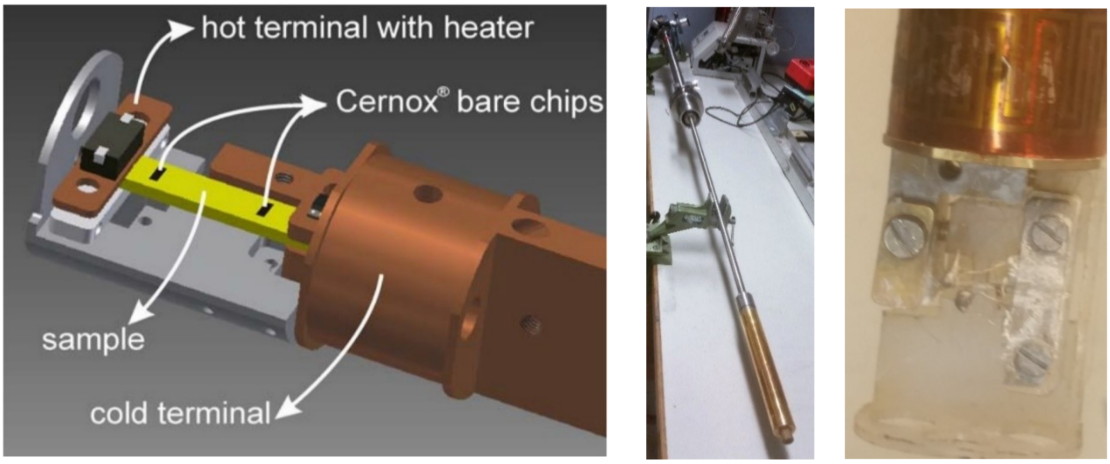

Fig. 2.18: On the left: view of thermal conductivity probe terminal with sample parallel to magnetic field [154]. In the middle: Full thermal conductivity probe with cylindrical vacuum chamber enclosing the terminal probe. On the right: the sample housed perrpendicularly to the magnetic field.

Operative Temperature	**4.2 K**	**77 K**	**273 K**
Thermal response times	1.5 ms	50 ms	135 ms
Calibrated Accuracy	±5 mK	±15 mK	±40 mK
Temperature errors $\Delta T/T$ *(%) at* $B = 2.5$ *T*	0.1	0.002	0.003
Temperature errors $\Delta T/T$ *(%) at* $B = 8$ *T*	-0.15	0.022	0.004
Temperature errors $\Delta T/T$ *(%) at* $B = 14$ *T*	-0.85	0.062	0.004
Temperature errors $\Delta T/T$ *(%) at* $B = 19$ *T*	-0.8	0.11	0.006

Table 2.3

process that will be described in the last part of this section. The distance L between the two bare-chips is measured by a caliper.

Electronics and software for control and measurements

In the Fig. 2.19 is shown the wiring of the probe terminal. We can see three wires groups, the upper one collects the sample thermometry wiring, the middle group collects the cold terminal temperature controller wiring, the lower one collects the hot terminal heater wiring.

Pins	**Instrument**	**Function**
K 1 – K 2	Source Meter Keithley 2400	Bare Chips current supply
A 1 – A 2	Digital Multimeter HP 3458A	Bare chip 2 - Voltmeter
A 3 – A 4	Digital Multimeter Agilent 3458A 8½	Bare chip 1 - Voltmeter
LS series	Lake Shore 340	Temperature Controller
K 3 – K 4	Source Meter Keithley 2400	Heater B current supply
A 5 – A 6	Digital Multimeter Agilent 3458A 8½	Heater B Voltmeter

Table 2.4

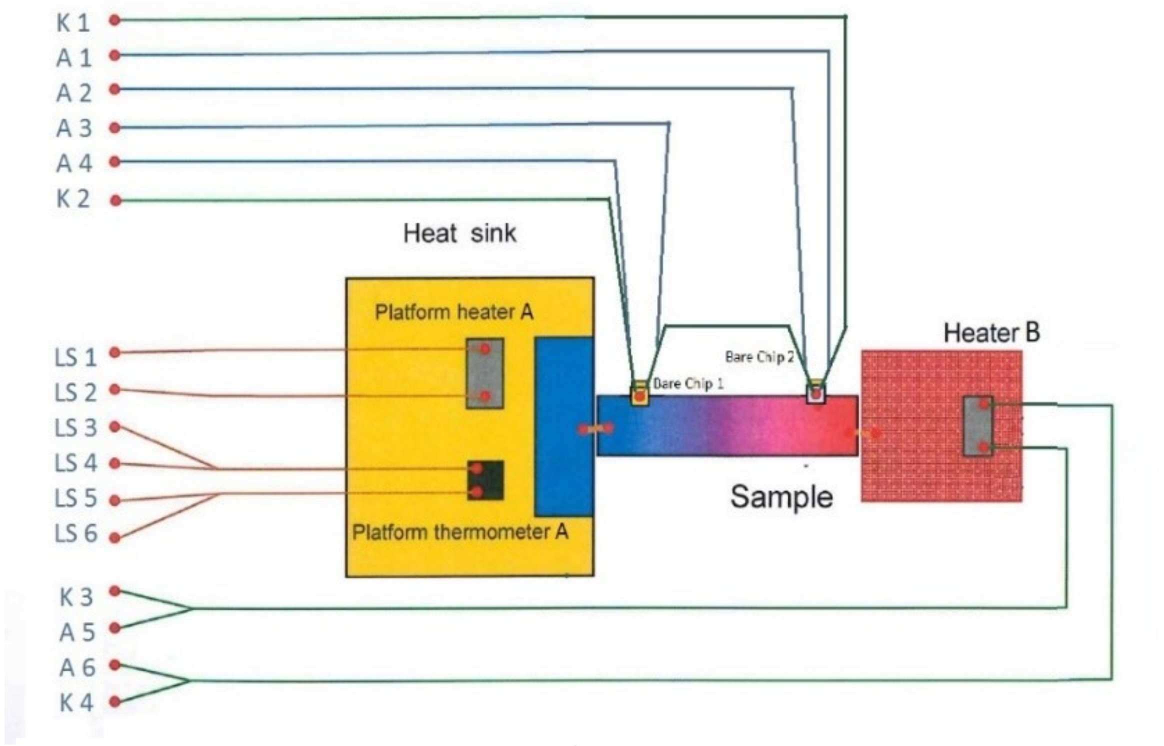

Fig. 2.19: sketch of probe-end wiring

The measurement instrumentations used for thermal conductivity measurement, connected via connectors and a breakout box, are summarized in Table 2.4.

A Keithley 2400 source-meter, supplies to the bare chips an excitation current of 1 µA.

The voltage drop across each bare chip is measured with two different digital multimeters Agilent 3458A type. The heating power provided to Heater B is obtained suppling it with a current within 0.6 mA to 2.0 mA, depending on the operative temperature. Therefore, the required heating power is obtained by multiplying this value for the heater's resistance.

The heat sink temperature is measured by a LakeShore 340.

The control software is homemade designed in the LabVIEW environment and allows to automatically control all the measurement procedure. All instruments are connected through GPBI 488 bus to the control computer.

Measurements procedure

Thermal conductivity is measured by means of the steady-state axial heat flow method, considering the thermal diffusion equation (Fourier- Biot law)

$$W = KA\frac{\Delta T}{L} \tag{2.14}$$

that links the thermal conductivity K to the measured quantities ΔT, with given the thermal power W, the cross-section area of the conductor A and its length L. The ΔT temperature difference is measured when a steady temperature gradient has been reached, assuming a homogeneous material sample and the flow of heat through the cross-section so that the one-dimensional approximation is valid (see Fig. 2.20).

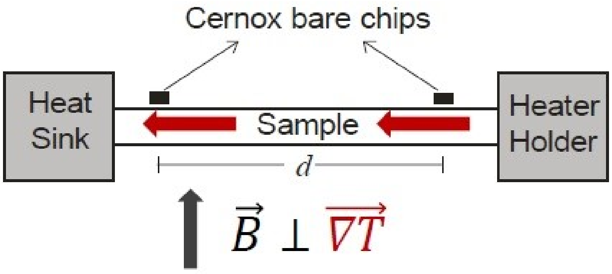

Fig. 2.20: sketch of thermal flow through the sample

The procedure used to determine the thermal conductivity as the temperature changes is the following:

- The operating temperature T′ is set on the LakeShore temperature controller of VTI. When the two bare chips thermalization is reached, their resistance values are acquired. Therefore, the two resistances for chip 1 and chip 2, corresponding to the same temperature, are respectively called $R_1(T')$ and $R_2(T')$.
- A current bias to heater B is applied. At this stage, when the two bare chips thermalization is reached, because the sample is between two heat sources, the steady state is characterized by a temperature gradient along it. For this reason, the bare chips temperature respectively reaches the

different values, T_1 and T_2. Thus, the previous acquisition operation is repeated by obtaining the resistances $R_1(T_1)$ and $R_2(T_2)$.

- The current bias to heater B is removed and the operating temperature is increased at T″ value. Thus, the acquisition operation is repeated for the third time by getting $R_1(T'')$ e $R_2(T'')$.

If the temperature range (T′, T″) is small (up to 1 K), it is possible to approximate the R(T) curve as a line. Therefore, identifying the $R_1(T_1)$ value on the line that joins the points $R_1(T')$ and $R_1(T'')$, and the $R_2(T_2)$ value on line that joins $R_2(T')$ and $R_2(T'')$, it is possible to establish the temperature values T_1 and T_2 respectively (see Fig. 2.21).

We thus obtain the temperature gradient $\Delta T = T_2 - T_1$ due to the power application to one of the wire end and use it to calculate the thermal conductivity K(T). The temperature vale T is given by the mean value between T_1 and T_2.

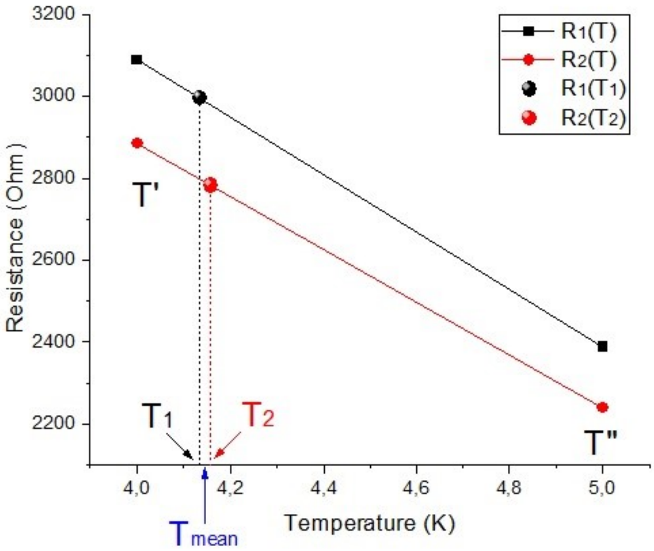

Fig. 2.21: R(T) as a temperature function of bare chip 1 (black), and bare chip 2 (red). T′ and T′′ are the temperature values of both chips acquired without the heater power, while T_1 and T_2 are the temperatures of chip 1 and chip 2 respectively, acquired with heater power on.

3 ELECTRIC CURRENT TRANSPORT STABILITY MEASUREMENTS

3.1 Cooling efficiency study through I-V Curves measurements

Practical applications often involve the use of a superconductor with current values close to critical current I_c. Cooling efficiency and thermal stability can be crucial to avoid quench phenomenon, i. e. the switch from the superconducting state to the normal one.

Therefore, to study how different cooling methods can affect high current measurements of superconducting materials we will consider flux-flow instability phenomenon of ultra-thin films of NbN and NbTiN described in section 2.2.3 [70-190]. In particular, instability parameters I^* and V^*, corresponding to the current and voltage at which the superconducting-normal switch occurs, are studied.

Results and discussion

The high quality of ultra-thin films is displayed in *R(T)* curves. Indeed, the critical temperatures T_c, measured at 50% normal state (onset) resistance R_N, are about 13.7 K and 8.9 K, for NNA_1 and NTNB_1 respectively (Fig. 3.1).

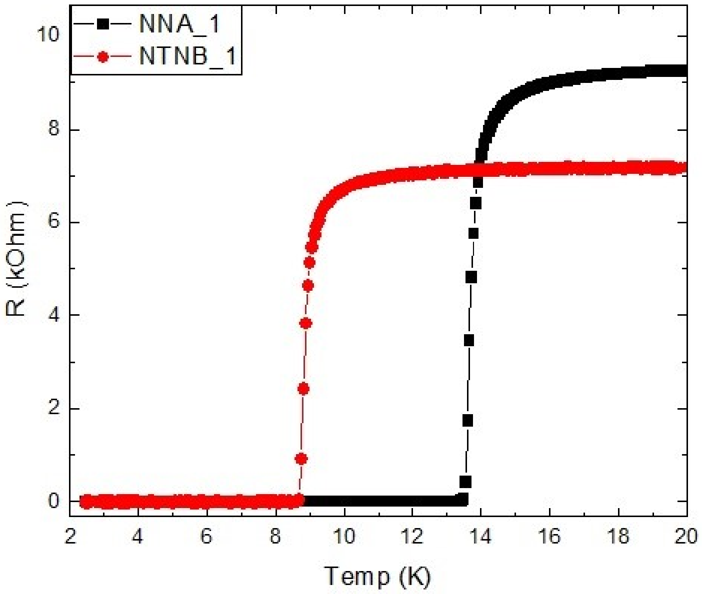

Fig. 3.1: R(T) curves of NNA_1 (black) and NTNB_1 (red) at B =0 T.

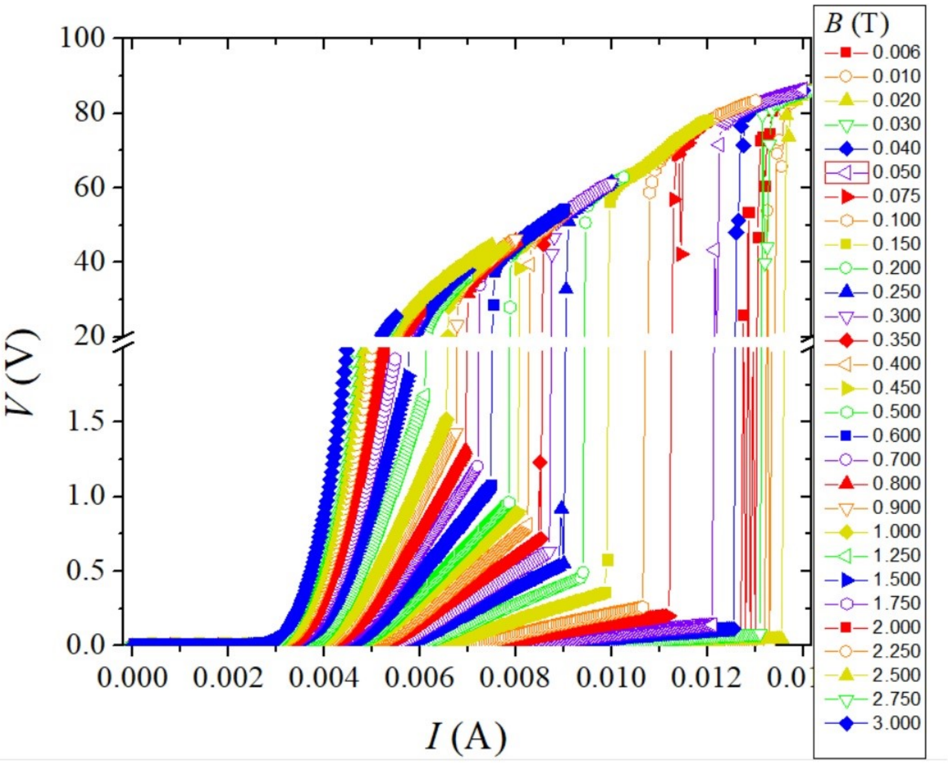

Fig. 3.2: I-V curves in perpendicular magnetic field up to 3 T in cryogen free gas flow environment.

The I-V curves have been acquired at the fixed temperature of 4.2 K, in magnetic fields varying between -2 and 2 T, perpendicularly to the films, for micro-bridges NNA_1 and for NTNB_1. As we can see from Fig. 3.2, which shows the I-V curves in Dyn-He for the NNA_1 in positive fields up to 3 T, the sudden

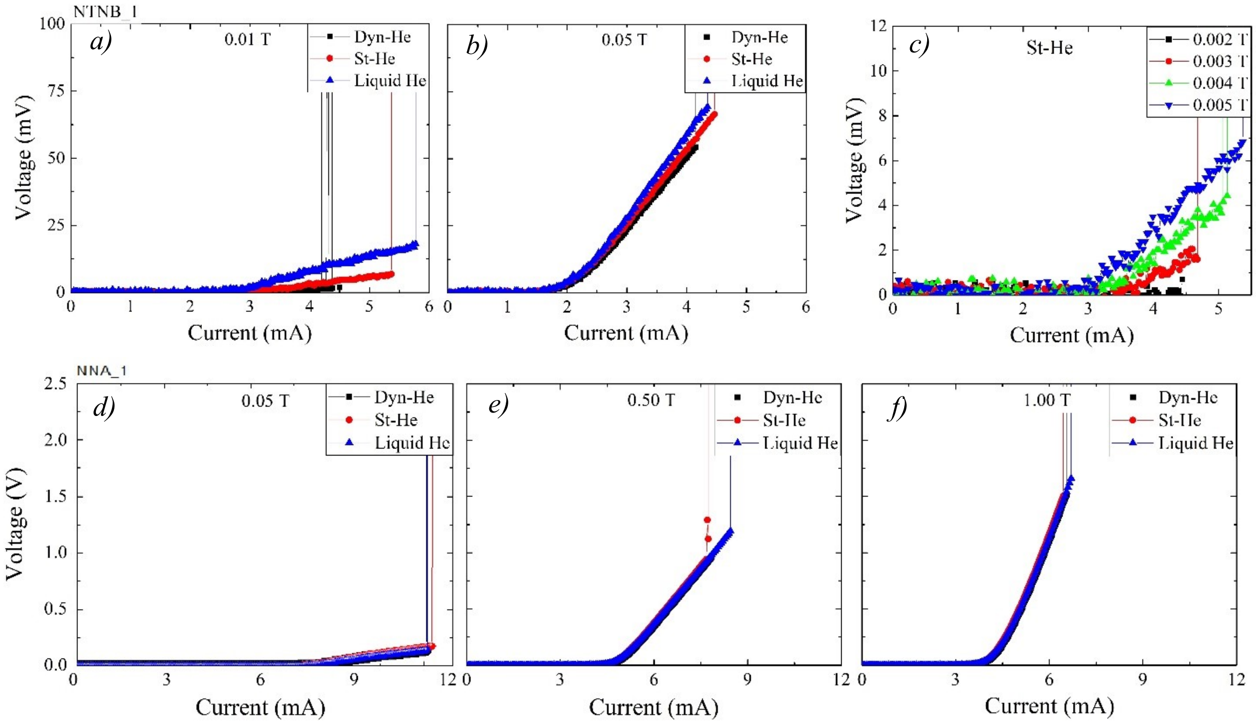

Fig. 3.3: panel a and b) I-V characteristics of sample NTNB_1 and (panel d, e and f) of sample NNA_1 at 4.2 K for each of the three different cooling environments at different magnetic fields. (panel c) I-V curves at 4.2 K for different fields in the St-He environment.

jumps from the flux flow branch to the normal resistive branch, that are the Flux Flow Instability signature, are visible.

A selection of the current-voltage characteristics at different magnetic fields for each of the three different cooling environments at 4.2 K is reported in Fig. 3.3. The small difference in the flux flow resistance that we notice in the I-V curves acquired below 0.05 T is due to small differences in the applied field values. Indeed, in Fig. 3.3 (c) we can notice that a variation of only 1 mT in the applied magnetic field leads to a detectable variation in the flux flow branch. Anyway, we remark that the I-V curves have almost the same I_c and that a variation of 1 mT in the applied magnetic field corresponds to a variation of less than 5% in the I^* values.

In general, we observe that for both samples the I^* values related to liquid He are slightly higher than those related to Dyn-He and St-He environments. This behavior is showed in Fig. 3.4, where the $I_c(H)$ curves of sample NNA_1, defined by a standard 1 μV/cm criterion, for the three cooling environments are reported in panel (a) as well as the corresponding $I^*(H)$ curves in panel (b). In particular, we notice that the three $I^*(H)$ curves perfectly overlap at fields higher than 1 T. The $I^*(H)$ curves show smaller differences for NTNB_1 samples among the three different cooling methods (see Fig. 3.4 (c)).

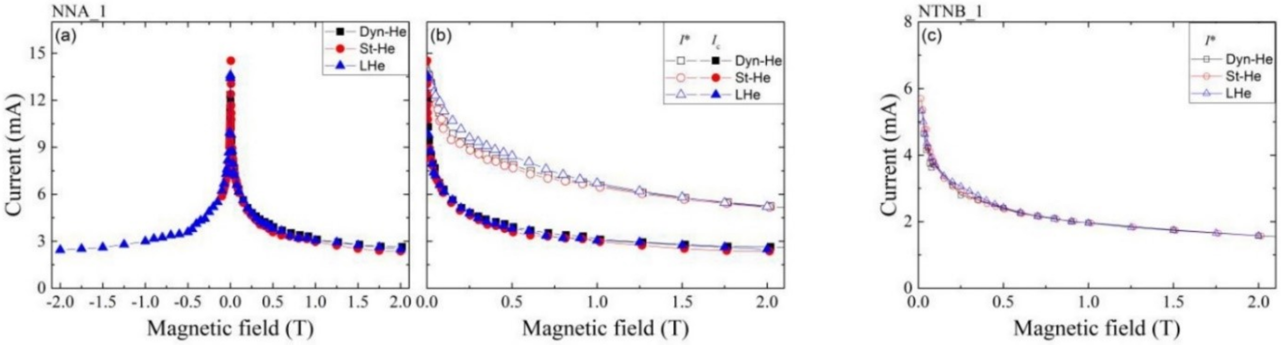

Fig. 3.4: (panel a) Critical current curve as a function of the applied magnetic field of sample NNA_1 for each of the three cooling environments. (panel b) For the same sample, comparison between critical current and instability current behaviors as a function of the applied magnetic field for each of the three cooling environments. (panel c) Instability current curve as a function of the applied magnetic field of sample NTNB_1 in the different cooling environments. All data have been evaluated from I-V curves acquired at 4.2 K

In Fig. 3.5 the critical voltage and the dissipated power $P^* = I^* \cdot V^*$ as a function of the applied magnetic field related to sample NNA_1 are shown, still for each of the three cooling environments. We notice that V^* values are slightly higher in the LHe environment for fields below 2 T, similarly to what has been observed for the instability parameter I^*. Consequently, also the dissipated power P^* related to measurements acquired in liquid Helium have slightly higher values with respect to the other cooling methods for fields below 2 T [174-176].

However, the magnetic field dependence of P*, below 2 T, can be interpreted as intrinsic microscopic mechanisms on the vortex motion instability [174-176, 191]. This can be sufficient to exclude extrinsic self-heating effects and, consequently, the different cooling methods do not influence the instability phenomenon.

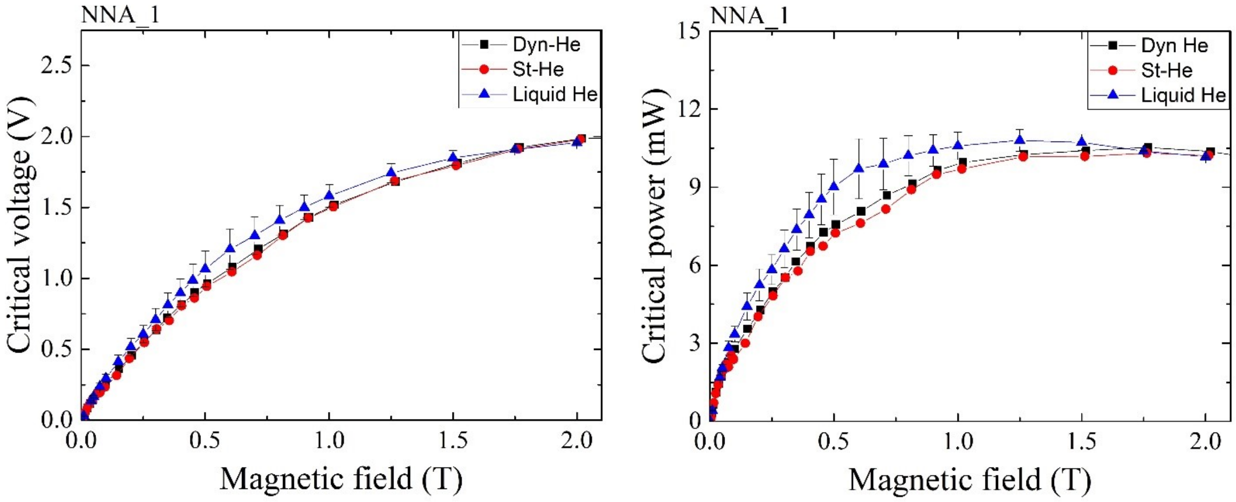

Fig. 3.5: (panel a) Critical voltage and (panel b) critical power behavior as a function of the applied magnetic field for sample NNA_1 in the three cooling environments.

3.2 Electrical transport measurement in Iron-chalcogenides Superconductors

Among the families of iron-based superconductors, the 11-family is one of the most attractive for high field applications at low temperatures. Optimization of the fabrication processes for bulk, crystalline and/or thin film samples is the first step in producing wires and/or tapes for practical high-power conductors. Although several studies have been performed to elucidate the nature of superconductivity in Fe-chalcogenides [92,127], the applications need further investigation.

The samples involved in this work are three optimized $Fe(Se_{1-x}Te_x)$ microbridges described in Sec. 2.2.3. In Section 3.2.1, the results of magnetoresistance analysis are presented. Thus, the determination of H-T phase diagram is showed and compared with literature. Then, the pinning properties have been studied by resistance as a function of the temperature measurements and carried up at fixed values of magnetic field up to 9 T. Moreover, in section 3.2.1, Flux flow instabilities have been recognized in this type of materials and the contributions to the FFI from extrinsic thermal mechanisms, as well as from intrinsic electronic mechanisms, have been investigated. Finally, it has been studied the relation between the critical current and the instability current in Fe(Se,Te) microbridges, with the analysis focus on the difference between I_c and I^*, namely I^*-I_c , which can be seen as a safety range before the full quench into the normal state. Indeed, in the range between I_c and the instability current I^*, the material is still in a superconducting phase, but dissipation occurs due to moving vortices. The relation between these two critical current values is a high relevant topic for the potential high field applications of these superconducting materials, but less well studied in the community, with few works on HTSs to our knowledge [19-20].

3.2.1 Magnetoresistance Analysis

The resistance of Fe(Se,Te) microbridge W20 grown on CaF_2 substrates (see Table 2, section 2.2.3) as a function of the temperature curves at zero applied magnetic field is shown in Fig. 3.6. The critical temperature is estimated applying the standard 50% criterion of normal state resistance R_N at the onset of the transition. Thus, it has been estimated the critical temperature value $T_c \approx 20.5$ K, which is enhanced with respect to the ones reported in the literature [18-123].

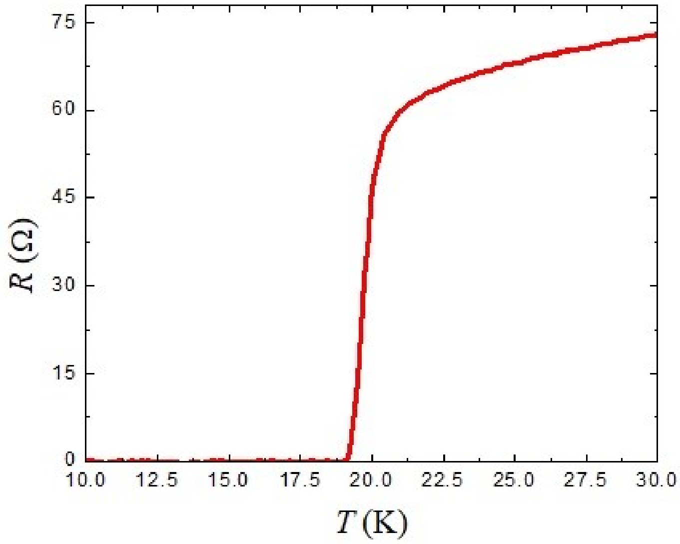

Fig. 3.6: R(T) of Fe(Se,Te) microbridge W20 at B = 0 T.

At fixed magnetic fields up to 9 T, $R(T)$ measurements provide the magnetic field–temperature (H–T) phase diagram, as shown in Fig. 3.7. In particular, the line of irreversibility field $H_{irr}(T)$ and the line of the upper critical field H_{c2} (T) are shown. The two lines have been defined by the standard 90% criterion of the R_N for $H_{c2}(T)$, while $H_{irr}(T)$ has been determined by the 10% criterion of the same R_N.

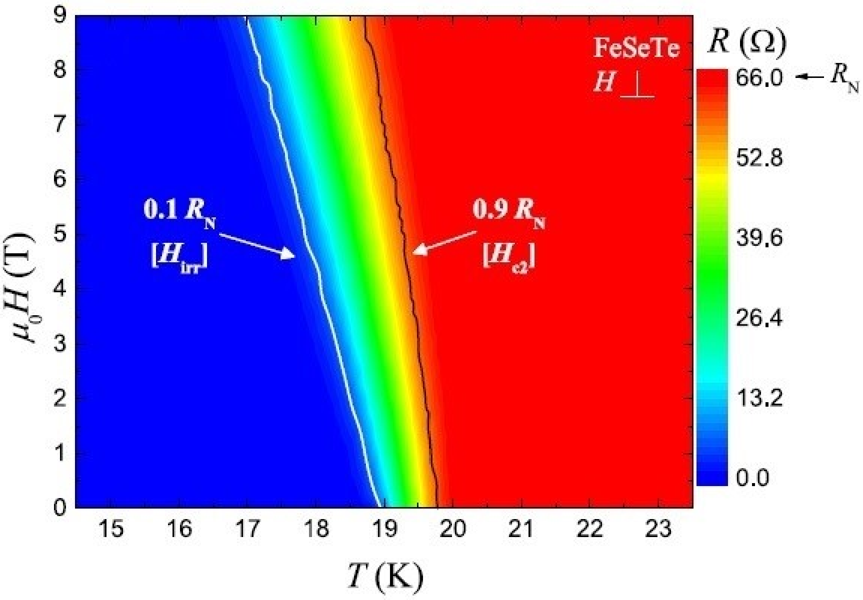

Fig. 3.7: H -T phase diagram of the Fe(Se,Te) thin film [178].

How we can see, the behaviour is slightly different. Indeed, H_{irr} is almost linear while H_{c2}, in the temperature range considered, follows the trend of the curve measured for samples Fe(Se,Te) grown on LAO substrates (see also Fig. 3.8) [192]. For the superconducting transition width is obtained $\Delta T_c(B = 0\ T) \approx 1$ K, and $\Delta T_c(B = 8\ T) \approx 2.0$ K. This last result can be interpreted as a sign of the good homogeneity of the samples. In addition, from the $H_{c2}(T)$ data it is also possible to evaluate the $H_{c2}(T)$ slope near T_c ($dH_{c2}/dT\,|\,_{Tc}$). It turns out to be a very steep slope near T_c due to the very low values about 8 $T\,/\,K$ (see the comparison in Fig. 3.8) [192]. Moreover, it is slightly enhanced respect to the value found in first-generation Fe(Se,Te) films [17]. This means that the second-generation Fe(Se,Te)/CaF_2 films shown a better robustness of superconductivity near T_c.

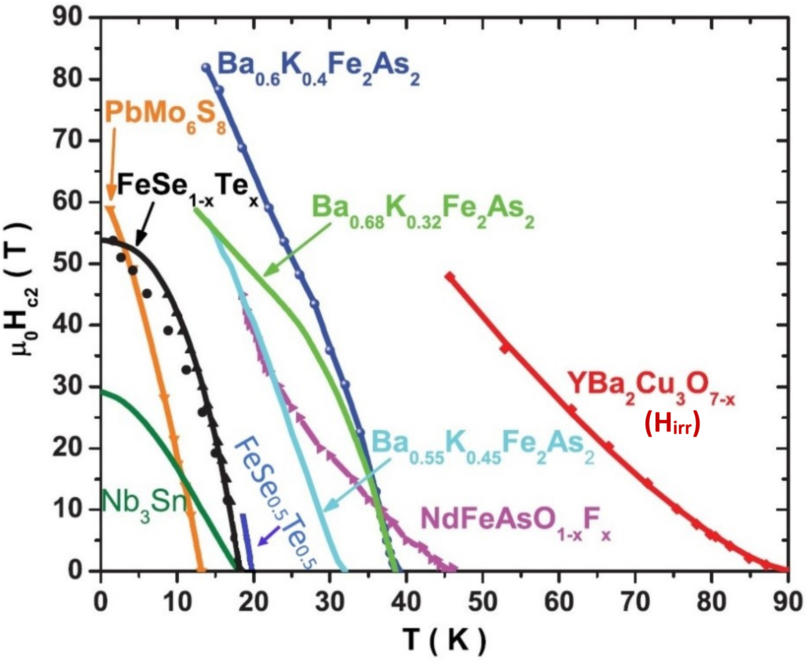

Fig. 3.8: Comparison of the upper critical fields of different materials: $H_{c2}(T)$ data for samples studied in this thesis is labelled in blue as $FeSe_{0.5}Te_{0.5}$, $H_{c2}(T)$ data for FeSe1-xTex (in black) as well as the other materials H_{c2} data and the YBCO irreversibility field H_{irr} are extracted from Ref. [192]

Pinning properties

The analysis of the *R(T)* curves at different applied magnetic fields allow us to estimate the pinning activation energy *U*, by the Arrhenius plot (see section 1.3), which is obtained by plotting the logarithm of the resistance as a function of the temperature inverse (see Fig. 3.9).

In this plot, $U\,(T, H)$ is the slope of the linear region after the onset of the superconducting transition.

The Tinkham approach [193], placing $t = T/T_c$, allows to factorize the $U(t, H)$ function into two contributions

$$U(t, H) = U_0(H)g(t),$$

where

$$g(t) = (1 - t^2)(1 - t^4)^{1/2}$$

In this way, we can extract the magnetic field contribution $U_0(H)$ to the pinning activation energy of Fe(Se,Te) samples (Fig. 3.10).

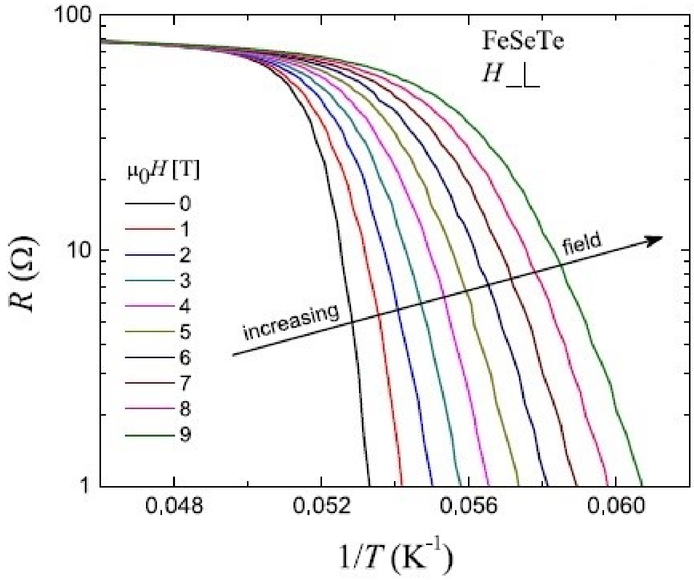

Fig. 3.9: Arrhenius plots at different magnetic fields for Fe(Se,Te) microbridge

As well know, $U_0(H) \propto H^{-\alpha}$, where the term α can assume different values depending on the dominant pinning regime. When $\alpha \approx 0$ we are dealing with a single-vortex pinning regime [194], while for $\alpha > 0.5$ we are in a collective pinning regime [195]. $U_0(H)$ is almost constant up to a crossover field value, found

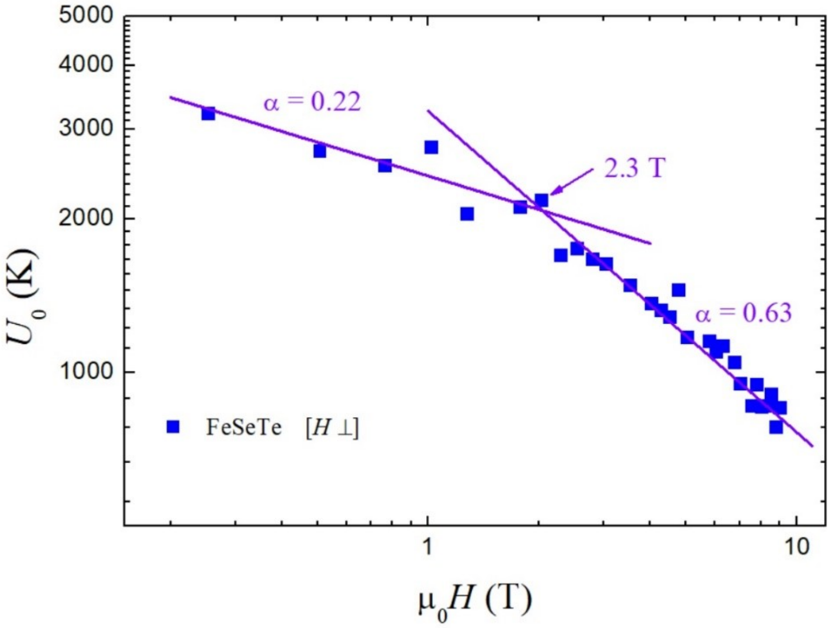

Fig. 3.10: Pinning activation energy as function of the applied magnetic field perpendicular to the film. The solid lines are fitting lines based on the formula $U_0(H) \propto H^{-\alpha}$.

at 2.3 T, being the data well fitted by $\alpha = 0.22$, whereas a more pronounced field dependence is observed for higher field with $\alpha = 0.63$. This finding suggests that in our films, the single-vortex pinning regime is active at least up to such a magnetic field, which means that the vortices in these materials are subject to the action of strong pinning. Indeed, pinning energy is larger than the vortex-vortex interaction.

Pinning Force

The pinning properties of the Fe(Se,Te) samples can be further explored studying the normalized pinning force ($f_p = F_p/F_{p,max}$) as a function of the normalized magnetic field ($h = H/H_{irr}$). The $f_p(h)$ curves can be evaluated using the relation $F_P = J_c B$, [eq. (1.25)]. For this purpose, we can perform J_c measurements by directly studying the I-V characteristics of Fe(Se,Te) thin films. It is easier to identify a modified Dew-Hughes scaling law

$$f_p = wC_1 h^{p_1}(1-h)^{q_1} + (1-w)C_2 h^{p_2}(1-h)^{q_2} \tag{3.1}$$

in which correction for the two components is related to the particular nature of their intrinsic pinning centers [18], [177]. In our case, the model curve represented by the solid line in Fig. 3.11 can be obtained by fixing $C_1 = 3.49$, $p_1 = 0.5$, $q_1 = 2$ and $C_2 = 6.75$, $p_2 = 1$, $q_2 = 2$. The only fitting parameter used is the weight w, with the resulting value $w = 0.66 \pm 0.04$. These parameters give a maximum of the curves between $h_{\max} = 0.2$, which is expected for surface core pinning (see section 1.1.3, table 1.1) and $h_{\max} = 0.33$, expected point core pinning. This result is compatible with what is reported in the literature for

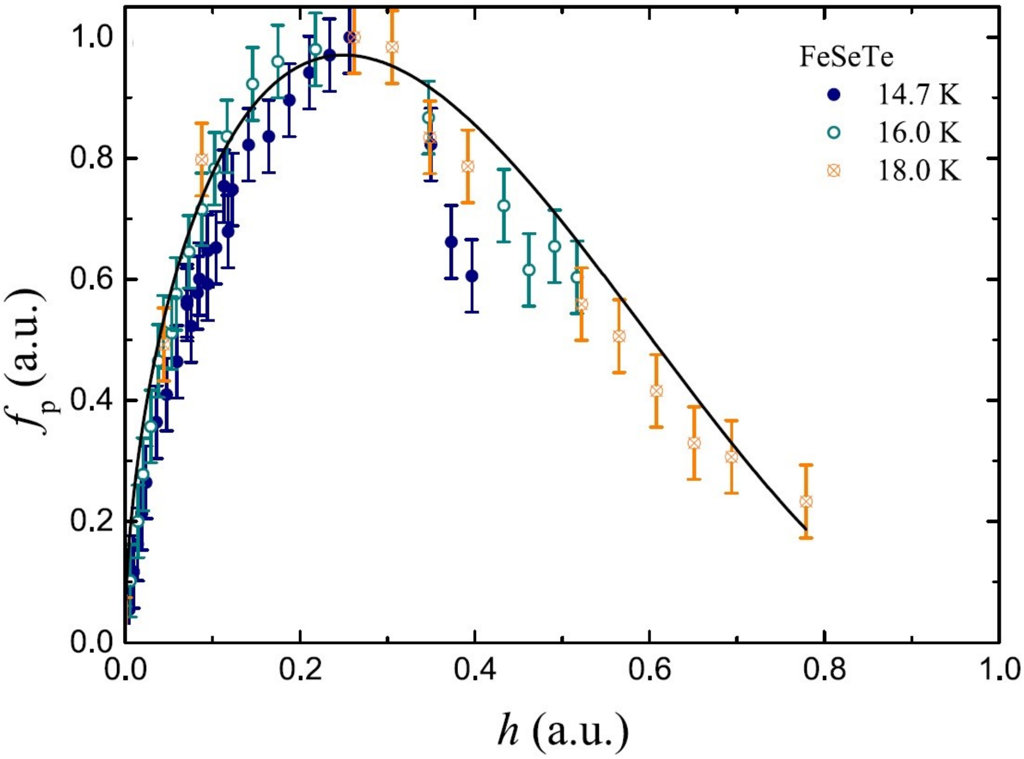

Fig. 3.11: Normalized pinning force as a function of normalized magnetic field at three different temperature. Solid line is the Dew-Hughes model fitting curve [178].

Fe(Se,Te) films on CaF_2 substrates, for which the presence of defects looking like local lattice displacements at very small scale, between 5 and 20 nm, and acting well as pinning centers, is highlighted [15, 18, 177]. This is thought to be responsible for the isotropic behaviour of Fe(Se,Te)/CaF_2 films

3.2.2 Flux Flow Instability study

It is well known that almost all superconducting materials, including HTSs and IBSs, can be affected by the presence of the Flux-Flow Instability (FFI). This phenomenon can be relevant for applications, since it can strongly compromise the high-current-carrying capability of any superconducting device. In addition, it is known that the presence of FFI in a superconducting sample is related to different material properties, among them we can mention the pinning due to natural or artificial defects, or the sample geometry [67-68, 71, 176, 196-199]. In particular, the FFI can be observed in samples whose dimensions are comparable to those of the filaments in superconducting cables. In the present section the stability of electric current transport in Fe(Se,Te) microbridge W20, in a regime well above the critical current have been examined, in order to reproduce the technical superconductors operative conditions.

Before proceeding with the study of the flux flow instability phenomenon, a further test on the validity of the experimental procedure has been done. We first have verified that during an instability phenomenon the sample holder would not heat up by joule heating due to the bias current in the wires which can alter the validity of the study. To exclude the possible presence of a thermal contribution to the observed

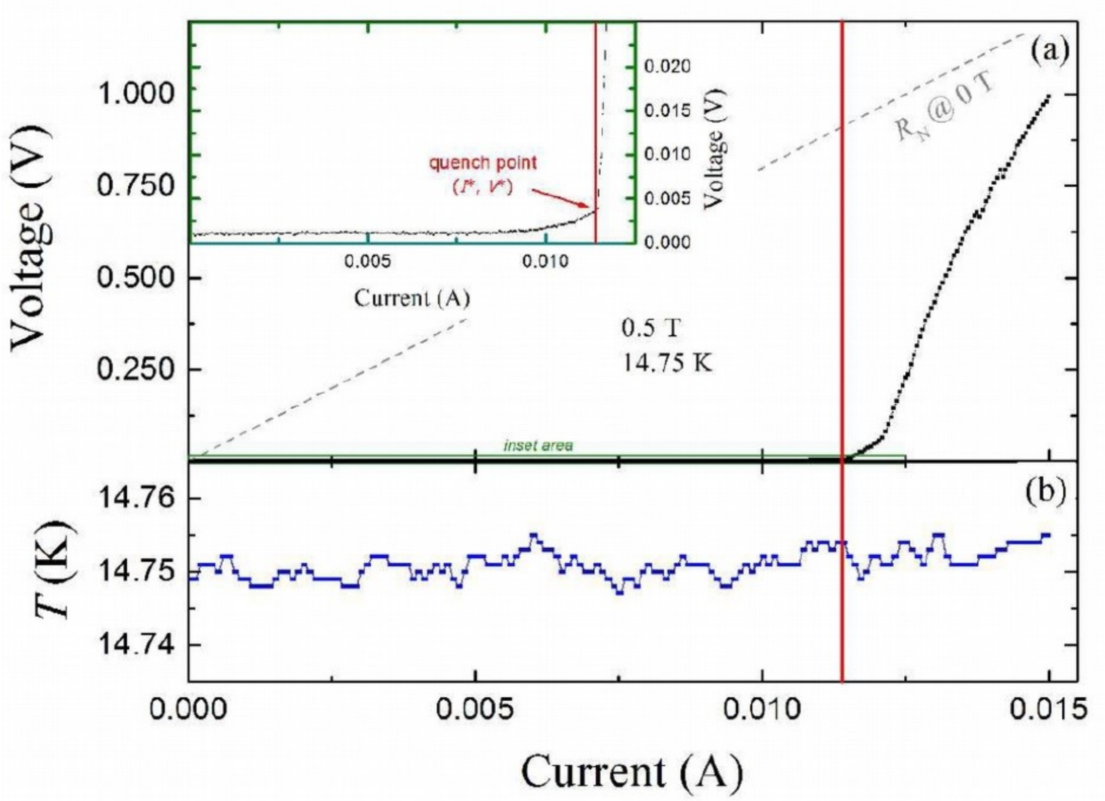

Fig. 3.12: (a) An example of Current-Voltage Characteristic acquired at a temperature of 14.75 K and in an applied magnetic field of 0.5 T. Inset: an enlargement of the low voltage data shown in the main panel. (b) The sample holder temperature variation as function of the bias current. The vertical red line in the panels marks the point at which the quench occurs [200].

instability due to the surrounding environment heating, the variation of the sample holder temperature T with the increasing bias current I has been studied [200]. In Fig. 3.12 (a), one of the measured I-V curve of the W20 microbridge is reported. It shows a clear evidence of the quench from the flux flow branch toward the normal state interpreted. The quench point at which the jump occurs is identified by the current-voltage instability parameters (I^*, V^*), as reported in the inset of the figure.

In Fig. 3.12 (b), it is clearly visible that the temperature excursion does not exceed the stability range, thus a complete recover of the sample holder temperature to the flow temperature during the pulse delay PD is achieved (see section 2.2.3). This ensures that the pulse current mode with the employed parameters is a proper choice.

The behaviour exhibited by the W20 sample I-V curves at a fixed temperature and in different applied magnetic field is reported in Fig. 3.13. Here it is evident the signature of such rapid transitions as current instabilities.

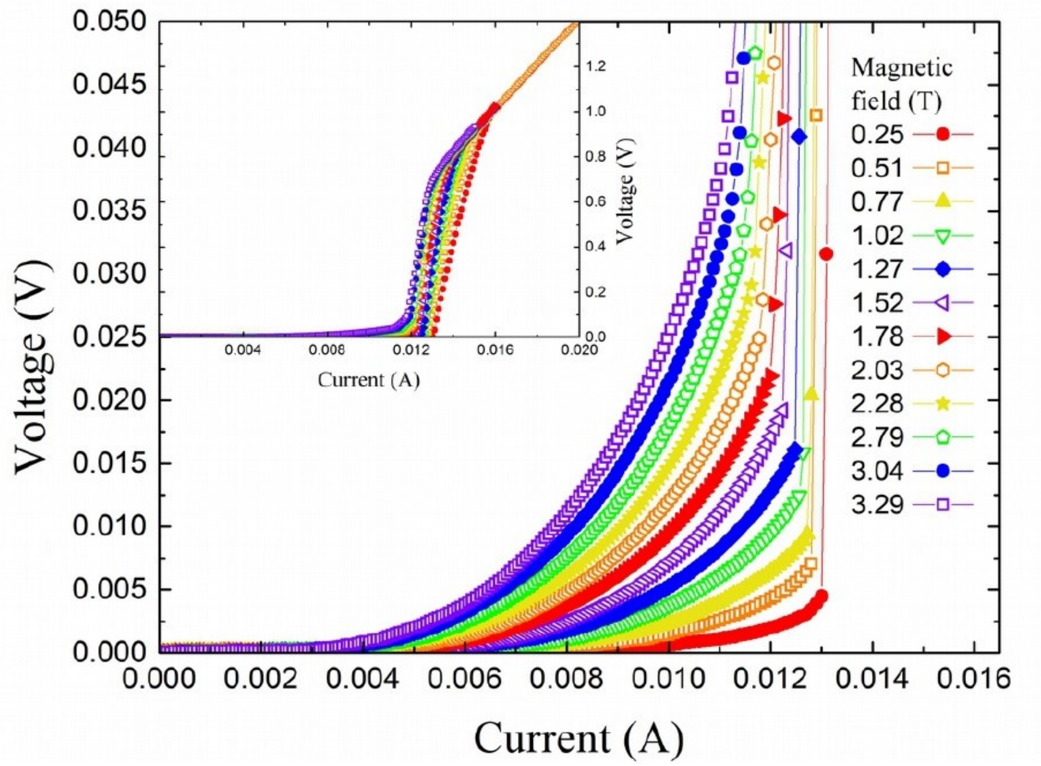

Fig. 3.13: Enlargement of low voltage region of Current-Voltage Characteristics acquired at a constant temperature of 16.00 K and in different applied magnetic fields of a 20 µm wide microbridge. In the inset: the I-V curves in the whole measured range [200].

The Figures 3.14 (a) and (b) report the dependence of the instability current I^* on the magnetic field, where it can be recognized an almost constant I^* behaviour. While, the critical current, defined by a standard 1 µV/cm criterion, rapidly decreases as a function of the perpendicular applied magnetic field.

In addition, as shown in Fig. 3.14 (b), at 16 K, the instability current behaviour is almost constant in magnetic field, although the pinning as expected decreases. This feature is usually observed in high-T_c

superconductors [64], but not in low-T_c materials [174]. Such instability current behaviour in the applied field can be interpreted as a robust wide range of current stability above the critical current, similarly to what happens in superconducting materials modified with a proper pinning landscape [196-197]. The peculiar behaviour of I^* in high-T_c superconductors is related to the presence of Larkin-Ovchinnikov (LO) electronic instabilities [12]. Moreover, in section 1.1.4 is reported the critical vortex velocity v^* as a function of the applied magnetic field, with v^* evaluated from the measured critical voltage curve V^* [eq. (1.34)] as $v^* = V^*/(\mu_0 HL)$ [201]. By plotting the obtained v^*, it is possible to recognize the power law behaviour $v^* \propto \mu_0 H^{-\frac{1}{2}}$ which is usually attributed to the presence of FFI triggered by intrinsic electronic mechanisms [64].

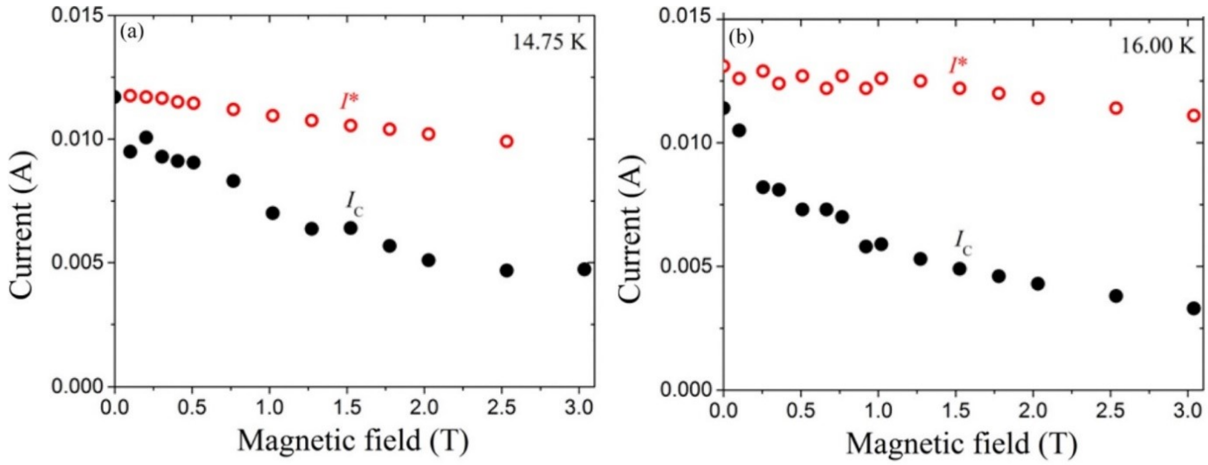

Fig. 3.14: Critical current Ic, defined by a standard 1 μV/cm criterion, and instability current I, defined as the current corresponding to the quench point in the I-V, as a function of the applied magnetic field for (a) T = 14.74 K and (b) T = 16.00 K [200].*

On the other hand, the transition from the flux flow branch to the normal state in our case it is not that sudden jump usually observed when pure electronic mechanisms trigger the FFI. Therefore, it is worthwhile to assess the possible presence of a thermal contribution to the observed instability.

In section 1.1.4, it has been introduced the Bezuglyj and Shklovskij (BS) macroscopic parameter B_T whose evaluation can add information about the contribution of pure Joule self-heating on the observed current instabilities. Indeed, it separates the region where non-thermal intrinsic ($B \ll B_T$) or pure heating extrinsic mechanisms ($B \gg B_T$) of the instability dominate.

B_T has been estimated following BS approach from eq. (1.36), as shown in section 1.1.4 [202]: $B_T = \frac{0.374 \cdot e \cdot h \cdot \tau_\varepsilon}{k_B}\left(R_N \frac{W}{L}\right)$. We have estimated τ_ε using the LO eq. (1.33), $R_N = 80\ \Omega$, and h is evaluated from $P = IV$ as a function of sample temperature. From these data, the B_T parameter is estimated to be major than 20 T, confirming the secondary relevance of the contribution from extrinsic thermal mechanisms in FFI instability phenomenon in Fe(Se,Te)/CaF$_2$ thin films [203].

The presence of FFI in a superconducting sample is also related to the sample geometry. For this reason, different wide microbridges have been studied, well above and below W20 microbridge, namely W1K and W10 samples respectively. In Fig. 3.15, a comparison of the three samples I-V curves at similar reduced temperatures $t = T/T_c(0)$ and at the same applied magnetic field $B = 0.5$ T is shown.

As has just been studied for **W20** sample**,** the observed FFI is slightly smoothed and it is interpreted as the result of the coexistence of thermal and electronic mechanisms [200-201].

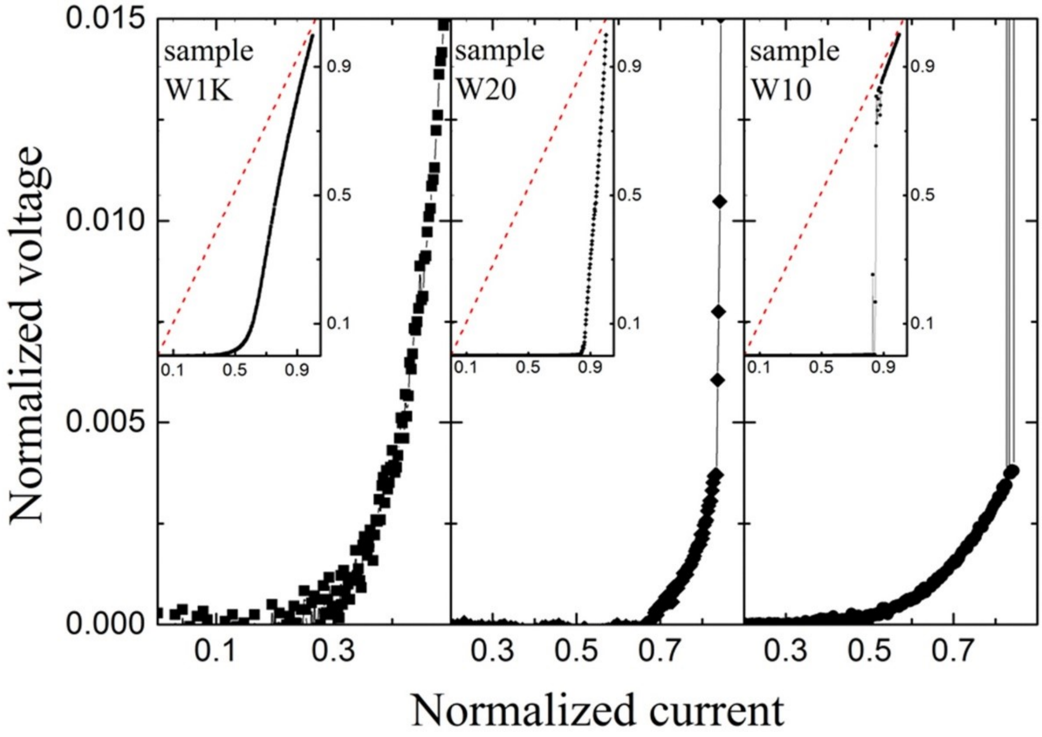

Fig. 3.15: I-V curves of the three analyzed samples in the low voltage region. The current value of the current feeded to the sample, i. e., 30 mA for W1K, 19 mA for W20 and 30 mA for W10. The voltage values are normalized to the maximum measured value of the voltage (0.8817 V, 1.39284 V and 0.93603 V respectively for W1K, W20, W10)). The field applied for alla three samples is 0.5 T. (insets) the three curves in the full range; the red dashed line is the normal resistivity line [203].

In the case of **W1K** microbridge, the low voltage region, where the sudden voltage jump is usually observed, is free by this characteristic voltage jump associated to the Flux-Flow Instability. This FFI lack can be explained by the wide geometry of the sample. Indeed, the heat-transfer coefficient h_S between the sample and the substrate decreases as the bridge width is increased and the self-heating effects are enhanced [199]. In wide bridges, the temperature increase due to the less efficient heat removal prevents the vortices from reaching the critical velocity. Although this observation strictly depends on the material under investigation as well as on the substrate and cooling environment [73] [176].

Concerning **W10**, this sample has been realized in order to obtain a predominance of electronic mechanisms by maximizing h_S. Thus, it is not surprising that the transition in this case is steeper than that of the sample W20. In this sample, the predominance of intrinsic mechanisms is confirmed through the analysis of the dependence of critical vortex velocity by the magnetic field. As shown in Fig. 3.16, we found that the v^* behaviour is in agreement with that expected in the case of a FFI triggered by electronic mechanisms, i.e. a $B^{-1/2}$ dependence at low field values followed by a rather constant value at higher fields [65-68, 204-205].

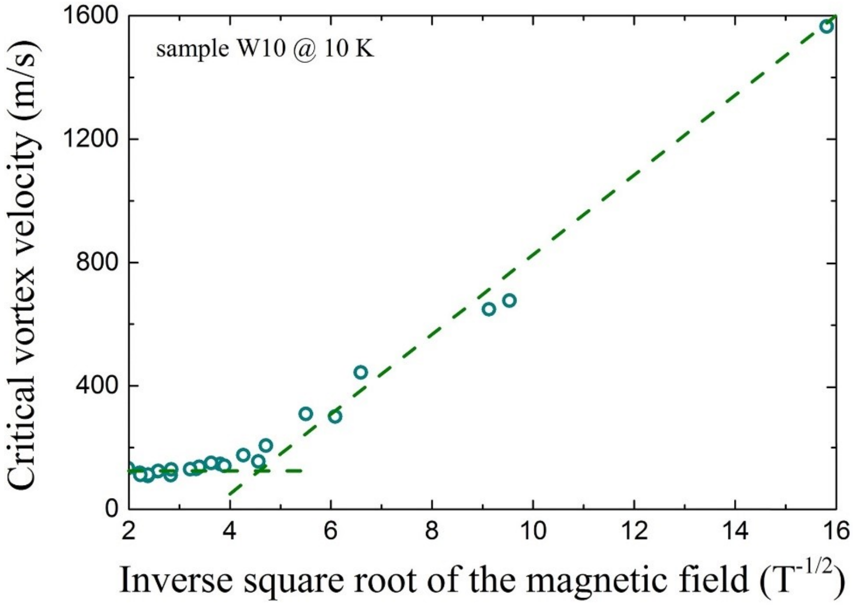

Fig. 3.16: Behavior of the critical vortex velocity as a function of the inverse of the square root of the applied magnetic field. The dashed lines are guides for the eye [203].

Flux-Flow Instability in the current-voltage characteristics of samples W20 and W10 allows the study of the relation between the instability current and the critical current based on the possible coexistence of both thermal and electronic mechanisms (W20), as well as on the predominant intrinsic mechanism (W10). In Fig. 3.17, the difference between the instability current and the critical current normalized to the critical current value at zero field $\Delta i = (I^* - I_c)/I_c(0)$ is reported as a function of the applied magnetic field for both samples W20 and W10 at two different temperatures. In both cases, although the increase of the temperature implies a reduction of the critical and the instability currents, the values of Δi are higher for the upper temperature value in the whole magnetic field range (I^* decreases less than I_c). This feature is interpreted as a consequence of two concurrent effects. First, a higher stability in the current conduction at higher temperature, due to a weaker contribution from the extrinsic thermal mechanism to the FFI [191]. Second, regardless of the pinning mechanism, the pinning strength has a weaker influence on the instability current with respect to the influence on the critical current [68, 196-197].

Moreover, a crossover between an increasing Δi and a quite constant behaviour with the increasing applied magnetic field is observed in both samples. In particular, the crossover field value is around 1 T for all the curves. This behaviour is still a consequence of the weaker dependence of the instability current on the applied magnetic field with respect to the critical current. The substantial independence of I^* on B both in the case of a thermal origin of the instability and in the case of intrinsic electronic mechanisms triggering the FFI can be inferred by the data reported in the insets of Fig. 3.17. Indeed, the percentage variation of *I** in the considered range is always less than 24%, with a minimum value of about 3% for sample W10 at 15 K. On the contrary, the percentage variation of I_c in the same range is always more than 60%. In particular, in the case of intrinsic electronic mechanisms, the almost *B*-independent behaviour of *I** is the result of the influence of the peculiar pinning landscape [196-197].

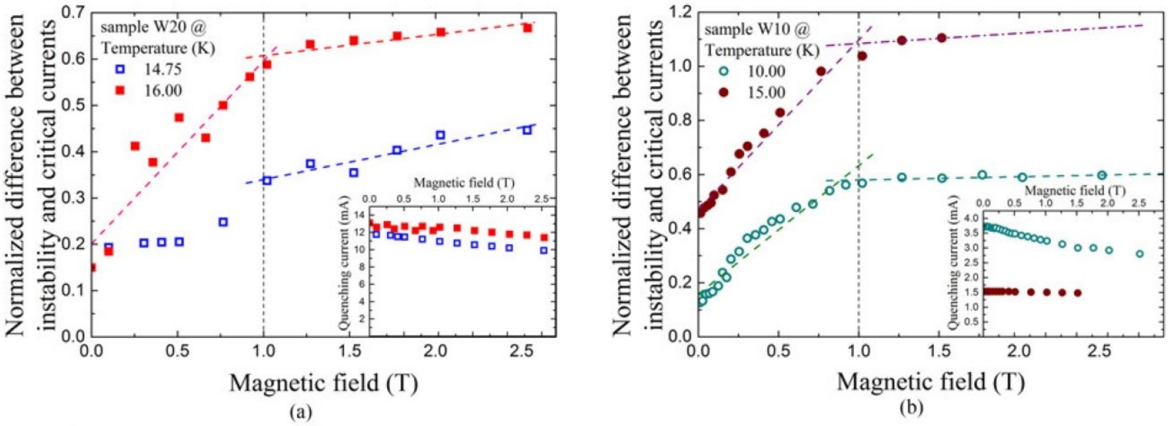

Fig. 3.17: Behavior of the difference between the quenching and the critical current normalized to the critical current value at zero field at different temperatures for (a) sample W20 and (b) sample W10. Here, the data are normalized to the Ic (0) values 11.7 mA at 14.75 K and 11.4 mA at 16.00 K for sample W20, and 3.24 mA at 10.00 K and 1.05 mA at 15.00 K for sample. The dashed lines are guides for the eye. (Insets) Curves of the quenching current as a function of the applied magnetic field for (a) sample W20 and (b) sample W10 [203].

Thus, from the analysis of the correlation between *I** and I_c it was possible to verify that intrinsic mechanisms give a significant contribution to the Flux Flow Instability.

Moreover, we can make a comparison with other materials in which electronic or thermal mechanisms dominate. In Fig. 3.18, the Δi curves are shown as a function of the applied magnetic field as obtained by the data for HTS ($YBa_2Cu_3O_{7-\delta}$) reported by Doval et al. in [19] and for LTS (Nb) reported by Grimaldi et al. in [174]. In the case of HTS analysed by Doval et al., the quenching current *I** is associated with pure thermal mechanism [73]. On the contrary, in the LTS case the FFI has been proven to be triggered by pure electronic mechanisms [174-175, 197]. In the last case, we note a very similar behavior of Δ*i*(*B*) to those of the Fe(Se,Te)/CaF_2 thin films.

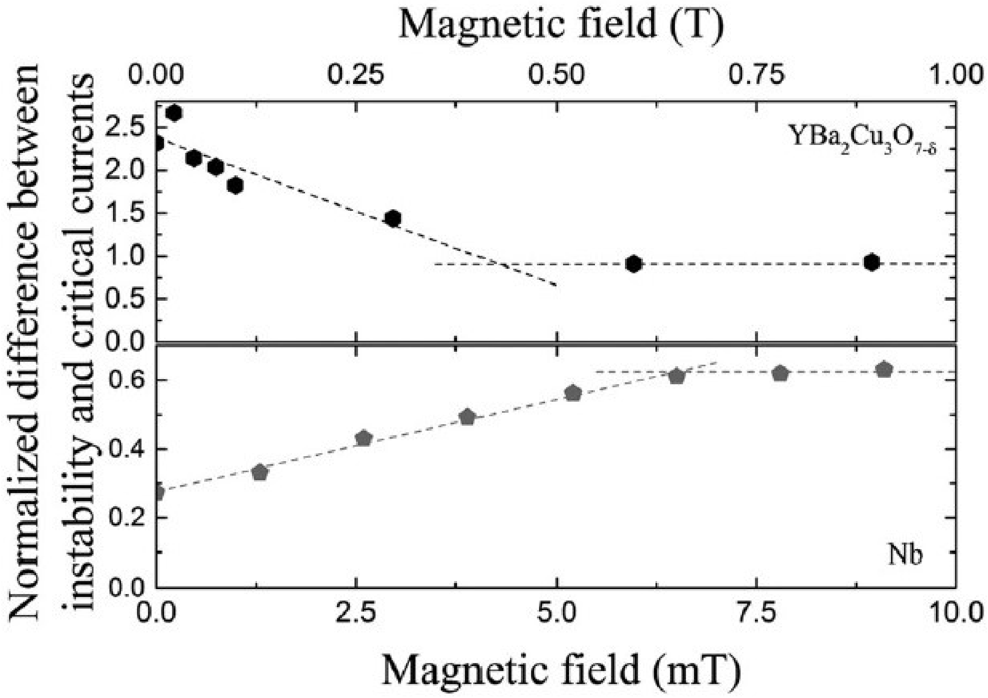

Fig. 3.18: Behavior of the difference between the quenching and the critical current normalized to the critical current value at zero field and different temperatures for (upper panel) an HTS sample as by the data reported in [19] and (lower panel) a LTS sample as by the data reported in [174]. The dashed lines are guides for the eye [203].

3.3 Conclusions

In order to verify if the measuring environment used has any influence on the electric transport measurements, current-voltage characteristic measurements have been carried out in three different measurement environments on LTS ultra-thin films. In particular, we considered the cooling in a liquid Helium cryostat and in a cryogen-free cryostat in both dynamic (flowing) and static gas conditions.

A slightly higher stability can be inferred in liquid He, in which fairly larger in-stability current values can be achieved with higher critical voltages, too.

The differences among the instability current $I*$ values measured in the three different environments decrease with the increase of the magnetic field, and this is more pronounced for the NbTiN material.

Moreover, $P*$ is slightly higher in LHe below 2 T. The magnetic field dependence of $P*$ is a fingerprint of the intrinsic microscopic mechanisms of vortex motion instability.

However, the different cooling methods do not affect the critical currents at all, whereas the instability parameters result reproducible within few percent, so that in practice the investigated cooling methods result suitably efficient also for high current transport measurements.

Once the efficiency of the cooling mode has been determined, a study of some properties relevant for applications of a second generation Fe(Se,Te) films grown on CaF_2 substrates has been effectuated by electrical transport characterization.

By means of R(T) measurements at different magnetic fields, the phase diagram H-T has been obtained.

A considerable increase in T_c has been observed compared to first-generation films. The evidence of a reduced transition width $\Delta T_c(B)$, from 0 T up to 8 T between the H_{irr} and the H_{c2} lines denotes a good sample homogeneity, better than that of first-generation films. Moreover, the $H_{c2}(T)$ slope near T_c ($dH_{c2}/dT\,|_{Tc}$) is slightly enhanced respect to the one of the first-generation films, thus demonstrating greater robustness of the superconductivity near T_c.

From R(T) measurements was also possible to estimate the pinning activation energy by the Arrhenius plot has allowed to determine that the single-vortex pinning regime is active up to at least 2 T, which means that vortices are subject to strong pinning. The pinning properties have been studied by means of the normalized pinning force and the Dew-Hughes scaling law by which we have determined the pinning center displacements within 5 to 20 nm and the consequent isotropic behaviour of Fe(Se,Te)/CaF_2 thin films.

Other information about Fe(Se,Te)/CaF_2 films have been extracted by Flux Flow Instability. We first have verified that during an instability phenomenon the sample holder would not heat up by joule heating which can alter the validity of the study. The test has showed that a complete recover of the sample holder temperature to the flow temperature during the pulse delay is achieved.

By the I-V curves, the plot of the instability and critical current values has revealed the increasing I*-I_c difference in magnetic field and in temperature which is generally related to electronic instabilities. This origin is also confirmed by the study of the instability velocity v*. However, the presence of thermal mechanisms is also highlighted by a smoother voltage jump. Indeed, our results enlighten the existence of many points of contact between our experimental findings and the literature related to flux flow instabilities triggered by intrinsic electronic mechanisms in high-T_c superconductors. On the other hand, the estimation of the sample temperature increase and the calculated value of the Bezuglyj-Shklovskij parameter identify the contribution from extrinsic thermal mechanisms as of a secondary relevance. Moreover, the current transport has been found to be intrinsically stable, even as a function of the magnetic field, thus confirming the high-field performance of these materials for applications.

By studying different size microbridges, we have seen that for too large dimensions the heat exchange prevails and the FFI does not occur. For the 20 μm wide microbridge the coexistence of thermal and electronic mechanisms is observed while, for the 10 m wide microbridges, electronic mechanisms are predominant.

Then, the relation between the instability and the critical current has been analyzed both in the case of FFI ascribed to the coexistence of extrinsic thermal and intrinsic electronic mechanisms and in the case of predominant intrinsic electronic mechanisms. The difference between the instability current and the critical current normalized to the critical current value at zero field reported as a function of the applied magnetic field for both samples at two different temperatures has revealed that I^* decreases less than I_c. This feature is interpreted as a consequence of a higher stability in the current conduction at higher temperature, due to a weaker contribution from the extrinsic thermal mechanism to the FFI and by the weaker influence of the pinning mechanism on the instability current with respect to the influence on the critical current.

On the basis of the results obtained in the present study, it can be seen that the contribution of the intrinsic mechanisms to the FFI in IBS leads to a substantial independence of the instability current from the intrinsic pinning influence. Moreover, it is observed the presence of a crossover from an increasing difference between the quenching and the critical current to a quite constant value as the applied magnetic field is increased.

4 THERMAL CHARACTERIZATION OF TECHNICAL SUPERCONDUCTORS

As seen in section 1.4, electrical and thermal stability of technical superconductors is based on key parameters as thermal conductivity, residual-resistivity ratio (*RRR*), normal zone propagation velocity (*NZPV*). High values of these parameters are desired to protect superconducting magnets in case of quench, as the Joule heating generation term is proportional to the electrical resistivity (ρ) of the normal matrix [148, 153].

In Section 4.1, the thermal conductivity data for Bi-2212 round wires samples reacted at different pressures, namely 1, 10 and 100 bar, have been examined. The κ has been studied in magnetic fields up to 19 T.

Moreover, the determination *RRR* of the normal-metal matrix is a key parameter for the electrical and thermal stability of technical superconductors because it determines the temperature dependence of thermal conductivity κ [148]. In particular, the higher the *RRR*, the higher the κ. The superconducting transition at high T impedes a direct measurement of the *RRR* of the matrix for HTS conductors. In Bi-2212 wires, the superconducting embedded filaments in Ag matrix have required the chemical etching treatment, described in section 2.3.1, to dissolve the filaments of Bi-2212 leaving the Ag matrix unchanged. Thus, in section 4.2, the *RRR* measurements have been performed on the three aforementioned samples.

Furthermore, in section 4.3, we will verify the validity of a practical formula for the calculation of the normal zone propagation velocity (*NZPV*) within Bi-2212 round wires.

4.1 Thermal Conductivity measurements

Thermal conductivity of samples reacted at different pressures, namely 1, 10 and 100 bar, seen in Section 2.3.1, has been examined in magnetic fields up to 19 T. The experimental *κ(T)* curves of the samples are presented Figure 4.1 [206]. Thermal conductivity κ has been measured in the range of temperatures from ≈ 4 - 40 K. Measurements have been performed at B = 0, 1, 7 and 19 T with the field oriented perpendicularly to the thermal current. Two additional data points have been taken at T ≈ 55 K and ≈ 77 K in zero field to check the trend in an area where κ(T) tends to be almost constant because the purity of the material becomes less important when the electron-phonon scattering dominates over the electron-defect one [207].

The thermal conductivity curves *κ(T)*, at B= 0, 1 and 7 T, exhibit a clear peak whose intensity lowers as

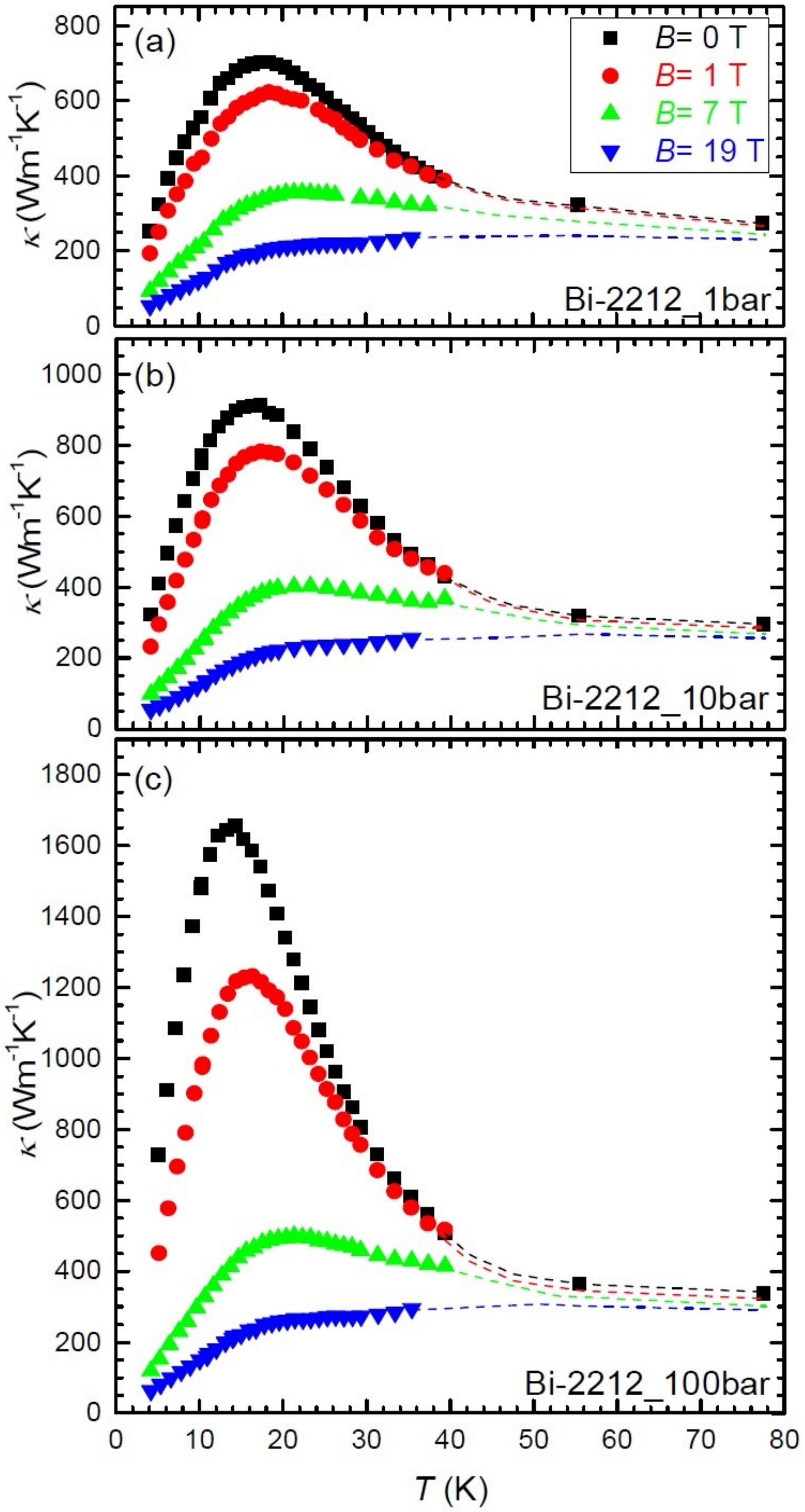

Fig. 4.1: Temperature dependence of the thermal conductivity at different fields for Bi-2212 wires reacted at 1 (a), 10 (b) and 100 bar (c). Dashed lines are guides to the eye [182] [206].

	Bi-2212_1bar	Bi-2212_10bar	Bi-2212_100bar
$\kappa_{peak}(0\ \mathrm{T})$	700 $\mathrm{Wm^{-1}K^{-1}}$	910 $\mathrm{Wm^{-1}K^{-1}}$	1650 $\mathrm{Wm^{-1}K^{-1}}$
$\kappa(20\ \mathrm{K},\ 19\ \mathrm{T})$	210 $\mathrm{Wm^{-1}K^{-1}}$	225 $\mathrm{Wm^{-1}K^{-1}}$	260 $\mathrm{Wm^{-1}K^{-1}}$
Filament fraction ($s_{fil.}$)	0.22	0.22	0.22
Silver fraction (s_{Ag})	0.54	0.54	0.54
Silver-alloy fraction (s_{AgMg})	0.24	0.24	0.24
RRR of the normal-metal matrix	95	110	220
RRR of Ag	90	104	208

Table 4.1: Structural, thermal and electrical properties of the investigated Bi-2212 [206].

the field increases. At 19 T the peak is barely distinguishable and $\kappa(T)$ increases almost monotonically. In Fig. 4.2, the pairs constituted by the temperature T_{peak} at which the peak occurs and the maximum value of the thermal conductivity peak κ_{peak}, which identify the peak position at B= 0, 1, 7 T, are reported for the three investigated samples, even with the best-fit straight line. In this graph, it can be seen the linear decrement of the peak of the thermal conductivity as a function of the temperature. The values corresponding to the maximum of the $\kappa(T,\ B=0)$ curve have been summarized in Table 4.1. It can be easily seen that the heat-treatment at 100 bar has increased the $\kappa_{peak}(0\ T)$ by ≈ 135 %, but the field-induced reduction of κ is more pronounced for these wires.

In Table 4.1, κ measured at 19 T and 20 K has been reported, too. Indeed, 20 K is the temperature to which the beginning of the $\kappa(T)$-curve sector weakly dependent on T approximatively corresponds. Thus, it can be observed that increasing the reaction pressure from 1 to 100 bar, the resulting improvement of κ is only by 25 % at high fields.

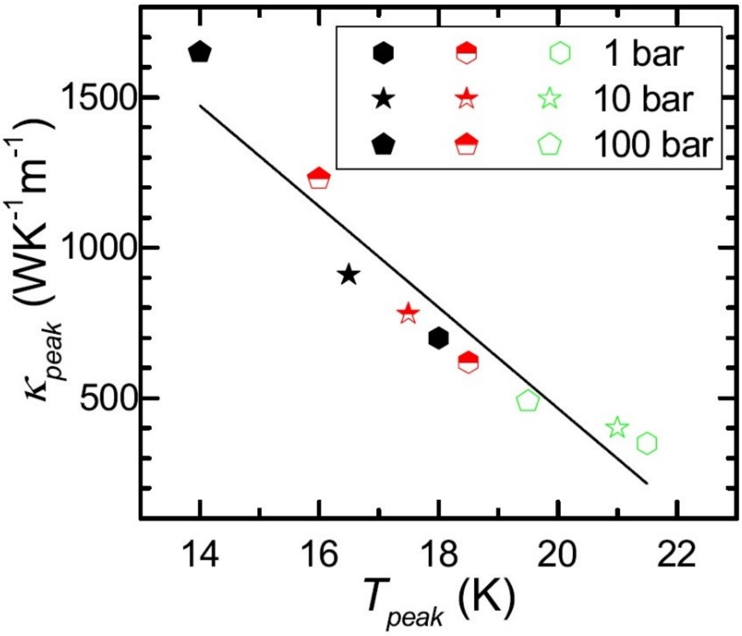

Fig. 4.2: the coordinates of the _(T)-curve peak at 0 T (full symbols), 1 T (half-full symbols) and 7 T (open symbols), along with the best-fit straight line [182] [206].

4.2 *RRR* measurements

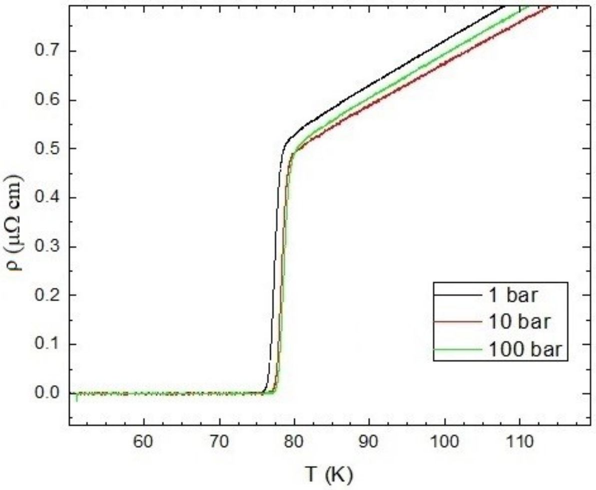

Fig. 4.3: Resistivity of Bi-2212 round wires reacted at different pressures, namely 1, 10 and 100 bar

In Fig. 4.3, the resistivity of the three superconducting wires, reacted at the different pressures 1, 10 and 100 bar, is shown. Being the RRR defined as $R(273\ K)/R_{Res}$, before the R_{Res} of the Ag matrix could be measured by means of resistance measurements, the superconducting filaments have been removed, from short conductor pieces, dissolving the Bi-2212 in glacial acetic acid (see section 2.3.2).

The residual resistance R_{Res}, and room-temperature electrical resistance, as measured in the etched Bi-2212_100bar sample, are reported in Figure 4.4. The *RRR* of the non-superconducting fraction of the conductor (Ag and AgMg), defined as $R(273\ K)/R_{Res}$, is about 220.

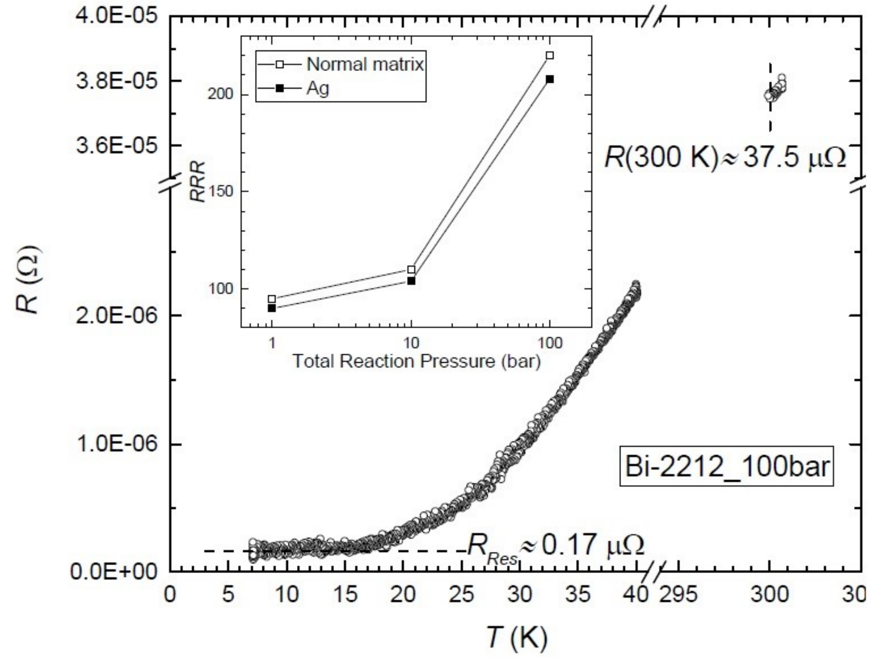

Fig. 4.4: Low- and room-temperature electrical resistance measured on a 2-mm-long Bi-2212 conductor reacted at 100 bar, in which the superconducting filaments have been dissolved away in glacial acetic acid. The inset shows the dependence of the normal-matrix and Ag RRR on the heat treatment pressure [206].

The *RRR* of Ag can be determined as follows. The relative fraction of Ag and AgMg in the cross-section is known for all the investigated wires (data summarized in Table 4.1). The resistance *R* of the non-superconducting fraction of the conductor is the equivalent resistance value of two parallel resistors R_{Ag}

and R_{AgMg}. The RRR of Ag can be determined considering that, at low T, $\rho_{Ag} \ll \rho_{AgMg}$ whilst at 300 K $\rho_{Ag} \approx 16.1$ nΩm and $\rho_{Ag} \approx 19.7$ nΩm [26]. The parallel resistor calculation at low T and at 300 K, leads to a RRR of Ag of ~ 208.

In the inset of Fig. 4.4 the RRR data versus the three different overpressures relative to the heat treatments undergone have been plotted.

4.3 Error on *NZPV* evaluation

The other parameter of fundamental importance for the thermal stability of a technical superconductor is *NZPV*. In section 1.1.7, as it has been seen, the eq. (1.45) represent an analytical expression for the *NZPV* with adaptations for the case of HTS. However, the calculation of the *NZPV* from eq. (1.45) is hindered by the need of details about the $\kappa(T)$ curve of the conductor at the conditions realized in a magnet. In order to bypass these difficulties, an approximation of eq. (1.45) has been derived for REBCO CCs in eq. (1.52). In this section we show the necessary measurements to calculate the error made in the use of the practical formula for the calculation of the *NZPV* for the REBCO CCs applied to the Bi-2212 round wires. In section 1.5 the error has been evaluated as $\varepsilon = 1 - \sqrt{1-\Delta}$ with:

$$\Delta = \frac{\left.\frac{1}{K}\frac{dK}{dT}\right|_{T_t} \cdot \int_{T_{Op}}^{T_t} C(T)dT}{C(T)}$$

therefore, Δ is the product of three factors that can be obtained from thermal conductivity measurements, thermal capacity measurements and by the computation of enthalpy.

Since the $\kappa(T)$ at high T is approximated by a straight line passing through the points at 55 and 77 K, the term $\left.\frac{dK}{dT}\right|_{T_t}$ can be calculate as the angular coefficient of the $\kappa(T)$ curves linear fit due to the expected value $T_t > 30\ K$.

The heat capacity curve $C(T)$, measured as indicated in section 2.3.3, is shown in Fig. 4.5. Integrating this function between the lower integration end, equal to the operating temperature of 4.2 K, and the upper integration end equal to the variable T_t, we obtain the enthalpy as a function of the T_t (see Fig. 4.6. The resulting error $\varepsilon(T)$ is then calculated and shown in Fig. 4.7 for the three sample in 7 T and 19 T magnetic fields.

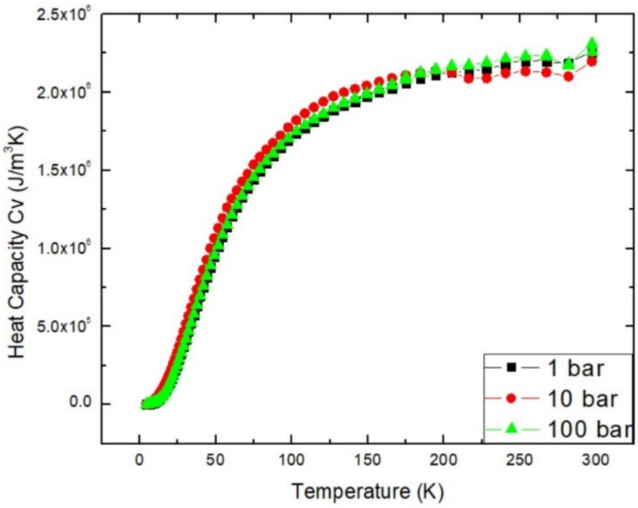

Fig. 4.5: Heat Capacity of the three Bi-2212 samples reacted at 1, 10 and 100 bar.

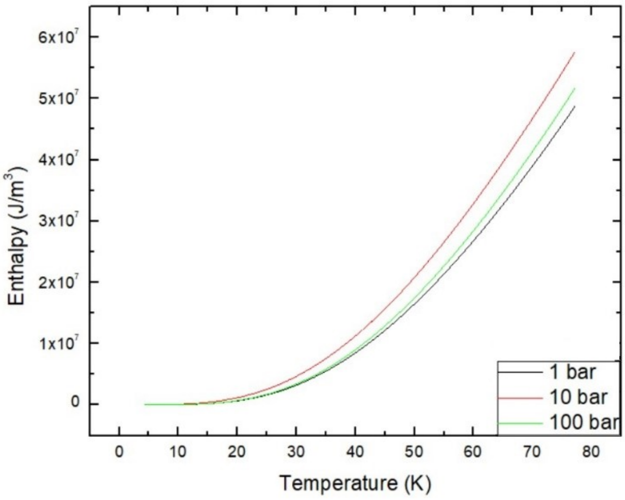

Fig. 4.6: Enthalpy calculated integrating Heat Capacity curve from 4.2 K to T_t.

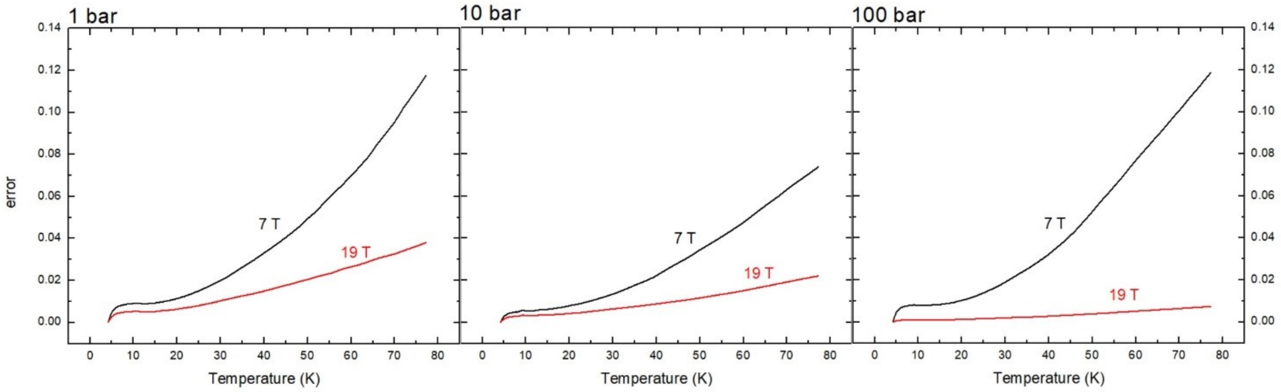

Fig. 4.7: Error on NZPV function calculated by approximation of NZPV practical formula for REBCO CC.

4.4 Discussion

In section 1.5, it has been reported that the overall longitudinal thermal conductivity (κ_{tot}) is the weighted sum of the thermal conductivity of each material composing the conductor $\kappa_{tot} = \sum \kappa_i \, s_i$. As concerns cross-section fractions s_i for the investigated wires, in Table 4.1 are reported the Bi-2212 (or filament weigth s_{fil}), Ag (s_{Ag}), and AgMg (s_{AgMg}) data. Concerning the relative thermal conductivity κ_i, for the filament κ_{fil} of Bi-2212 is below ≈ 1 $\mathrm{WK^{-1}m^{-1}}$ at T $\lesssim$ 150 K [26]. From the wire thermal conductivity values reported in Fig. 4.1 one deduces that its contribution to the overall κ_{tot} is negligible. The thermal conductivity κ_{AgMg} of AgMg used in the production of Bi-2212 wires has been reported in [26]. We can evaluate that its contribution to the overall κ is lower than ≈ 10 % at T $\lesssim$ 40 K and decreases at lower T. Finally, Fig. 4.8 shows κ_{Ag}(T) for the three investigated samples (green, purple and pink points), as evaluated considering that $\kappa_{Ag}(T) \approx \left(\kappa(T) - \kappa_{AgMg}(T) s_{AgMg}\right)/s_{Ag}$, using the experimental κ of Fig. 4.1, s_i values reported in Table 4.1 and κ_{AgMg}(T) from [26]. In the same plot we have included the κ(T) curves for Ag samples with different *RRR* from the literature [26, 160].

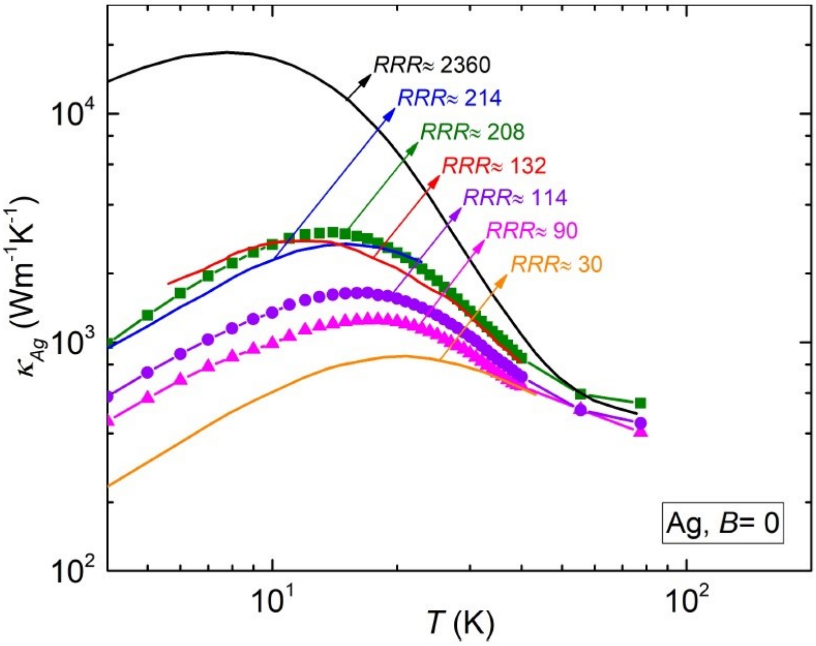

Fig. 4.5: Temperature dependence of the thermal conductivity of Ag samples of different purity; RRR references from top to bottom: black [160], blue [26], green (Bi-2212_100bar) [206], red [160], purple (Bi-2212_10bar) and pink (Bi-2212_1bar) [206], orange [160].

For the sample Bi-2212_100bar, the measured κ(T) and *RRR* of Ag are consistent within the experimental accuracy with the results shown in [26] on a stand-alone Ag sample provided by Oxford Superconducting Technologies. The stand-alone Ag sample has been heat treated using a standard Bi-2212 schedule in 1 bar O_2 and a *RRR* of 214 has been measured (blue line in Figure 4.8) [26]. Since the stand-alone sample is from the silver stock used in wire production, we infer that matrix contamination by Bi-2212 elements when reacting the wire at 100 bar is low.

On the other hand, element contamination effects cannot be neglected when the conductor is reacted at pressures ≲ 10 bar. Indeed, the lowest *RRR* of Ag (≈ 90) has been measured on the conductor reacted at 1 bar. However, this *RRR* reduction of a factor of ≈ 2 is not so dramatic if we consider that, in the case of Nb_3Sn wires, a complex conductor layout that includes reaction barriers around the filaments is necessary to keep the *RRR* above ≈ 100 [185].

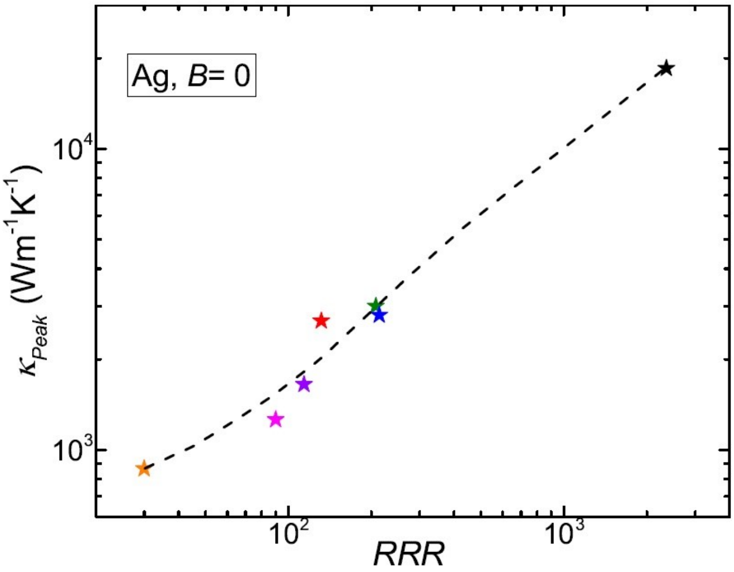

Fig. 4.6: Correlation between the RRR and the maximum of the κ(T) curve at B=0 for Ag. The symbol colors are in accordance with the results of Fig. 4.5; the dashed line is to guide the eye [206].

Figure 4.9 shows the correlation between the *RRR* and the maximum of the κ(T) curve at B = 0 for Ag. Considering the complexity of the procedure to measure R(T) on the etched short wires, this plot provides an alternative practical method to estimate the *RRR* of the Ag matrix from a κ(T) measurement performed at B = 0 on the whole conductor. Indeed, κ_{peak} of Ag can be estimated considering that $\kappa_{Ag} \approx \kappa/s_{Ag}$, since AgMg gives only second order corrections to κ at T ≲ 40 K.

As seen in Section 1.5, the fact that both κ and *RRR* increase with the overpressure proves that the three different heat-treatments have an influence on the contamination of the Ag matrix. It has been shown that, in the case of standard reaction at 1 bar, Cu diffuses from the Bi-2212 through the Ag matrix into the AgMg external sheath [23-26].

At the same time, energy dispersive x-ray spectrometry has been unable to detect Cu signal in the Ag matrix above the detection limit of 0.1 at. % [26]. This suggests that the observed *RRR* variations we observed are due to Cu concentrations in Ag ≲ 0.1 at. %.

Comparison of the present results with those of Li et al. shows that both our and their study show that extremely high thermal and electrical conductivities can be obtained after reaction [26]. However, in their experiment the *RRR* values increases with the heat treatment duration and there is an explicit evidence that Cu dissolves in the Ag, with probable consequences on thermal conductivity.

Although our results cannot be conclusive about the exact origin of the disorder, they unambiguously show that the Ag matrix contamination is hindered by high reaction pressures. A complete understanding of the mechanisms behind the improved thermal and electrical properties demands for a deep investigation of the microstructural properties of the matrix, as well as of the chemical diffusion processes from the filaments to the matrix.

Concerning the *NZPV*, the error committed in calculating this important parameter by the practical formula for REBCO CCs is below 12 % in a magnetic field of 7 T for a temperature T_t below T_c, and it remains smaller than 5 % below 50 K. The error decreases on increasing B as reported in REBCO case [149]. In particular, for the sample reacted at 100 bar overpressure, the error is considerably reduced for a 19 T magnetic field at about 1 % within the entire temperature range.

4.5 Conclusions

In summary, we have investigated the thermal conductivity of Bi-2212 wires, reacted at different overpressure heat treatments, in magnetic fields up to 19 T.

The thermal conductivity contribution of the Bi-2212 filament to the overall κ_{tot} is negligible while the AgMg contribution is lower than ≈ 10 % below 40 K. On increasing the heat-treatment pressure from 1 to 100 bar, κ is raised up to ≈ 135 % at B = 0 and ≈ 25 % at B = 19 T.

Moreover, the *RRR* of the Ag matrix is also increased from ≈ 90 to ≈ 208. We have observed that the OP processing limits the Ag-matrix contamination during the wire heat treatment. We also proposed a practical method to estimate the *RRR* of the Ag matrix from a κ(T) measurement performed at B = 0 in the reacted conductor.

Finally, in view of suggesting an approximated equation suitable for REBCO CCs we have evaluated the error in *NZPV* estimation within 10 % for T well down T_c.

CONCLUSIONS

In order to determine if a superconducting material is suitable for applications, certain fundamental properties requirements must be met. The study of the electrical transport properties concerning the transition (quench) between the superconducting and the normal region becomes crucial from the point of view of applications. Moreover, in order to avoid a quench or to adopt protection strategies, several parameters like the minimum propagation zone *MPZ,* the residual resistance ratio *RRR* and the normal zone propagation velocity *NZPV* are relevant. The determination of these parameters for a technical superconductor is a very important goal that can be done by means of thermal and electrical transport characterization.

In this framework, we have done the electrical transport measurements of Fe(Se,Te) thin films, being Fe(Se,Te) a material belonging to the 11-family of iron-based superconductors, which is one of the most attractive for high field applications at low temperatures. These measurements are accompanied by a test carried out Nb-based ultra-thin films to verify the influence of the cooling environment. Moreover, we have done the thermal and electrical characterization of the technical superconductor Bi-2212 round wire, which is a reliable candidate for solenoids and accelerator magnets able to generate magnetic fields unattainable with low-temperature superconductors.

As preliminary tests to verify if the cooling mode used has any influence on the electric transport properties, current-voltage characteristics have been acquired in three different environments on LTS ultra-thin films. In particular, we have considered the cooling in a liquid Helium cryostat and in a cryogen-free cryostat in both dynamic (flowing) and static gas conditions.

A slightly higher stability can be inferred in liquid He, in which fairly larger instability current values can be achieved with higher critical voltages, too, for field below 2 T.

The differences among the instability current I^* values measured in the three different environments decrease with the increase of the magnetic field, and this is more pronounced for the NbTiN material.

Moreover, P^* is slightly higher in LHe below 2 T. The magnetic field dependence of P^* is a fingerprint of the intrinsic microscopic mechanisms of vortex motion instability [174, 176].

However, the different cooling methods do not affect the critical currents at all, whereas the instability parameters result reproducible within few percent, so that in practice the investigated cooling methods result all suitably efficient also for high current transport measurements.

Once the efficiency of the cooling mode has been proved, a study of some properties relevant for applications of a second generation Fe(Se,Te) films grown on CaF_2 substrates has been carried on.

By means of R(T) measurements at different magnetic fields, the phase diagram H-T has been obtained. A considerable increase in T_c has been observed compared to first-generation films. A reduced transition width denotes a good sample homogeneity, better than that of first-generation films. Moreover, the $H_{c2}(T)$ slope near T_c ($dH_{c2}/dT\mid_{Tc}$) is slightly enhanced with respect to the one of the first-generation films, thus demonstrating greater robustness of the superconductivity near T_c.

From $R(T)$ data the pinning activation energy can be estimated. From the power law dependence on H of the pinning activation energy it has deduced that the single-vortex pinning regime is active at least up to 2 T, thus it can be argued that vortices are subject to strong pinning. The pinning properties have been further analyzed by means of the Dew-Hughes approach from which the interpretation of the pinning centers as local lattice displacements within 5 to 20 nm can be given, with a resulting isotropic behaviour of Fe(Se,Te)/CaF_2 thin films.

Other information about Fe(Se,Te)/CaF_2 films have been extracted by current-voltage characteristics, through the study of current stability mechanisms. The monitoring of the sample temperature during the I-V measurements has showed that a full recovery of the sample temperature during the pulsed biased measurements is achieved, thus excluding Joule self-heating effects.

The plot of the instability and critical current values has revealed the increasing I^*- I_c difference in magnetic field and in temperature which is generally related to electronic instabilities. This origin is also confirmed by the study of the critical vortex velocity v^*. However, the presence of thermal mechanisms, sometimes, are also highlighted by the presence of a smoother transition to the normal state resistance. Indeed, our results enlighten the existence of many points of contact between our experimental findings and the literature related to flux flow instabilities triggered by intrinsic electronic mechanisms in high-T_c superconductors.

By studying microbridges of different sizes, we have seen that for wide samples the heat exchange prevails and the FFI does not occur. For the intermediate wide microbridge (around 20 μm) the coexistence of thermal and electronic mechanisms is observed, while in the case of the smaller microbridge (around 10 μm), the signature of FFI is clearly visible and electronic mechanisms are predominant.

The difference between the instability current and the critical current normalized to the critical current value at zero field reported as a function of the applied magnetic field for both samples at two different temperatures has revealed that I^* decreases less than I_c. This feature is interpreted as a consequence of a higher stability in the current conduction at higher temperature, due to a weaker contribution from the extrinsic thermal mechanism to the FFI and by the weaker influence of the pinning mechanism on the instability current with respect to the influence on the critical current.

Moreover, the current transport has been found to be intrinsically stable, even as a function of the magnetic field, thus confirming the high-field performance of these materials for applications.

Concerning the thermal and electrical characterization of Bi-2212 round wire, we can conclude as follows. We have studied the thermal stability of technical superconductors $Bi_2Sr_2CaCu_2O_{8+x}$ (Bi-2212) round wires reacted at different overpressure heat treatments, in magnetic fields up to 19 T.

The thermal conductivity curves κ(T) at magnetic field up to 7 T, exhibit a clear peak whose intensity decreases as the field increases. At 19 T the peak is barely distinguishable and κ(T) increases almost monotonically. It can be also seen the linear decrement of the peak of the thermal conductivity as a function of the temperature. On increasing the heat-treatment pressure from 1 to 100 bar, κ is raised up to ≈ 135 % at B = 0 and ≈ 25 % at B = 19 T. The enhancement of the thermal conductivity is due to an increase of the *RRR* of the Ag matrix, which passes from ≈ 90 to ≈ 208 on increasing the reaction pressure from 1 to 100 bar.

Results very similar to those obtained in the wire reacted at 100 bar, both for κ and *RRR*, were previously reported for a stand-alone Ag sample from the stock used in the wire production, heat treated using a standard Bi-2212 heat treatment. From comparison, we infer that the overpressure (OP) processing limits the Ag-matrix contamination during the wire heat treatment.

We also proposed a practical method to estimate the *RRR* of the Ag matrix from a $\kappa(T)$ measurement performed at B = 0 in the reacted conductor.

In view of suggesting an approximated equation suitable for REBCO CCs we have also evaluated the error in *NZPV* estimation within 10 % for T well down T_c.

A main outcome of this work is that a higher overpressure limits the Ag-matrix contamination during the wire heat treatment, providing both the highest J_c and the highest thermal and electrical conductivity with great benefit to the thermal and electrical conductivity properties of the conductor.

Acknowledgments

It is my intention to sincerely thank the members of the research group MaSTeR-Lab of the “Dipartimento di Fisica ‘E. R. Caianiello’ – Università degli Studi di Salerno” and of the “Cnr-SPIN Salerno”, for all that I received from them from the professional and human points of view.

In particular, I would like to thank Prof. Angela Nigro for the opportunity that she gave me to work in her group making this thesis possible and ever gave me support and instruction.

I would also like to thank Dr. Gaia Grimaldi for the fruitful discussions and her encouragement and for all the opportunities she made possible to get in this doctoral period.

Many thanks to Dr. Antonio Leo for his solid theoretical preparation combined with an excellent experimental attitude from which I could learn a lot to be able to carry on my thesis work.

Thanks a lot to Dr. Anita Guarino for all her support in the lab, her patience and the many helpful tips.

I also thank all of them for all the time they have dedicated to my preparation and my training, especially in this last period of my doctorate in which I made them tired a lot.

I would like to thank the Supra group of “Département de Physique de la Matière Quantique” of Geneva University (Switzerland) and, primarly, to its chief, Prof. Carmine Senatore that provided me facilities, funds and the excellent opportunity for training during the stage period at his research group.

I would like to thank Dr. Marco Bonura for the helpful support, the many tips, for the discussions about the physics and life in general and for his helpful feedback which enhanced my work.

Thank also to the other members of the group, Davide Matera, Alexandre Fête and Christian Barth for their support and the nice working atmosphere.

Thanks a lot to Dr. Paola Romano for having created the conditions to finish the thesis work without too many worries.

I am very grateful to my family for their patience in enduring my stress and, in particular, to my mother Bianca, who have always supported me in these years.

BIBLIOGRAPHY

[1] N. Martucciello, F. Giubileo, G. Grimaldi, and V. Corato, "Introduction to the focus on superconductivity for energy," *Supercond. Sci. Technol.,* vol. 28, no. 7, p. 070201, 2015.

[2] S. Nishijima et al., "Superconductivity and the environment: a Roadmap," *Supercond. Sci. Technol.,* vol. 26, no. 11, p. 113001, 2013.

[3] R. M. Scanlan, A. P. Malozemoff, D. C. Larbalestier, "Superconducting materials for large scale applications," *Proceedings of the IEEE,* vol. 92, no. 10, p. 1639, 2004.

[4] Y. Lvovsky, E. W. Stautner, and T. Zhang, "Novel technologies and configurations of superconducting magnets for MRI," *Supercond. Sci. Technol.,* vol. 26, no. 9, p. 093001, 2013.

[5] U. Amaldi, "The importance of particle accelerators," *Europhysics News,* 31 june 2000.

[6] H. Yaghoubi, "The Most Important Maglev Applications," *Journal of Engineering,* vol. 2013, no. 537986, p. 19, 2013.

[7] S. Kopylov, N. Balashov, S. Ivanov, A. Veselovsky, V. Zhemerikin, "Use of Superconducting Devices Operating Together to Ensure the Dynamic Stability of Electric Power System," *IEEE Trans. Appl.,* vol. 21, no. 3, p. 2135, 2011.

[8] Max-Planck-Institut für Plasmaphysik (IPP), "Nuclear Fusion Status and Prospects," 4 2017. [Online]. Available: https://www.ipp.mpg.de/986351/fusion_e.pdf.

[9] W. Zeng, B. Johnson, R. Smith, N. Rubin, M. Reagor, C. Ryan, and C. Rigetti, "First quantum computers need smart software," *Nature,* vol. 549, no. 7671, pp. 156-302, 2017.

[10] C. M. Natarajan, M. G. Tanner, R. H. Hadfield, "Superconducting nanowire single-photon detectors: physics and applications," *Supercond. Sci. Technol.,* vol. 25, no. 6, 2012.

[11] W. Klein, R. P. Huebener, S. Gauss, and J. Parisi, "Nonlinearity in the Flux-Flow Behavior of Thin-film Superconductors," *J. Low Temp. Phys.,* vol. 61, p. 413, 1985.

[12] S. G. Doettinger, R. P. Huebener et al., "Electronic Instability at High Flux-Flow Velocities in High-Tc Superconducting Films," *Phys. Rev. Lett.,* vol. 73, no. 12, pp. 1691-1694, 1994.

[13] M. Liang and M. N. Kunchur, "Vortex instability in molybdenumgermanium superconducting films," *Phys. Rev. B, Condens. Matter Mater. Phys.,* vol. 82, no. 14, p. 144517, 2010.

[14] M. N. Wilson, Superconducting Magnets, Oxford: Clarendon Press, 1983.

[15] W. Si, S. J. Han, X. Shi, S. N. Ehrlich, J. Jaroszynski, A. Goyal and Q. Li, "High current superconductivity in FeSe0.5Te0.5-coated conductors at 30 tesla," *Nat. Commun.,* vol. 4, p. 1347, 2013.

[16] S. Kawale, E. Bellingeri, V. Braccini, I. Pallecchi, M. Putti, G. Grimaldi, A. Leo, A. Guarino, A. Nigro, and C. Ferdeghini, "Comparison of superconducting properties of FeSe0.5 Te0.5 thin films grown on different substrates," *IEEE Trans. Appl. Supercond.,* vol. 23, no. 3, p. 7500704, 2013.

[17] A. Leo, A. Guarino, G. Grimaldi, A. Nigro, S. Pace, E. Bellingeri, S. Kawale, C. Ferdeghini and E. Giannini, "Comparison of the pinning energy in Fe(Se1-xTex) compound between single crystals and thin films," *J. Phys.: Conf. Ser.,* vol. 507, p. 012029, 2014.

[18] E. Bellingeri, S. Kawale, F. Caglieris, V. Braccini, G. Lamura, L. Pellegrino, A. Sala, M. Putti, C. Ferdeghini, A. Jost, "High field vortex phase diagram of Fe(Se, Te) thin films," *Supercon. Sci. Technol.,* vol. 27, no. 4, p. 044007, 2014.

[19] J. M. Doval, J. Maza, C. Torron, J. A. Veira, M. Tello, and F. Vidal, "New measurements of the transition to the normal state induced by high current densities in high-Tc superconductor microbridges under thermal smallness conditions," *Adv. Sci. Technol.,* vol. 95, pp. 202-206, 2014.

[20] J. M. Doval et al., "Transition to the normal state induced by high current densities in high-Tc superconductor microbridges under applied magnetic fields," *IEEE Trans. Appl. Supercond.,* vol. 26, no. 3, p. 8000805, 2016.

[21] D. C. Larbalestier, J. Jiang, U. P. Trociewitz, F. Kametani, C. Scheuerlein, M. Dalban-Canassy, "Isotropic round-wire multifilament cuprate superconductor for generation of magnetic fields above 30 T," *nat. mat.,* vol. 13, p. 375, 2014.

[22] J. Jiang, W. L. Starch, M. Hannion, F. Kametani, U. P. Trociewitz, E. E. Hellstrom and D. C. Larbalestier, "Doubled critical current density in Bi-2212 round wires by reduction of the residual bubble density," *Supercond. Sci. Technol.,* vol. 24, no. 8, p. 082001, 2011.

[23] A. Kajbafvala, W. Nachtrab, T. Wong and J. Schwartz, "Bi2Sr2CaCu2O8+x round wires with Ag/Al oxide dispersion strengthened sheaths: microstructure–properties relationships, enhanced mechanical behavior and reduced Cu depletion," *Supercond. Sci. Technol.,* vol. 27, p. 095001, 2014.

[24] R. Bjoerstad, C. Scheuerlein, M. O. Rikel, A. Ballarino, L. Bottura, J. Jiang, M. Matras, M. Sugano, J. Hudspeth and M. Di Michiel, "Strain induced irreversible critical current degradation in highly dense Bi-2212 round wire," *Supercond. Sci. Technol.,* vol. 28, no. 6, p. 062002, 2015.

[25] T. Shen, L. Ye, P. Li, "Feasible voltage-tap based quench detection in a Ag/Bi-2212 coil enabled by fast 3D normal zone propagation," *Supercond. Sci. Technol.,* vol. 29, no. 8, p. 08LT01, 2016.

[26] P. Li, L. Ye, J, Jiang, T. Shen, "RRR and thermal conductivity of Ag and Ag-0.2 wt.%Mg alloy in Ag/Bi-2212 wires," *IOP Conf. Series: Materials Science and Engineering,* vol. 102, no. conference 1, p. 012027, 2015.

[27] M. Tinkham, Introduction to Superconductivity, New York: McGraw Hill Inc., 1996.

[28] H. Kamerlingh Onnes, Leiden Comm. 120b, 122b, 124c (1911).

[29] W. Meissner, R. Ochsenfeld, *Naturwissenschaften,* vol. 21, no. 44, pp. 787-788, November 1933.

[30] H. London and F. London, vol. A149, no. 71, 1935.

[31] A. A. Abrikosov, "On the Magnetic Properties of Superconductors of Second Group," *Sov. Phys. Jetp,* vol. 5, no. 6, p. 1174, 1957.

[32] J. Bardeen, L. N. Cooper, and J. R. Schrieffer, "Microscopic theory of superconductivity," *Phys. Rev.,* vol. 106, pp. 162-164, 1957.

[33] G. Bilbro and W. L. McMillan, *Phys. Rev. B,* vol. 14, p. 1887, 1976.

[34] J. G. Bednorz and K. A. Müller , “Possible High Tc Superconductivity in the Ba-La-Cu-O System.,” *Zeitschrift für Physik B Condensed Matter,* vol. 64, no. 2, pp. 189-193, 1986.

[35] M. K. Wu, J. R. Ashburn, C. J. Torng, P. Hor, R. L. Meng, L. Gao, Z. J. Huang, Y. Q. Wang, and C. W. Chu, *Phys. Rev. Lett.,* vol. 58, p. 908, 1987.

[36] H. Maeda, Y. Tanaka, and M. Fukutomi, *Jpn. J. Appl. Phys. ,* vol. 27, no. L209, 1988.

[37] L. Gao, Y. Y. Xue, F. Chen, Q. Xiong, R. L. Meng, D. Ramirez, and C. W. Chu, *Phys. Rev. B,* vol. 50, p. 4260, 1994.

[38] J. Nagamatsu, N. Nakagawa, T. Muranaka, Y. Zenitani, and J. Akimitsu, “Superconductivity at 39 K in magnesium diboride,” *Nature,* vol. 410, pp. 63-64, 2001.

[39] D. G. Hinks, H. Claus,and J. D. Jorgensen, “The complex nature of superconductivity in MgB2 as revealed by the reduced total isotope effect,” *Nature,* vol. 411, pp. 457-460, 2001.

[40] F. Giubileo, D. Roditchev, W. Sacks, R. Lamy, D. X. Thanh, J. Klein, S. Miraglia, D. Fruchart, J. Marcus, and Ph. Monod, “Two-Gap State Density in MgB2: A True Bulk Property or a Proximity Effect?,” *Phys. Rev. Lett.,* vol. 87, p. 177008, 2001.

[41] Y. Kamihara, T. Watanabe, M. Hirano, and H. Hosono, “Iron-Based Layered Superconductor La[O1-xFx]FeAs(x=0.05-0.12) with Tc = 26 K),” *J. Am. Chem. Soc.,* vol. 130, no. 11, pp. 3296-3297, 2008.

[42] H.Takahashi, K. Igawa, K. Arii, Y. Kamihara, M. Hirano, and H. Hosono, “Superconductivity at 43 K in an iron-based layered compound LaO1-xFxFeAs,” *Nature,* vol. 453, pp. 376-378, 2008.

[43] Zhi-An Ren et al., “Superconductivity and phase diagram in iron-based arsenic-oxides ReFeAsO1-δ (Re = rare-earth metal) without fluorine doping,” *EuroPhys. Lett.,* vol. 83, no. 1, p. 17002, 2008.

[44] G. Wu, Y. L. Xie, H. Chen, M. Zhong, R. H. Liu, B. C. Shi, Q. J. Li, X. F. Wang, T. Wu, Y. J. Yan, “Superconductivity at 56 K in samarium-doped SrFeAsF,” *Jour. Phys.: Cond. Mat.,* vol. 21, no. 14, p. 142203, 2009.

[45] Yu. V. Pustovit, A. A. Kordyuk, “Metamorphoses of electronic structure of FeSe-based superconductors (Review article),” *Low Temp. Phys. ,* vol. 42, p. 995, 2016.

[46] R. Peng, X. P. Shen, X. Xie, H. C. Xu, S. Y. Tan, M. Xia, T. Zhang, H. Y. Cao, X. G. Gong, J. P. Hu, B. P. Xie, and D. L. Feng, “Measurement of an Enhanced Superconducting Phase and a Pronounced Anisotropy of the Energy Gap of a Strained FeSe Single Layer...,” *Phys. Rev. Lett.,* vol. 112, p. 107001, 2014.

[47] J. F. Ge, Z. L. Liu, C. Liu, C. L. Gao, D. Qian, Q. K. Xue, Y. Liu, and J. F. Jia, “Superconductivity above 100 K in single-layer FeSe films on doped SrTiO3,” *Nat. Mat.,* vol. 14, pp. 285-289, 2015.

[48] Wikipedia, “High-temperature superconductivity,” [Online]. Available: https://en.wikipedia.org/wiki/High-temperature_superconductivity.

[49] V. L. Ginzburg, “Once again about high-temperature superconductivity,” *Contemp. Phys.,* vol. 33, pp. 15-23, 1992.

[50] N. W. Ashcroft, “A high-temperature superconductor?,” *Phys. Rev. Lett.,* vol. 21, pp. 1748-1750, 1968.

[51] N. W. Ashcroft, “Hydrogen dominant metallic alloys: high temperature superconductors?,” *Phys. Rev. Lett. ,* vol. 92, p. 187002, 2004.

[52] A. P. Drozdov,M. I. Eremets,I. A. Troyan,V. Ksenofontov,and S. I. Shylin , “Conventional superconductivity at 203 kelvin at high pressures in the sulfur hydride system,” *Nature,* vol. 525, no. 14964, pp. 73-76, 2015.

[53] V. Ginzburg, L. D. Landau, “Toward the superconductivity theory,” *Zh. Eksperim. Yheoret. Phys.,* vol. 29, p. 1064, 1950.

[54] V. V. Moshchalkov and J. Fritzsche, Nanostructured Superconductors, Singapore: World Scientific Publishing Co. Pte. Ltd., 2011.

[55] C.P. Poole, H.A. Farach Jr., R.J. Creswick, R. Prozorov, Superconductivity, Amsterdam: Academic Press, 1995.

[56] P. G. De Gennes , Superconductivity of Metals and Alloys, New York: Benjamin, 1966.

[57] E. H. Brandt, “Elastic and plastic properties of the flux-line lattice in type-II superconductors,” *Phys. Rev. B,* vol. 34, no. 9, p. 6514, 1986.

[58] R. P. Huebener, Magnetic Flux Structures in Superconductors, New York: Springer-Verlag Berlin Heidelberg, 2001.

[59] Y. B. Kim and M.J. Stephen, Superconductivity, New York: Marcel Dekker, 1969.

[60] D. Dew-Huges, “Flux pinning mechanisms in type II superconductors,” *Phil. Mag.,* vol. 30, no. 2, p. 293, 1974.

[61] G. Blatter, V. B. Geshkenbein, J. A. G. Koopmann, “Weak to Strong Pinning Crossover,” *Phys. Rev. Lett.,* vol. 92, no. 6, p. 067009, 2004.

[62] R. Labusch, *Cryst. Lattice Defects,* vol. 1, no. 1, p. 16, 1969.

[63] A. I. Larkin and Y. N. Ovchinnikov, “Nonlinear conductivity of superconductors in the mixed state,” *J. Exp. Theor. Phys.,* vol. 41, p. 969, 1975.

[64] S. G. Doettinger, R. P. Huebener, and A. Kahle, “Electronic instability during vortex motion in cuprate superconductors: Regime of low and high magnetic fields,” *Phys. C, Supercond.,* vol. 251, no. 3/4, p. 285–289, 1995.

[65] M. N. Kunchur, “Unstable flux flow due to heated electrons in superconducting films,” *Phys. Rev. Lett,* vol. 89, no. 13, p. 137005, 2002.

[66] J. M. Knight and M. N. Kunchur, “Energy relaxation at a hot-electron vortex instability,” *Phys. Rev. B,* vol. 74, no. 6, p. 064512, 2006.

[67] G. Grimaldi, A. Leo, D. Zola, A. Nigro, S. Pace, F. Laviano and E. Mezzetti, “Evidence for low-field crossover in the vortex critical velocity of type-II superconducting thin films,” *Phys. rev. B,* vol. 82, no. 2, p. 024512, 2010.

[68] G. Grimaldi, A. Leo, P. Sabatino, G. Carapella, A. Nigro, S. Pace, V. V. Moshchalkov, and A. V. Silhanek, “Speed limit to the Abrikosov lattice in mesoscopic superconductors,” *Phys. Rev. B ,* vol. 92, no. 2, p. 024513, 2015.

[69] G. Grimaldi et al., “Geometry Effects on Switching Currents in Superconducting,” *IEEE Trans. Appl. Supercond.,* to be published.

[70] A. Leo, F. Avitabile, N. Martucciello, J.C. Villégier, S. Pace, A. Nigro, G. Grimaldi, "Tuning the Resistive Switching of Superconducting Films by Geometry Effects," *IEEE Trans. Appl. Supercond.,* vol. in press, 2018.

[71] A. Leo, G. Grimaldi, R. Citro, A. Nigro, S. Pace, and R. P. Huebener, "Quasiparticle scattering time in niobium superconducting films," *Phys. Rev. B,* vol. 84, no. 1, p. 014536, 2011.

[72] G. Grimaldi, A. Leo, C. Cirillo, A. Casaburi, R. Cristiano, C. Attanasio, A. Nigro, S. Pace, R. P. Huebener, "Non-linear Flux Flow Resistance of Type-II Superconducting Films," *J. Supercond. Nov. Magn.,* vol. 24, pp. 81-87, 2011.

[73] J. Maza, G. Ferro, J. A. Veira, and F. Vidal, "Transition to the normal state induced by high current densities in YBa2Cu3O7−δ thin films," *Phys. Rev. B,* vol. 78, no. 9, p. 094512, 2008.

[74] J. Maza, G. Ferro, M. Rodríguez Osorio, J. A. Veira, and F. Vidal, "Analytical approach to the thermal instability of superconducting films under high current densities," *Phys. Rev. B 84,* vol. 84, no. 21, p. 214530, 2011.

[75] A. I. Bezuglyj, V. A. Shklovskij, "Effect of self-heating on flux flow instability in a superconductor near Tc," *Phys. C,* vol. 202, no. 3-4, pp. 234-242, 1992.

[76] A. Vl. Gurevich and R. G. Mints, "Self-heating in normal metals and superconductors," *Rev. Mod. Phys. ,* vol. 59, no. 4, p. 941, 1987.

[77] C. Jiang and J. P. Carbotte, "Phonon structure in anisotropic layered superconductors," *Phys. Rev. B,* vol. 45, no. 13, p. 7368, 1992.

[78] E. J. Nicol and J. P. Carbotte, "Temperature dependence of the critical pair-breaking current in thin-film, strong-coupling superconductors," *Phys. Rev. B,* vol. 43, no. 13, p. 10210, 1991.

[79] Y. Iwasa, Case Studies in Superconducting Magnets, 2nd ed. ed., New York: Springer, 2009.

[80] Paul Seidel, Applied Superconductivity Handbook on Devices and Applications, Weinheim: Wiley-VCH Verlag Gmb H & Co KGaA, 2015.

[81] L. Dresner, Stability of Superconductors, Washington: Kluwer Academic Publishers, 2002.

[82] R. H. Bellis, Y. Iwasa, "Quench propagation in high Tc superconductors," *Cryogenics,* vol. 34, no. 2, pp. 129-144, 1994.

[83] C. N. Whetstone and C. E. Roos, "Thermal Phase Transitions in Superconducting Nb-Zr Alloys," *J. Appl. Phys.,* vol. 36, no. 3, p. 783, 1965.

[84] W.J. de Haas, J. Voogd, " Proc. 33 (1930) 262 and 34 (1931) 56, Comm. 208b (1930) and 214b (1931)".

[85] C. Attanasio, C. Cirillo, "Quasiparticle relaxation mechanisms in superconductor/ferromagnet bilayers," *J. Phys.: Condens. Matt.,* vol. 24, no. 8, 2012.

[86] M. Caputo, C. Cirillo, C. Attanasio, "NbRe as candidate material for fast single photon detection," *Appl. Phys. Lett.,* vol. 111, no. 19, p. 192601, 2017.

[87] C. Cirillo, G. Carapella, M. Salvato, R. Arpaia, M. Caputo, and C. Attanasio, "Superconducting properties of noncentrosymmetric Nb0.18Re0.82 thin films probed by transport and tunneling experiments," *Phys. Rev. B,* vol. 94, no. 10, p. 104512, 2016.

[88] D. Dew Hughes, “Superconducting A-15 compounds: a review.,” *Cryogenics,* vol. 15, no. 8, p. 435, 1975.

[89] E. M. Gershenzon, G. N. Gol’tsman, I. G. Gogidze, Y. P. Gusev, A. I. Elant’ev, B. S. Karasik, and A. D. Semenov, “Millimeter and submillimeter range mixer based on electronic heating of superconducting films in the resistive state,” *Supercond. Phys. Chem. Technol.,* vol. 3, no. 10, p. 1582, 1990.

[90] K. S. Il’in, I. I. Milostnaya, A. A. Verevkin, G. N. Gol’tsman, E. M. Gershenzon, and R. Sobolewski, “Ultimate quantum efficiency of a superconducting hot-electron photodetector,” *Appl. Phys. Lett.,* vol. 73, no. 26, p. 3938, 1998.

[91] P. W. Anderson, “The resonating valence bond state in La2CuO4 and superconductivity,” *Science,* vol. 235, no. 4793, pp. 1196-1198, 1987.

[92] H. Hosono, K. Kuroki, “Iron-based superconductors: Current status of materials and pairing mechanism,” *Physica C,* vol. 514, pp. 399-422, 2015.

[93] J. Paglione and R. L. Greene, “High-temperature superconductivity in iron-based materials,” *Nature Phys.,* vol. 6, pp. 645-658, 2010.

[94] K. Tanabe and H. Hosono, “Frontiers of Research on Iron-Based Superconductors toward Their Application,” *Jpn. J. Appl. Phys.,* vol. 51, p. 10005, 2012.

[95] Y. Kamihara, H. Hiramatsu, M. Hirano, R. Kawamura, H. Yanagi, T. Kamiya, and H. Hosono, “Iron-Based Layered Superconductor: LaOFeP,” *J. Am. Chem. Soc.,* vol. 128, no. 31, pp. 10012-10013, 2006.

[96] X. H. Chen, T. Wu, G. Wu, R. H. Liu, H. Chen, and D. F. Fang, “Superconductivity at 43 K in SmFeAsO1-xFx,” *Nature,* vol. 453, pp. 761-762, 2008.

[97] Z. A. Ren et al., “Superconductivity at 55 K in Iron-Based F-Doped Layered Quaternary Compound Sm[O1-xFx] FeAs,” *Chin. Phys. Lett.,* vol. 25, no. 6, p. 2215, 2008.

[98] M. Rotter, M. Tegel, and D. Johrendt, “Superconductivity at 38 K in the Iron Arsenide (Ba1-xKx)Fe2As2,” *Phys. Rev. Lett. ,* vol. 101, p. 107006, 2008.

[99] K. Sasmal, B. Lv, B. Lorenz, A. M. Guloy, F. Chen, Y.-Y. Xue, and C.-W. Chu, “Superconducting Fe-Based Compounds (A1-xSrx)Fe2As2 with A=K and Cs with Transition Temperatures up to 37 K,” *Phys. Rev. Lett. ,* vol. 101, p. 107007, 2008.

[100] J. H. Tapp, Z. Tang, B. Lv, K. Sasmal, B. Lorenz, C. W. Chu, and A. M. Guloy, “LiFeAs: An intrinsic FeAs-based superconductor with Tc=18 K,” *Phys. Rev. B,* vol. 78, no. 060505(R), 2008.

[101] X. Zhu, F. Han, G. Mu, P. Cheng, B. Shen, B. Zeng, and H.-H. Wen, “Transition of stoichiometric Sr2VO3FeAs to a superconducting state at 37.2 K,” *Phys. Rev. B,* vol. 79, no. 220512(R), 2009.

[102] G. F. Chen, T.-L. Xia, H. X. Yang, J. Q. Li, P. Zheng, J. L. Luo, and N. L. Wang, “Possible high temperature superconductivity in a Ti-doped A–Sc–Fe–As–O (A = Ca, Sr) system,” *Supercond. Sci. Technol.,* vol. 22, no. 7, p. 072001, 2009.

[103] K. Kuroki, S. Onari, R. Arita, H. Usui, Y. Tanaka, H. Kontani, and H. Aoki, “Unconventional Pairing Originating from the Disconnected Fermi Surfaces of Superconducting LaFeAsO1-xFx,” *Phys. Rev. Lett.,* vol. 101, p. 087004, 2008.

[104] I. I. Mazin, D. J. Singh, M. D. Johannes, and M. H. Du, “Unconventional Superconductivity with a Sign Reversal in the Order Parameter of LaFeAsO1-xFx,” *Phys. Rev. Lett.,* vol. 101, p. 057003, 2008.

[105] H. Kontani and S. Onari, “Orbital-Fluctuation-Mediated Superconductivity in Iron Pnictides: Analysis of the Five-Orbital Hubbard-Holstein Model,” *Phys. Rev. Lett.,* vol. 104, p. 157001, 2010.

[106] M. Putti, I. Pallecchi, E. Bellingeri, M. R. Cimberle, M. Tropeano, C. Ferdeghini, A. Palenzona, C. Tarantini, A. Yamamoto, J. Jiang, “New Fe-based superconductors: properties relevant for applications,” *Supercond. Sci. Technol.,* vol. 23, no. 3, p. 034003, 2010.

[107] J. Jaroszynski, F. Hunte, L. Balicas, Y.-J. Jo, I. Raičević. A. Gurevich, D. C. Larbalestier, F. F. Balakirev, L. Fang, P. Cheng, Y. Jia, and H. H. Wen, “Upper critical fields and thermally-activated transport of NdFeAsO0.7F0.3 single crystal,” *Phys. Rev. B,* vol. 78, p. 174523, 2008.

[108] Z. S. Wang, H. Q. Luo, C. Ren, and H. H. Wen, “Upper critical field, anisotropy, and superconducting properties of Ba1-xKxFe2As2 single crystals,” *Phys. Rev. B,* vol. 78, p. 140501, 2008.

[109] F-C. Hsu et al., “Superconductivity in the PbO-type structure α-FeSe,” *Proc. Am. Chem. Soc.,* vol. 105, no. 38, p. 14262, 2008.

[110] Q. Li, W. Si, and I. K. Dimitrov, “Films of iron chalcogenide superconductors,” *Rep. Prog. Phys.,* vol. 74, no. 12, p. 124510, 2011.

[111] S. Medvedev, T. M. McQueen, I. A. Troyan, T. Palasyuk, M. I. Eremets, R. J. Cava, S. Naghavi, F. Casper, V. Ksenofontov, G. Wortmann and C. Felser, “Electronic and magnetic phase diagram of β-Fe1.01Se with superconductivity at 36.7 K under pressure,” *Nat. Mat.,* vol. 8, pp. 630-633, 2009.

[112] S. Margadonna, Y. Takabayashi, Y. Ohishi, Y. Mizuguchi, Y. Takano, T. Kagayama, T. Nakagawa, M. Takata, and K. Prassides, “Pressure evolution of the low-temperature crystal structure and bonding of the superconductor FeSe (Tc = 37 K),” *Phys. Rev. B,* vol. 80, no. 6-1, p. 064506, 2009.

[113] K. Buchkov, M. Polichetti, K. Nenkov, E. Nazarova, D. Mancusi, N. Balchev, D. Kovacheva, A. Zahariev and S. Pace, “Investigation of the vortex dynamics of Fe1.02Se crystals by fundamental and 3rd harmonic ac magnetic susceptibility analysis,” *Supercond. Sci. Technol.,* vol. 28, no. 3, p. 035009, 2015.

[114] J-F. Ge, Z-L. Liu, C. Liu, C-L. Gao, D. Qian, Q-K. Xue, Y. Liu and J-F. Jia, “Superconductivity above 100 K in single-layer FeSe films on doped SrTiO3,” *Nat. Mater.,* vol. 14, pp. 285-289, 2015.

[115] M. H. Fang, H. M. Pham, B. Qian, T. J. Liu, E. K. Vehstedt, Y. Liu, L. Spinu, and Z. Q. Mao, “Superconductivity close to magnetic instability in Fe(Se1-xTex)0.82,” *Phys. Rev. B ,* vol. 78, no. 22-1, p. 224503, 2008.

[116] M. Palombo, A. Malagoli, M. Pani, C. Bernini, P. Manfrinetti, A. Palenzona and M. Putti, “Exploring the feasibility of Fe(Se,Te) conductors by ex-situ powder-in-tube method,” *J. Appl. Phys.,* vol. 117, no. 21, p. 213903, 2015.

[117] T. J. Liu et al., “From (π,0) magnetic order to superconductivity with (π,π) magnetic resonance in Fe1.02Te1−xSex,” *Nat. Mat.,* vol. 9, pp. 718-720, 2010.

[118] Y. F. Nie, E. Brahimi, J. I. Budnick, W. A. Hines, M. Jain, and B. O. Wells, “Suppression of superconductivity in FeSe films under tensile strain,” *Appl. Phys. Lett.,* vol. 94, no. 24, p. 242505, 2009.

[119] T-K. Chen et al., “Low-temperature fabrication of superconducting FeSe thin films by pulsed laser deposition,” *Thin Solid Films,* vol. 519, no. 5, p. 1540, 2010.

[120] Y. Han, W. Y. Li, L. X. Cao, S. Zhang, B. Xu and B. R. Zhao , “Preparation and superconductivity of iron selenide thin films,” *J. Phys.: Condens. Matter,* vol. 21, no. 23, p. 235702, 2009.

[121] W. Si, Z-W. Lin, Q. Jie, W-G. Yin, J. Zhou, G. Gu, P. D. Johnson, and Q. Li, “Enhanced superconducting transition temperature in FeSe0.5Te0.5 thin films,” *Appl. Phys. Lett. ,* vol. 95, no. 5, p. 052504, 2009.

[122] E. Bellingeri, R. Buzio, A. Gerbi, D. Marrè, S. Congiu, M. R. Cimberle, M. Tropeano, A. S. Siri, A. Palenzona, and C. Ferdeghini , “High quality epitaxial FeSe0.5Te0.5 thin films grown on SrTiO3 substrates by pulsed laser deposition,” *Supercond. Sci. Technol.,* vol. 22, no. 10, p. 105007, 2009.

[123] E. Bellingeri, I. Pellecchi, R. Buzio, A. Gerbi, D. Marre, M. R. Cimberle, M. Tropeano, M. Putti, A. Palenzona, C. Ferdeghini, “Tc=21 K in epitaxial FeSe0.5Te0.5 thin films with biaxial compressive strain,” *Appl. Phys. Lett.,* vol. 96, no. 10, p. 102512, 2010.

[124] E. Bellingeri, I. Pallecchi, R. Buzio, A. Gerbi, D. Marrè, M. R. Cimberle, M. Tropeano, M. Putti, A. Palenzona, S. Kaciulis, “Critical Temperature Enhancement by Biaxial Compressive Strain in FeSe0.5Te0.5 Thin Films,” *J. Supercond. Nov. Magn.,* vol. 24, no. 1-2, pp. 35-41, 2011.

[125] W. Si, J. Zhou, Q. Jie, I. Dimitrov, V. Solovyov, P. D. Johnson, J. Jaroszynski, V. Matias, C. Sheehan, and Q. Li, “Iron-chalcogenide FeSe0.5Te0.5 coated superconducting tapes for high field applications,” *Appl. Phys. Lett. ,* vol. 98, no. 26, p. 262509, 2011.

[126] M-K. Wu, M-J. Wang and K-W. Yeh, “Recent advances in β-FeSe1−x and related superconductors,” *Sci. Technol. Adv. Mater.,* vol. 14, no. 1, p. 014402 , 2013.

[127] C. C. Chang, T. K. Chen, W. C. Lee, P. H. Lin, M. J. Wang, Y. C. Wen, P. M. Wu, M. K. Wu, “Superconductivity in Fe-chalcogenides,” *Physica C,* vol. 514, pp. 423-434, 2015.

[128] H. Lei, K. Wang, R. Hu, H. Ryu, M. Abeykoon, E. S. Bozin, and C. Petrovic, “Iron chalcogenide superconductors at high magnetic fields,” *Sci. Technol. Adv. Mat.,* vol. 13, no. 5, p. 054305, 2012.

[129] M. Shahbazi, X. L. Wang, C. Shekhar, O. N. Srivastava, Z. W. Lin, J. G. Zhu, and S. X. Dou, “Upper critical field and thermally activated flux flow in LaFeAsO1−xFx,” *J. Appl. Phy.,* vol. 109, no. 7, p. 07E162, 2011.

[130] S. R. Foltyn, L. Civale, J. L. MacManus-Driscoll, Q. X. Jia, B. Maiorov, H. Wang & M. Maley, “Materials science challenges for high-temperature superconducting wire,” *Nature Materials,* vol. 6, p. 631–642, 2007.

[131] X. Obradors and T. Puig, “Coated conductors for power applications: materials challenges,” *Supercond. Sci. Technol.,* vol. 27, no. 4, p. 044003, 2014.

[132] nationalmaglab, [Online]. Available: https://nationalmaglab.org/magnet-development/applied-superconductivity-center.

[133] L. Muzzi, G. De Marzi, A. Di Zenobio, and A. della Corte, “Cable-in-conduit conductors: lessons from the recent past for future developments with low and high temperature superconductors,” *Supercond. Sci. Technol.,* vol. 28, no. 5, 2015.

[134] H. Rogalla and P. H. Kes, 100 Years of Superconductivity, New York: CRC Press, 2012.

[135] H. Ullmaier, Irreversible Properties of Type II Superconductors, Berlin: Springer, 1975.

[136] A. M. Campbell, and J. E. Evetts, “Flux vortices and transport currents in Type II superconductors,” *Adv. Phys.,* vol. 21, no. 90, p. 199, 1972.

[137] E. J. Kramer, “Microstructure-critical current relationships in hard superconductors,” *J. Electron. Mater.,* vol. 4, no. 5, p. 839, 1975.

[138] T. Matsushita, Flux Pinning in Superconductors, Berlin: Springer, 2010.

[139] Heller, R. (ed) (guest ed.), “Low-Tc superconducting materials,” *Cryogenics,* vol. 48, no. 7-8, pp. 281-396, 2008.

[140] M. Suenaga and A. F. Clark, Filamentary A15 Superconductors, New York and London: Plenum Press, 1980.

[141] H. Veringa, P. Hoogendam, A. Wees, “Growth kinetics and characterization of superconducting properties of multifilament materials made by the ECN powder method,” *IEEE Trans. Magn,* vol. 19, no. 3, p. 773, 1983.

[142] A. Godeke, D. Cheng, D. R. Dietderich, P. Ferracin, S. O. Prestemon, G. Sabbi, R. M. Scanlan, “Limits of NbTi and Nb3Sn, and Development of W&R Bi-2212 HighField Accelerator Magnets,” *IEEE Trans. Appl. Superc.,* vol. 17, no. 2, pp. 1149-1152, 2007.

[143] D. Larbalestier, A. Gurevich, D. M. Feldemann, A. Polianskii, “High-Tc superconducting materials for electric power applications,” *Nature,* vol. 414, pp. 368-377, 2001.

[144] S. Graser, P. J. Hirschfeld, T. Kopp, R. Guster, B. M. Andersen and J. Mannhart, “How grain boundaries limit supercurrents in high-temperature superconductors,” *Nat. Phys.,* vol. 6, pp. 609-614, 2010.

[145] K. Heine, J. Tenbrink,M. Thöner, “High-field critical current densities in Bi2Sr2Ca1Cu2O8Cx=Ag wires,” *Appl. Phys. Lett.,* vol. 55, 1989.

[146] Malagoli, A. et al., “Evidence for length-dependent wire expansion, filament dedensification and consequent degradation of critical current density in Ag-alloy sheathed Bi-2212 wires,” *Supercond. Sci. Technol.,* vol. 26, p. 055018, 2013.

[147] T. Shen, A. Ghosh, L. Cooley, and J. Jiang, “Role of internal gases and creep of Ag in controlling the critical current density of Ag-sheathed Bi2Sr2CaCu2Ox wires,” *J. Appl. Phys.,* vol. 113, no. 21, p. 213901, 2013.

[148] J. G. Hust and A. B. Lankford, “Thermal conductivity of aluminium, copper, iron, and tungsten for temperatures from 1 K to the melting point,” *Nat. Bur. Stand., Boulder, CO,* no. NBSIR-84/3007, 1984.

[149] M. Bonura, and C. Senatore, “An equation for the quench propagation velocity valid for high field magnet use of REBCO coated conductors,” *Appl. Phys. Lett.,* vol. 108, p. 242602, 2016.

[150] A. Goyal et al., “High critical current density superconducting tapes by epitaxial deposition of YBa2Cu3Ox thick films on biaxially textured metals,” *Appl. Phys. Lett.,* vol. 69, pp. 1795-1797, 1996.

[151] S. R. Foltyn, L. Civale, J. L. MacManus-Driscoll, Q. X. Jia, B. Maiorov, H. Wang and M. Maley, “Materials science challenges for high-temperature superconducting wire,” *Nat. Mat.,* vol. 6, p. 631, 2007.

[152] K. Togano, A. Matsumoto and H. Kumakura , “Large Transport Critical Current Densities of Ag Sheathed (Ba,K)Fe2As2+Ag Superconducting Wires Fabricated by an Ex-situ Powder-in-Tube Process,” *Appl. Phys. Express,* vol. 4, no. 4, p. 043101, 2011.

[153] M. Bonura and C. Senatore, “High-field thermal transport properties of REBCO coated conductors,” *Supercond. Sci. Technol.,* vol. 28, no. 2, p. 025001, 2015.

[154] M. Bonura and C. Senatore, "Thermal Conductivity of Industrial Nb3Sn Wires Fabricated by Various Techniques," *IEEE Trans. Appl. Supercond.,* vol. 23, no. 3, 2013.

[155] M. Bonura and C. Senatore, "Thermal conductivity and stability of commercial MgB2 conductors," *Supercond. Sci. Technol.,* vol. 28, no. 11, p. 115014, 2015.

[156] M. Bonura and C. Senatore, "Transverse Thermal Conductivity of REBCO Coated Conductors," *IEEE Trans. Appl. Supercond.,* vol. 25, no. 3, p. 6601304, 2015.

[157] H. Froehlich, Elektronen theorie der Metalle, Berlin: Springer, 1936.

[158] R. W. Arenz, C. F. Clark, and W. N. Lawless, "Thermal conductivity and electrical resistivity of copper in intense magnetic fields at low temperatures," *Phys. Rev. B,* vol. 26, no. 6, p. 2727, 1982.

[159] G. K. White and R. J. Tainsh, "Lorenz Number for High-Purity Copper," *Phys. Rev. ,* vol. 119, no. 6, p. 1869, 1960.

[160] D. R. Smith, F. R. Fickett, "Low-Temperature Properties of Silver," *J. Res. Natl. Inst. Stand. Technol.,* vol. 100, no. 2, pp. 119-171, 1995.

[161] E. W. Fenton, J. S. Rogers, and S. B. Woods, "Lorenz numbers of pure aluminum, silver, and gold at low temperatures," *Can. J. of Phys.,* vol. 41, no. 12, pp. 2026-2033, 1963.

[162] Y. Iwasa, EJ McNiff, RH Bellis and K. Sato, "Magnetoresistivity of silver over the temperature range 4.1-159 K," *Cryogenics,* vol. 33, no. 8, pp. 836-837, 1993.

[163] J. W. Ekin, Experimental Techniques for Low-Temperature Measurements, New York: Oxford University Press, 2006.

[164] N. H. Balshaw, Practical Cryogenics, An Introduction to Laboratory Cryogenics, Oxford: Oxford Instruments Superconductivity Limited, 2000.

[165] R. Radebaugh, "Refrigeration for Superconductors," *Proc. IEEE,* vol. 92, no. 10, pp. 1719-34, 2004.

[166] B. Evans, R. Down, J. Keeping, O. Kirichek, Z. Bowden, "Cryogen-free low temperature sample environment for neutron scattering based on pulse tube refrigeration," *Meas. Sci. Technol.,* vol. 19, no. 3, p. 034018, 2008.

[167] L. G. Valdes, "Resistivity Measurements on Germanium for Transistors," *Proc. I.R.E.,* vol. 42, pp. 420-427, 1954.

[168] D. S. Perloff, "Four-Point Sheet Resistance Correction Factors for Thin Rectangular Samples," *Solid State Electronics,* vol. 20, no. 8, pp. 681-687, 1977.

[169] D. C. Look, Electrical Characterization of GaAs Materials and Devices, Chichester: John Willey & Sons, 1989.

[170] TEGAM Inc., "www.tegam.com," [Online]. Available: https://www.tegam.com/wp-content/uploads/2015/10/AN309.pdf.

[171] Tektronix UK Ltd, [Online]. Available: https://www.tek.com/blog/low-resistance-measurement-sourcemeter-do-i-use-current-reversal-offset-compensation-or-delta-m.

[172] J. C. Villegier, S. Bouat, P. Cavalier, R. Setzu, R. Espiau de Lamaestre, et al., “Epitaxial Growth of Sputtered Ultra-thin NbN Layers and Junctions on Sapphire,” *IEEE Trans. Appl. Supercond.,* vol. 19, no. 3, pp. 3375-3378, 2009.

[173] R. Di Leo, A. Nigro, G. Nobile, and R. Vaglio, “Niobium-titanium nitride thin films for superconducting rf accelerator cavities,” *J. Low Temp. Phys.,* vol. 78, no. I/2, pp. 41-50, 1990.

[174] G. Grimaldi, A. Leo, A. Nigro, E. Bruno, F. Priolo and S. Pace, “A Study of Current Stability in the Dissipative Flux Flow State of Superconducting Films,” *IEEE Trans. Appl. Supercond.,* vol. 23, no. 3, p. 8200704, 2013.

[175] G. Grimaldi, A. Leo, A. Nigro, S. Pace, and R. P. Huebener, “Dynamic ordering and instability of the vortex lattice in Nb films exhibiting moderately strong pinning,” *Phys. Rev. B,* vol. 80, no. 14, p. 144521, 2009.

[176] G. Grimaldi, A. Leo, A. Nigro, S. Pace, A. Angrisani Armenio, and C. Attanasio, “Flux flow velocity instability in wide superconducting films,” *J. Phys.: Conf. Ser.,* vol. 97, no. 1, p. 012111, 2008.

[177] V. Braccini, S. Kawale, E. Reich, E. Bellingeri, L. Pellegrino, A. Sala, M. Putti, K. Higashikawa, T. Kiss, B. Holzapfel, and C. Ferdeghini, “Highly effective and isotropic pinning in epitaxial Fe(Se,Te) thin films grown on CaF2 substrates,” *Appl. Phys. Lett.,* vol. 103, no. 17, p. 172601, 2013.

[178] A. Leo, G. Grimaldi, A. Guarino, F. Avitabile, A. Nigro, A. Galluzzi, D. Mancusi, M. Polichetti, S. Pace, K. Buchkov, E. Nazarova, S. Kawale, E. Bellingeri and C. Ferdeghini, “Vortex pinning properties in Fe-chalcogenides,” *Supercond. Sci. Technol.,* vol. 28, no. 12, p. 125001, 2015.

[179] K. R. Marken, H. Miao, M. Meinesz, B. Czabaj, and S. Hong, “BSCCO-2212 Conductor Development at Oxford Superconducting Technology,” *IEEE Trans. Appl. Supercond.,* vol. 13, no. 2, p. 3335, 2003.

[180] H. Miao, K. R. Marken, M. Meinesz, B. Czabaj, and S. Hong, “Development of Round Multifilament Bi-2212/Ag Wires for High Field Magnet Applications,” *IEEE Trans. Appl. Supercond.,* vol. 15, no. 2, p. 2554, 2005.

[181] Y. Huang, H. Miao, S. Hong, and J. A. Parrell, “Bi-2212 Round Wire Development for High Field Applications,” *IEEE Trans. Apll. Supercond.,* vol. 24, no. 3, p. 6400205, 2014.

[182] M. Bonura, F. Avitabile, C. Barth, J. Jiang, D. Larbalestier, A. Leo, L. Bottura, G. Grimaldi, A. Nigro, and C. Senatore, “High-Field Thermal Conductivity of OP Bi-2212 wires,” [Online]. Available: https://indico.cern.ch/event/659554/contributions/2709610/attachments/1527400/2388808/4MO1-02_Marco_Bonura_Room_2.pdf.

[183] W. E. Gifford, “The Gifford-McMahon Cycle,” in *Cryogenic Engineering Conference* -, Houston, Texas, 1965.

[184] Montana Instruments, 01 06 2016. [Online]. Available: http://resources.montanainstruments.com/help/understanding-the-gifford-mcmahon-cryocooler-cycle.

[185] A. Fête, L. Rossi, A. Augieri, and C. Senatore, “Ionic liquid gating of ultra-thin YBa2Cu3O7−x films,” *Appl. Phys. Lett.,* vol. 109, no. 19, p. 192601, 2016.

[186] Quantum Design, “PPMS Heat Capacity Option User's Manual,” 2004. [Online]. Available: https://www.mrl.ucsb.edu/sites/default/files/mrl_docs/instruments/hcapPPMS.pdf.

[187] G. Ventura, M. Perfetti, Thermal Properties of Solids at Room and Cryogenic Temperatures, Springer Netherlands, 2014.

[188] J. S. Hwang, K. J. Lin, and C. Tien, “Measurement of heat capacity by fitting the whole temperature response of a heat-pulse calorimeter,” *Review of Scientific Instruments,* vol. 68, p. 94, 1997.

[189] Lake Shore Cryotronics, [Online]. Available: http://www.lakeshore.com/products/Cryogenic-Temperature-Sensors/Cernox/Models/pages/Specifications.aspx.

[190] A. Leo, N. Martucciello, A. Guarino, V. La Ferrara, E. Bobeico, J. C. Villégier, A. Nigro, S. Pace, G. Grimaldi, “Geometry Effects on Switching Currents in Superconducting Ultra Thin Films,” *IEEE Trans. Appl. Supercond.,* vol. doi:10.1109/ISEC.2017.8314225, p. in press, 2018.

[191] Z. L. Xiao, P. Voss-de Haan, G. Jakob, and H. Adrian, “Voltage jumps in current-voltage characteristics of Bi2 Sr2 CaCu2O8+δ superconducting films: Evidence for flux-flow instability under the influence of self-heating,” *Phys. Rev. B, Condens. Matter Mater. Phys.,* vol. 57, no. 2, p. R736, 1998.

[192] C. Tarantini, A. Gurevich, J. Jaroszynski, F. Balakirev, E. Bellingeri, I. Pallecchi, C. Ferdeghini, B. Shen, H. H. Wen, and D. C. Larbalestier, “Significant enhancement of upper critical fields by doping and strain in iron-based superconductors,” *Phys. Rev. B,* vol. 84, no. 18, p. 184522, 2011.

[193] M. Tinkham, “Resistive Transition of High-Temperature Superconductors,” *Phys. Rev. Lett.,* vol. 61, no. 14, p. 1658, 1988.

[194] G. Blatter, M. V. Feigel'man, V. B. Geshkenbein, A. I. Larkin, and V. M. Vinokur, “Vortices in high-temperature superconductors,” *Rev. Mod. Phys.,* vol. 66, no. 4, p. 1125, 1994.

[195] Y. Yeshurun and A. P. Malozemoff, “Giant flux creep and irreversibility in an Y-Ba-Cu-O crystal: an alternative to the superconducting-glass model,” *Phys. Rev. Lett.,* vol. 60, no. 21, p. 2251, 1998.

[196] A. V. Silhanek, A. Leo, G. Grimaldi, G. R. Berdiyorov, M. V. Milošević, A. Nigro, S. Pace, N. Verellen, W. Gillijns, V. Metlushko, “Influence of artificial pinning on vortex lattice instability in superconducting films,” *New J. Phys.,* vol. 14, p. 053006, 2012.

[197] G. Grimaldi, A. Leo, A. Nigro, A. V. Silhanek, N. Verellen, V. V. Moshchalkov, M. V. Milošević, A. Casaburi, R. Cristiano, and S. Pace, “Controlling flux flow dissipation by changing flux pinning in superconducting films,” *Appl. Phys. Lett.,* vol. 100, no. 20, p. 202601, 2012.

[198] P. Sànchez-Lotero, D. Domìnguez, and J. Albino Aguiar, “Flux flow in current driven mesoscopic superconductors: Size effects,” *Eur. Phys. J. B,* vol. 89, no. 141, pp. 1-6, 2016.

[199] Z. L. Xiao, P. Voss-de Haan, G. Jakob, Th. Kluge, P. Haibach, and H. Adrian, E. Y. Andrei, “Flux-flow instability and its anisotropy in Bi2Sr2CaCu2O8+δ superconducting films,” *Phys. Rev. B,* vol. 59, no. 2, pp. 1481-1490, 1999.

[200] A. Leo, G. Grimaldi, P. Marra, F. Avitable, A. Guarino, E. Bellingeri, S. Kawale, C. Ferdeghini, A. Nigro, S. Pace, “Stability mechanisms of high current transport in iron-chalcogenide superconducting films,” *IEEE Trans. Appl. Supercond.,* vol. 26, no. 3, p. 8001104, 2016.

[201] A. Leo, P. Marra, G. Grimaldi, R. Citro, S. Kawale, E. Bellingeri, C. Ferdeghini, S. Pace, A. Nigro, “Competition between intrinsic and extrinsic effects in the quenching of the superconducting state in Fe(Se,Te) thin films,” *Phys. Rev. B, Condens. Matter Mater. Phys.,* vol. 93, no. 5, p. 054503, 2016.

[202] A. Bezuglyj and V. Shklovskij, “Effect of self-heating on flux flow instability in a superconductor near Tc,” *Phys. C, Supercond.,* vol. 202, no. 3/4, p. 234–242, 1992.

[203] A. Leo, G. Grimaldi, A. Guarino, F. Avitabile, P. Marra, R. Citro, V. Braccini, E. Bellingeri, C. Ferdeghini, S. Pace, and A.Nigro, “Quenching Current by Flux-Flow Instability in Iron-Chalcogenides Thin Films,” *IEEE Trans. Appl. Supercond.,* vol. 27, no. 4, p. 7300405, 2017.

[204] D. Y. Vodolazov and F. M. Peeters, “Rearrangement of the vortex lattice due to instabilities of vortex flow,” *Phys. Rev. B,* vol. 76, no. 1, p. 014521, 2007.

[205] C. Peroz and C. Villard, “Flux flow properties of niobium thin films in clean and dirty superconducting limits,” *Phys. Rev. B,* vol. 72, p. 014515, 2005.

[206] M. Bonura, F. Avitabile, C. Barth, J. Jiang, D. Larbalestier, A. F^ete, A. Leo, L. Bottura, and C. Senatore, “Very-high thermal and electrical conductivity in overpressure-processed Bi2Sr2CaCu2O8+x wires,” *Materials Research Express,* p. accepted manuscript, 2018.

[207] C. Kittel, Introduction to Solid State Physics, 8th ed., New York: Wiley, 2004.